The Dissertation Committee for Charlotte E. Sanders
certifies that this is the approved version of the following dissertation:

Tailoring Nanoscale Metallic Heterostructures with Novel Quantum Properties

Committee:

Chih-Kang Shih, Supervisor

Mark Raizen, Co-supervisor

Qian Niu

Edward Yu

Allan MacDonald

Tailoring Nanoscale Metallic Heterostructures with Novel Quantum Properties

by

Charlotte E. Sanders, B.A.; M.A.

DISSERTATION

Presented to the Faculty of the Graduate School of

The University of Texas at Austin

in Partial Fulfillment

of the Requirements

for the Degree of

DOCTOR OF PHILOSOPHY

THE UNIVERSITY OF TEXAS AT AUSTIN

May 2013

Dedicated to

Tony and Neil.

With all my love.

Acknowledgments

I want to extend my very sincere thanks to my advisor, Professor Ken Shih. I am grateful for the opportunity you have given me to work on interesting and important projects; still more, I am grateful for your active and involved mentorship, your patience, and the benefit of your wisdom. I also wish to thank my co-advisor, Professor Mark Raizen, for all the support and guidance he has given me over the course of my time at the University of Texas.

I owe thanks also to all the labmates with whom I have had the pleasure of working. My particular gratitude goes to Dr. Jisun Kim and Dr. Chendong Zhang, who have been dear friends and kind and patient teachers; to Dr. Insun Jo, for good advice; and to Dr. Alexander Ako Khajetoorians, who has been a constant mentor, benefactor, and friend, even from afar. Thank you to all my other good friends from the Shih Lab: Dr. Shengyong Qin, Dr. Jungdae Kim, Dr. Ned Flagg, Dr. Sebastien Founta, Dr. Sen Yang, John Robertson, Christopher Mann, Hyoungdo Nam, Miri Choi, Huan Li, Yuxuan Chen, Ping-Hsiang Su, and Amber Johnson. I have learned so much from all of you, both personally and professionally. I also want to express my gratitude and warm affection to my friends and colleagues in the Raizen Lab, especially Dr. Kirsten Viering and Dr. Adam Libson.

I extend my appreciation to all our collaborators. Thank you to Professor Xianggang Qiu and his group members, especially my friend Dr. Bohong Li. Thank you to Professor Gennady Shvets and his group members. Thank you to Dr. Gary Kellogg and the Center for Integrated Nanotechnologies at Sandia National Laboratory in New Mexico, not only for our collaboration but also for hosting me during my very enjoyable and productive visits to Albuquerque. Thank you to Professor Shangjr Gwo and his group members, especially Yu-Jung Lu, for the opportunity to collaborate with you and for hosting me during my delightful visit to Hsinchu, Taiwan.

Thank you to Dr. Jisun Kim, Dr. Chendong Zhang, Yuxuan Chen, Amber Johnson, Yu-Jung Lu, Dr. Bohong Li, Miri Choi, Haitao Zhou, Craig Sanders, Dana Edwards, Wenlee Jensen, and Dr. Kirsten Viering for help with the editing and preparation of this manuscript. Thank you to Craig Sanders, Kirsten Viering, and all my labmates for help with the preparation of the talks and presentations I have given over the course of my graduate studies.

Thank you to Annie Harding, Professor Ken Shih, Professor Jill Marshall, and the National Science Foundation's Integrative Graduate Education and Research Traineeship Program—not only for funding, but for a truly enriching and important extension of my graduate school experience.

Very sincere thanks to Mr. Allan Schroeder and all the members the outstanding UT Physics Machine Section. It has been a pleasure and a high honor to work with you on so many projects. Most of what I have done here would not have been possible without you.

Finally, many, many thanks and much love to my family. Thank you to my parents, my brother and sister-in-law, my grandparents, and my whole extended family for your support. Most of all, deepest thanks to Tony and Neil. You have made innumerable sacrifices so I could achieve this goal. My love and gratitude are with you always.

Charlotte Sanders

Tailoring Nanoscale Metallic Heterostructures with Novel Quantum Properties

Publication No. _____

Charlotte E. Sanders, Ph.D.
The University of Texas at Austin, 2013

Supervisors: Chih-Kang Shih
Mark Raizen

Silver (Ag) is an ideal low-loss platform for plasmonic applications, but from a materials standpoint it presents challenges. Development of plasmonic devices based on Ag thin film has been hindered both by the difficulty of fabricating such film and by its fragility out of vacuum. Silver is non-wetting on semiconducting and insulating substrates, but on certain semiconductors and insulators can adopt a metastable atomically flat epitaxial film morphology if it is deposited using the "two-step" growth method. This method consists of deposition at low temperature and annealing to room temperature. However, epitaxial Ag is metastable, and dewets out of vacuum. The mechanisms of dewetting in this system remain little understood. The fragility of Ag film presents a particular problem for the engineering of plasmonic devices, which are predicted to have important industrial applications if robust low-loss platforms can be developed.

This dissertation presents two sets of experiments. In the first set, scanning probe techniques and low energy electron microscopy have been used to characterize Ag(111) growth and dewetting on two orientations of silicon (Si), Si(111) and Si(100). These studies reveal that multiple mechanisms contribute to Ag film dewetting. Film stability is observed to increase with thickness, and thickness to play a decisive role in determining dewetting processes. A method has been developed to cap Ag film with germanium (Ge) to stabilize it against dewetting.

The second set of experiments consists of optical studies that focus on the plasmonic properties of epitaxial Ag film. Because of the problems posed until now by epitaxial Ag growth and stabilization, research and development in the area of plasmonics has been limited to devices based on rough, thermally evaporated Ag film, which is robust and simple to produce. However, plasmonic damping in such film is higher than in epitaxial film. The optical studies presented here establish that Ag film can now be stabilized sufficiently to allow optical probing and device applications out of vacuum. Furthermore, they demonstrate the superiority of epitaxial Ag film relative to thermally evaporated film as a low-loss platform for plasmonic devices spanning the visible and infrared regimes.

Table of Contents

List of Tables

List of Figures

Chapter 1

Molecular Beam Epitaxy: Background and Theory

1.1 Introduction and Historical Overview

"Epitaxy," in the most general sense of the term, refers to any process that builds structures (typically ranging in dimensions from $\mathring{A}$ to μm) which exhibit (a) crystallinity (or pseudo-crystallinity), and (b) a definite order with respect to an underlying crystalline substrate. In recent years a variety of advances in vacuum techniques, fabrication methods, and characterization tools have led to a wealth of diverse techniques which can, broadly speaking, be termed "epitaxial," and which open the door to complex and even exotic nanostructures with controlled crystallinity. Many of these have already been, or promise to be, of critical importance to both fundamental research and technological application. Examples of such structures include nanowires,[1, 2] quantum dots,[3–10] and complex multi-layer structures [11–13].

However, use of the term "epitaxy" originated with much simpler film growth techniques, still important today, which evolved after the invention of the transistor in 1947 created a sudden demand for high-purity semiconductor crystals. It was found that when a film was deposited on a semiconductor

seed crystal of the same material it could exhibit electrical properties superior to those of the original seed if the film grew with a well-defined crystallinity relative to that of the seed. Such film growth was described as "epitaxial."[14] Epitaxy of this original type, in which seed and film are of the same substance, is described as "homoepitaxial," whereas techniques developed later to grow films on substrates of dissimilar materials are known as "heteroepitaxial."

Molecular beam epitaxy (MBE) was among the earliest-used approaches to epitaxy and remains heavily used today in both fundamental research and industry. Under vacuum conditions, a source material (which can be either elemental or molecular) is vaporized, and because of the very long mean free path inside a vacuum chamber the vaporized material forms an effusive beam. A substrate is placed in the path of the beam, and the atoms or molecules adsorb to the substrate surface. With proper choice of substrate material and control of the substrate temperature the adsorbed material can crystallize. A shutter allows the beam to be turned off and on. Since the growth time for a single atomic or molecular layer (*i.e.,* a monolayer (ML)) is typically much longer than the time needed to close the shutter, one can (if the growth rate has been well calibrated) control film thickness with precision of a single ML. Moreover, when the substrate has been properly cleaned and prepared before growth, and when vacuum pressure is good, the interface between the substrate and the epitaxial film can—depending on substrate and film materials—be atomically clean and sharp.[1] Modern MBE systems operate under ultra-high vacuum

[1]This method must be distinguished from vapor phase epitaxy (VPE), in which source

(UHV) conditions (10^{-9}–10^{-11} Torr), which minimize sample contamination and lengthen the mean free path for the atomic or molecular beam.

Researchers in the 1950s and 1960s focused on developing MBE for III-V compound semiconductor films, but progress was limited by a paucity of analytical techniques for assessing stoichiometry and surface structure. As late as 1965, clean crystalline surfaces remained difficult or impossible to prepare for most materials and their structures remained in doubt.[15, 16] Progress accelerated in the late 1960s and the 1970s with the development of techniques that allowed continued improvement in vacuum conditions,[17] as well as more sensitive analysis of stoichiometry (especially through Auger electron spectroscopy (AES)[18, 19] and x-ray photoelectron spectroscopy (XPS)[19]), crystalline structure, and surface morphology (especially by electron diffraction techniques[16]). Some of these methods will be discussed in Chapter 4.

1.2 Basic Theory of Epitaxy; the Ag Growth Mode

A combination of parameters controls the morphology of an epitaxially grown structure. These include the mobility on the substrate of the atoms or molecules of the growth species; lattice matching; and interplay between bulk, surface, and interface energies.

---

material reacts chemically with a substrate or other seed that is heated to high temperature. VPE is a swift method of film growth, and therefore useful in industry. However, the high temperatures needed for the reaction tend to cause diffusion of reactants into the bulk of the substrate. Liquid phase epitaxy (LPE) is another well-established method. In LPE, a liquid is saturated with a substance to be deposited; the liquid is then cooled, and a high purity film forms. LPE films, however, are not necessarily smooth or uniform in thickness.[14]

The mobility of an adsorbate species on a substrate is determined by atomic-scale interactions between the adsorbate and the substrate lattice and also by temperature. Many common epitaxial methods use substrate heating to increase atomic mobility during deposition: thus, atoms or molecules arriving at random locations on the sample surface can move freely and find vacant positions in the growth front of the crystal lattice. Sample heating is used, for example, in growth of III-V and II-VI semiconductor films on Si. The time for an atom or molecule's diffusion and incorporation into the lattice must be less than the time for the deposition of one complete ML. Alternatively, substrate temperature can be lowered to quench mobility. This latter method will be discussed in Section 1.3.

Lattice matching (also known as "registry") is one of the most important factors that determine whether a particular epitaxial structure can be grown on a given substrate. If the two-dimensional (2D) surface of a substrate crystal is characterized by lattice constants a_1 and a_2 in the directions of basis vectors $\vec{a_1}$ and $\vec{a_2}$, respectively, and if the surface of a particular crystalline film can be characterized by lattice constants $\vec{a_1'}$ and $\vec{a_2'}$ in the directions of the same basis vectors $\vec{a_1}$ and $\vec{a_2}$, then the simplest model of lattice matching is $a_1 = n_1 a_1'$ and $a_2 = n_2 a_2'$, or $n_1 a_1 = a_1'$ and $n_2 a_2 = a_2'$, where n_1 and n_2 are integers. (In homoepitaxy, the lattice-matching requirement is trivially met.) Lattice matching determines the rotation of a film relative to its substrate, since registry is only possible at well-defined angles of the two crystalline surfaces. Slight lattice mismatch—for example, on the order of a percent or

less—results in lattice strain which can in some films be tolerated. Strain tolerance varies in different material systems. In some systems modestly strained films can grow with single crystallinity and smooth surface morphology, although strain tends to induce strain-relieving defects and can have complex consequences for electronic structure. Since the total strain energy of a film increases with film thickness, many thin-film systems exhibit a critical thickness beyond which smooth film growth becomes energetically impossible. The degree of lattice strain is dependent partly on temperature. Intentional lattice mismatching can lead to the spontaneous formation of many interesting structures. For example, in systems such as CdSe/ZnSe and InP/InGaP a strained but flat film grows for a few ML, with strain energy increasing with deposition thickness, and then the film separates into islands. This is the well-known growth mode for semiconductor quantum dots.[3–10]

Another important issue in epitaxy is the interplay between bulk energy, surface energy, and interface energy. Systems with high ratios of surface to bulk energy tend to form islands, clusters, or other structures (for example, corrugated or wavy morphologies) that reduce free energy.[20, 21] By contrast, systems in which this same ratio is low are more likely to form morphologies (such as flat film) where surface-to-volume ratio is larger. Growth morphologies that minimize interfacial area are favored in systems where interface energy is high.

Most epitaxial film growth exhibits one of three growth modes: Frank-Van der Merwe, Volmer-Weber, or Stranski-Krastanov.[22, 23] In Frank-Van

der Merwe (FV, or FM) growth, flat films grow layer by layer and are usually lattice-matched to their substrates. This mode—which generally requires that epitaxially deposited atoms bind more strongly to the substrate than to each other, so that a complete monolayer can form when growth is first initiated—is observed in some semiconductor-on-semiconductor and metal-on-metal systems, and in certain cases of gas adsorption.[23]

Volmer-Weber (VW) growth mode is the opposite of FV growth: deposited material forms clusters rather than a smooth film. This mode can occur if deposited atoms bond more strongly to each other than to the substrate, and if they therefore cluster together rather than spreading out as a film over the substrate. Volmer-Weber mode often characterizes metal epitaxy on semiconductors or insulators, where weak interaction between substrate and metal has been attributed in part to the different physics underlying the covalent bonding in the substrate and the metallic bonding in the metal.[24] A high ratio of surface to bulk energy can also promote VW growth, leading deposited material to assume a rounded, clustered morphology with small surface-to-volume ratio. Ag deposited at room temperature on a semiconductor or insulator assumes a morphology of this type: as an example, Fig. 1.1 shows Ag deposited on GaAs(110) at room temperature.

Stranski-Krastanov (SK) mode is often described as a hybrid of FV and VW modes (*e.g.,* ref. [23]). This is a phenomenologically reasonable description, though the physics driving SK growth morphology can be very different from that of either the FV or VW modes. In SK mode, initial flat

film growth yields to island growth above a thickness of a few MLs. There are many possible causes. For example, as mentioned above, a slight lattice mismatch which does not prohibit a few MLs' strained but flat film growth can nevertheless make flat film morphology unstable after several MLs' thickness and cause islands or clusters to form. Barriers to interlayer diffusion also lead to SK growth. The Ehrlich-Schwoebel (ES) interlayer diffusion barrier[25] exists because atoms incorporated at step edges have smaller numbers of nearest neighbors than atoms incorporated in terraces[26]: thus, descending step edges can present energy barriers to atoms diffusing on terraces and prevent diffusing atoms from descending to next-lower terraces. Systems in which the ES barrier is important exhibit "wedding cake"-shaped islands in which each atomic layer has a smaller radius than the one below it. Ag-on-Ag homoepitaxial growth is characterized by a wedding cake growth mode.

In order to describe the role of surface and interfacial energy in each of the three growth modes, E. Bauer's classic approach to this problem defines a quantity $\Delta \equiv \sigma_f + \sigma_i - \sigma_s$ where σ_i is the film-substrate interface energy per unit area, σ_f is the film-vacuum surface energy per unit area, and σ_s is the substrate surface energy per unit area.[27] We consider a film that is n MLs thick: if $\Delta > 0$ for all n then the model predicts rough VW-type growth. If, on the other hand, $\Delta \leq 0$ for n-ML-thick film and also for $n+1$-ML-thick film for all n, then the model predicts flat FV-type growth. If $\Delta \leq 0$ for some n-ML-thick film but $\Delta > 0$ for $n+1$-ML-thick film, then n-ML thickness is the threshold to SK-type growth. This model is qualitatively informative, but

difficult to use in a quantitative or predictive way: the interfacial energy σ_i is not precisely defined, and the film-vacuum surface energy is often difficult to determine because published values for surface energy can be different from the surface energies of very thin films.[28]

1.3 "Electronic Growth" Mode

In the late 1980s and the 1990s it was found that some types of flat metal films could be grown on certain semiconducting and insulating substrates by means of a new epitaxial procedure that was dubbed "two-step" growth.[24, 29] The substrate is held at low temperature (typically no more than 135 K) during deposition. This quenches atomic diffusivity at the growth front. After deposition, the sample is annealed at room temperature and the system evolves into a uniform flat film with atomic smoothness. Much early work focused on using this technique to prepare Ag(111) films on GaAs(110),[24, 30, 31] but the same technique has since been used for many systems including Ag(111) on Si(111)[32–34], Ag(111) on Si(100)[32], Ag(111) on glass[35], Au on Si(111)[29], Pb on Si(111),[36], Al on Si(111),[2, 37], Ag on a variety of III-V semiconducting substrates in the (110) orientation,[38] and many more.

In the case of Ag, quenched atomic mobility during deposition at low temperature causes the Ag to form clusters that are smaller than those which would otherwise form during room-temperature deposition. An example is shown in the left panel of Fig. 1.2. Notice that the scale is the same in Fig. 1.1 as in Fig. 1.2. A post-annealing film, in which the small Ag clusters have

coalesced into atomically flat Ag(111) film, is in the right panel of Fig. 1.2.[24]

The major theoretical contribution underlying the development of the two-step growth procedure was the discovery that itinerant electrons can play a key role in stabilizing or destabilizing metal films—this is the essence of the so-called "electronic growth" model.[39] The model is based on a thermodynamic analysis of metal growth on GaAs(110). The energy of a metal film is assumed to be dominated by three energy contributions: $E_{Tot} = E_{QWS} + E_C + E_F$. Here, E_{QWS} is the energy due to quantum confinement of conduction electrons in the film, E_C results from charge spilling at the boundary between the metal and the substrate, and E_F is an energy contribution resulting from Friedel oscillations.

Quantum confinement energy arises in very thin films from the confinement of itinerant electrons—treated here as a free electron gas—in one dimension. For conduction electrons the film constitutes a one-dimensional (1D) potential well which can be treated (for the sake of simplicity) as a square well potential. This "quantum size effect" (QSE) in thin metal film was investigated in the 1970s by F. Schulte for its effect on the work function,[40] and additional key work was done by P. Feibelman in the 1980s.[41, 42] However, Feibelman concluded in 1984 that the QSE was "unlikely to be observed in the laboratory"[41] because the confinement of itinerant electrons would presumably require that a metal film (if not freestanding) be grown on an insulating or semiconducting substrate, and at the time no method was known for this type of growth.

Subsequent work in the 1990s showed that the QSE can in certain cases play a decisive role in stabilizing films of particular thicknesses on semiconducting and insulating substrates. The width of the potential well is the film thickness $L = Nd$, where d is the thickness of a single ML and n is the number of MLs. The boundaries of the well are the two surfaces of the film: on one side, the interface with the substrate, and on the other, the vacuum interface. The substrate interface is taken to be an infinitely high potential barrier. The vacuum interface is a finite potential barrier whose height is the sum of the work function of the metal and the Fermi energy relative to the bottom of the conduction band. Taking the z direction to be the direction of confinement of a conduction electron and Φ_v, Φ_s to be the phases accumulated by an electron's reflection at the vacuum and substrate interfaces, respectively (accounting for wave function leakage beyond the boundaries of the potential well), then the Sommerfeld-Bohr quantization rule states that $2k_zL + \Phi_v + \Phi_s = 2\pi n$, where n takes integer values. This gives quantized, discrete allowed values for k_z as a function of film thickness. (Notice that for a free-standing film suspended in vacuum, where we can assume a phase shift of $\Phi = \pi$ at each interface, we recover the simple form for a particle in a box, $k_z(L) = \frac{\pi n}{L}$.)[43]

In computing the energy due to quantum confinement, conduction electrons are strictly forbidden from crossing the boundary between the metal and substrate. However, in the calculation of the second energy contribution, charge spilling is explicitly accounted for. Since the Fermi energies of the metal and substrate must align (and it should be observed that the Fermi energy in

the metal is raised by the QSE), a region of charge develops on either side of the interface. The resulting positively and negatively charged regions can be modeled as the plates of a parallel-plate capacitor. The thicknesses of the charged regions are equal to the screening lengths in the metal and substrate (e.g., 0.59 $\mathring{A}$ in Ag and 2.8 $\mathring{A}$ in GaAs[39]), and the centroids of these regions are treated as the effective locations of the plates of the capacitor. This capacitive contribution to the system's energy is simply $E_C = \frac{1}{2}CV^2$.[39]

The final energy contribution E_F comes from Friedel oscillations in the density of the free electron gas. The metal-substrate boundary is, for the calculation of this energy contribution, ignored, so the electron gas can be treated as semi-infinite and the Friedel oscillations as arising only from confinement at the film-vacuum interface. The electron density within the film can be shown to be $\frac{n(u)}{n_0} = \frac{1+3\frac{cos(u)-sin(u)}{u}}{u^2}$.[39] Here, $u = 2k_F z$, with z the distance from the surface-vacuum interface (we are only interested in those values of z which are less than the film thickness: $z < L$) and k_F the Fermi wave vector in the metal film. The electron density in the film therefore depends on both the intrinsic material properties of the metal film and on the film thickness. The effect of the Friedel oscillations on the system's energy is to amplify the effect of quantum confinement: the total quantum confinement energy of the system is large if there is a high electron density within the quantum well.

1.4 Electronic Growth of Ag(111) on Si

Early development of the two-step method for Ag film growth was carried out mainly on III-V semiconducting substrates. However, the importance of Si—especially Si(100)—for industrial applications and the ease with which atomically clean Si surfaces can be prepared have motivated extension of the method to this substrate. Growth of Ag(111) on Si was investigated by Matsuda *et al.* in 2001 and Jiang *et al.* in 2002.[32, 44] In both sets of studies, substrates were flashed to obtain either the clean 7x7 reconstruction, in the case of Si(111), or the 2x1/1x2 reconstruction, in the case of Si(100). The growth procedure was the same "two-step" procedure already described for GaAs(110). The growth mode manifested significant differences relative to the growth mode on GaAs. Deposition on GaAs of thicknesses less than the critical thickness yields only flat-topped mesas interspersed with bare substrate. Deposition at or above the critical thickness leads to the emergence of a uniform flat film fully covering the substrate. By contrast, deposition on Si leads first to the formation of an irregular wetting layer. At thicker deposition, three thickness regimes emerge: at very low coverage below the so-called "sub-critical thickness" L_1 there is cluster formation. Above L_1 the morphology consists of flat-topped terraces. No flat continuous film emerges until the nominal thickness reaches an "upper critical thickness" L_2. Jiang *et al.* found $L_1 = 2$ ML and $L_2 = 6$ ML for Ag on Si(111), and $L_1 = 5$ M and $L_2 = 9$ ML for Ag on Si(100). Matsuda and colleagues observed similar behavior, but reported lower values for the upper critical thicknesses on Si(100): at $L_2 = 5$

ML deposition they already saw a flat film emerging, and consequently defined the upper critical thickness as 6 ML.[44] The reason for these discrepancies remains unresolved. Qualitatively, the trends Matsuda *et al.* observed were otherwise similar to those observed by Jiang *et al.* The flat film which emerges at the upper critical thickness has a different morphology from that observed on GaAs(110). Close to L_2 the film exhibits voids that extend down to the wetting layer.[32]

At larger thicknesses the film exhibits ± 1 ML pits and islands distributed evenly over the terraces. As Fig. 1.2(b) shows, Ag on GaAs(110) forms an atomically flat film over large areas. Fig. 1.3 shows a low-temperature scanning tunneling microscopy (LT-STM) image of typical morphology for a relatively thick, 10-ML Ag film on Si(111) after annealing. A noticeable difference is the presence of steps in Fig. 1.3; however, these steps are not a property of the film itself but rather are steps in the underlying Si(111) substrate that the Ag film simply follows. GaAs(110) cleaved *in situ* is characterized by extremely wide flat terraces, as in Fig. 1.2(b). More importantly, however, the pits and holes that characterize the film grown on Si(111) are entirely absent in film grown on GaAs(110). It is noteworthy that the crystalline orientation of the Ag film on GaAs(110), on Si(111), and on Si(100) is always Ag(111). This fact is indicated by electron diffraction studies and will be discussed in Chapter 5.

The differences between growth on Si(111) and Si(100) with respect to the values of L_1, L_2 have been suggested by Jiang *et al.* to arise from different

pinning positions of the Fermi energy at the interfaces of the two types of substrate. For the Ag(111)/Si(111) 7x7 interface the pinning position is 0.7 eV above the valence band maximum, whereas for Ag(111)/Si(100) 1x2/2x1 it is only 0.3 eV above the valence band maximum. This in turn means that the quantum confinement barrier is 0.4 eV higher at the Si(100) interface than at the Si(111) interface, and so the energy due to quantum confinement is higher. The higher quantum confinement energy in Ag(111)/Si(100) perhaps accounts for the larger critical thicknesses observed.

Jiang *et al.* attribute the differences between growth on GaAs and Si to the fact that both Si(111) and Si(100) have surface states in the band gap, whereas GaAs(110) has none. The presence of surface states presumably enhances charge spilling.

As a final important point, both Ag(111)/GaAs(110) and Ag(111)/Si(100) exhibit subtle superstructures: in Ag on GaAs(110) there is a 1/5-ML high, quasi-periodic striped corrugation with stripe separations of 1.2 and 1.7 nm that can be seen in Fig. 1.2(b),[24, 31] while in Ag on Si(100) there is a 1/3-ML-high striped corrugation with average stripe separation of 14 nm. The corrugation of the film on Si(100) is interpreted by both Jiang and Matsuda as being due to stress effects in the film. The cause of the corrugation of the film on GaAs remains unknown, but defects in its periodicity are attributed to stress arising from lattice mismatch.[31] These issues will be discussed in Chapters 2 and 6. Here it is important only to note that, as Jiang *et al.* suggest, the persistence of voids in Ag(111)/Si(100) close to the upper critical

thickness might have the effect of relieving strain in those films, and this strain relief might make an additional contribution to the differences observed in Ag growth on the three types of substrates.

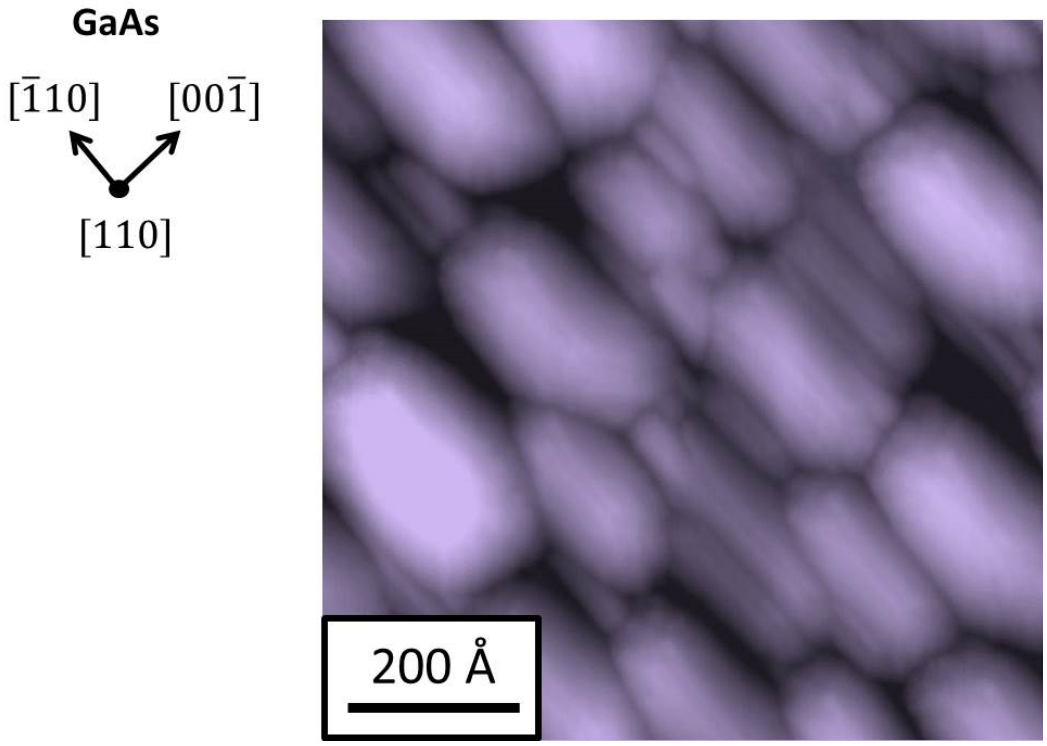

Figure 1.1: From [24]. Scanning tunneling microscopy (STM) topographic image of Ag grown and scanned at room temperature on GaAs(110). The Ag forms irregular clusters with sizes on the order of 100–200 $\mathring{A}$. The anisotropy of the Ag clusters is particular to their interaction with the underlying GaAs(110) substrate, whose orientation is as shown to the left of the image. Reproduced with permission from AAAS.

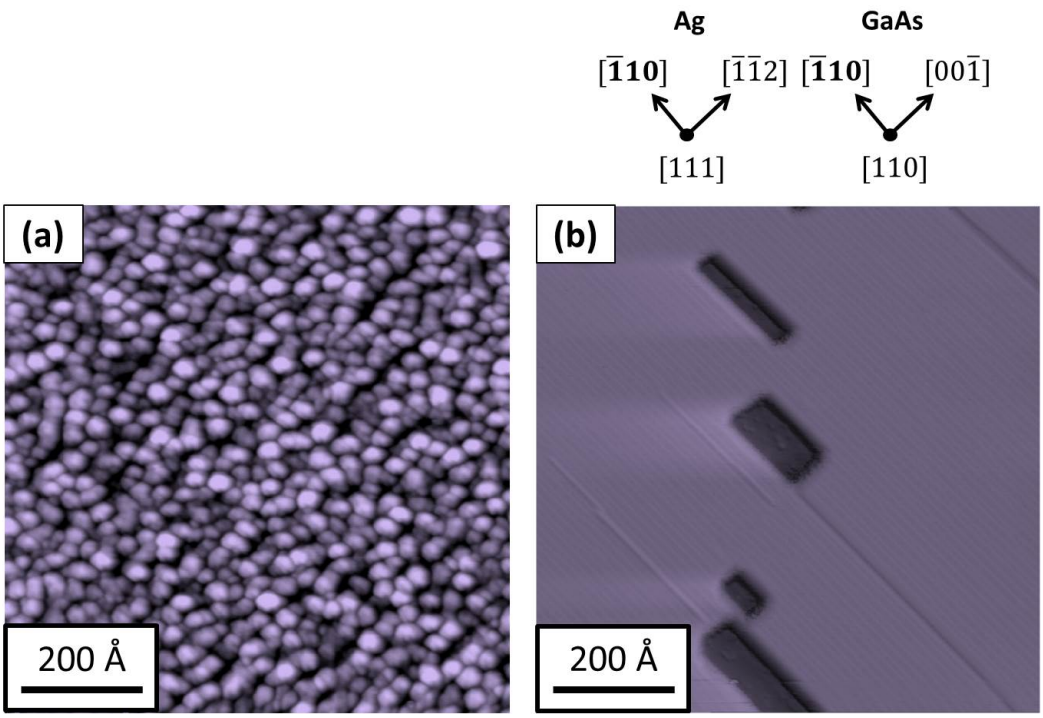

Figure 1.2: From [24]. Left: STM topographic image of as-deposited Ag clusters on GaAs(110) at 135 K, before annealing. Right: STM topographic image showing flat, atomically smooth Ag(111) film on GaAs(110) after annealing to room temperature. The square shapes in the right panel are voids that penetrate to the substrate. The QSE dictates a minimum stable thickness for Ag on GaAs(110), and this flat film is precisely at the minimum thickness. Regions of lesser coverage evolve into holes. Reproduced with permission from AAAS.

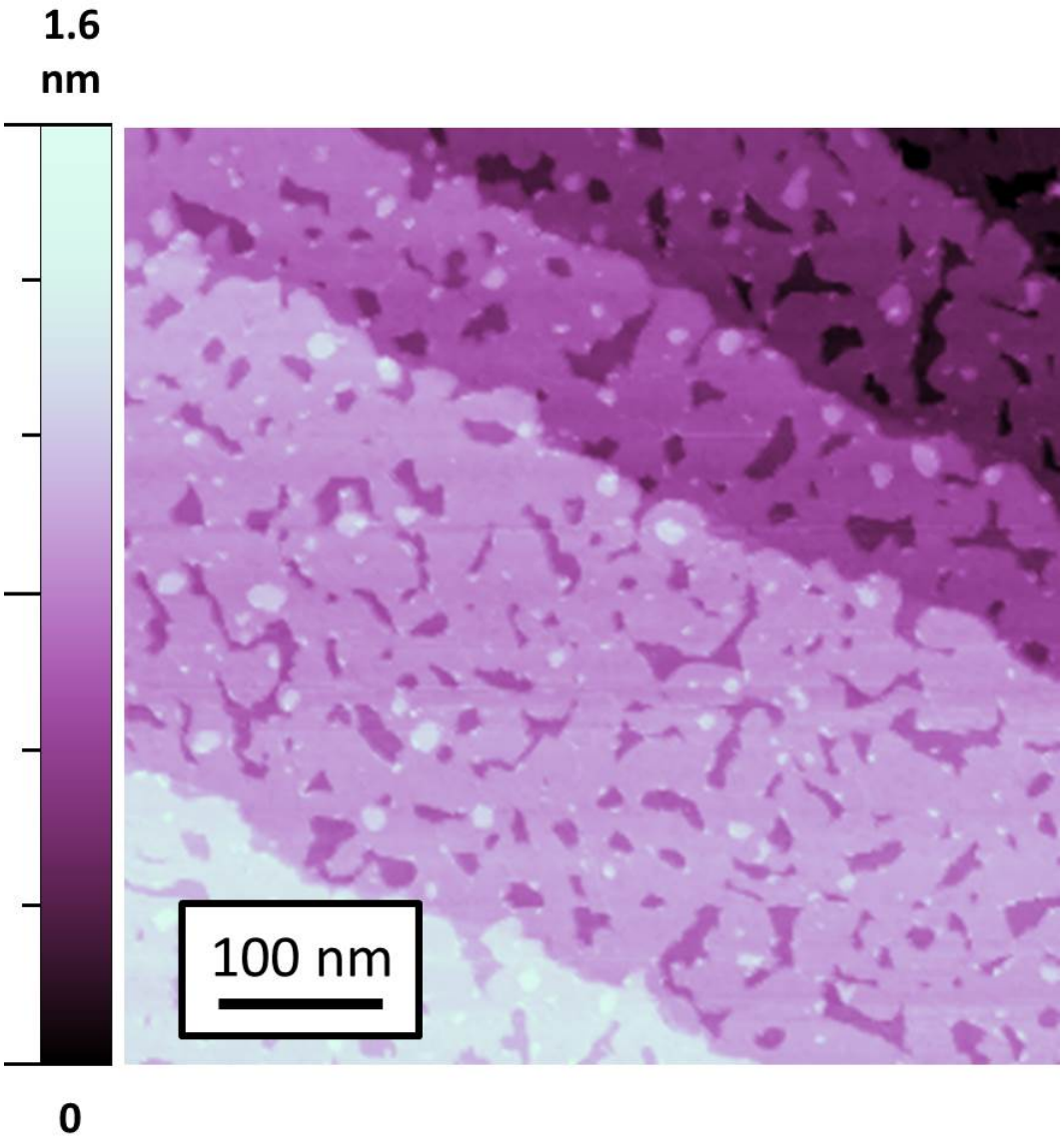

Figure 1.3: STM image acquired at 78 K. 10 ML Ag(111) film on Si(111), post-annealing. Film follows underlying substrate steps. Features on terraces are 1-ML islands and 1-ML pits in the Ag film.

Chapter 2

Silver Film Metastability and Dewetting: Background and Theory

Because the flat film morphology is, for Ag on semiconducting or insulting substrates, a metastable state, it will eventually give way to a lower energy state consisting of clusters if the kinetic pathway to such a state can be accessed. Thus, flat Ag film tends to exhibit surface roughening and dewetting (characterized by hole and island formation) on a time scale that depends on numerous factors. These factors remain little studied, but presumably include temperature, pressure, choice of substrate, substrate coverage, film thickness, and chemical composition of the environment. Although Ag film instability on semiconducting substrates has been a major obstacle to technological applications, and although a competition between stabilizing and destabilizing energetics underlies the physics of Ag film growth, little research has been done in this area. This chapter surveys the existing literature on relevant topics.

2.1 Ag(111) Film Dewetting on GaAs(110)

The stability of the Ag(111)/GaAs(110) system was investigated in 2001 by H. Yu *et al.* [45] The authors used the two-step method to grow

atomically smooth Ag film on GaAs(110), and low-temperature scanning tunneling microscopy (LT-STM) to characterize changing film morphology. The films were annealed at room temperature for different lengths of time and then scanned at liquid nitrogen temperature. Two distinct types of evolution were observed, depending on whether pinholes were present or not.

For a study of film with pinholes, thin film close to the critical thickness was prepared. As in Fig. 1.2, this film was atomically flat except for voids to the substrate. Furthermore, the density of voids was enhanced by annealing the film to room temperature unusually quickly, within only 10 min. after deposition. These films with pinholes were seen to begin dewetting at room temperature under UHV within a few hours. Fig. 2.1, reproduced from H. Yu *et al.*,[45] shows a film of 6.4 ML after it remained at room temperature (in UHV) for 162 min. Panel 2.1(a) shows the film topography after 2.7 hours. Panels 2.1(c)–(f) show the progression of dewetting up to 4.5 days. Hole size increases and islands appear, as atoms are transferred upward from the edges of the pits to the top of the film.

By contrast, H. Yu *et al.* observed that when deposition was thick enough to evolve into a film with no voids, the film was robust with respect to annealing, and film quality improved with time. Furthermore, annealing to temperatures above room temperature made film smoothness even better. This is illustrated in Fig. 2.2, where a 25-ML-thick film with five exposed atomic layers in panel 2.2(a) evolves after 13 hours at room temperature into a smoother film showing only three atomic layers in panel 2.2(b). The same

film was then annealed to 112°C for 20 min., after which further smoothing was observed, with two atomic layers dominant and only minor presence of a third.

It is not difficult to see why holes do not readily form in films in which there are initially no voids: the instability of all thicknesses less than 6 ML means that for a new hole to appear, at least 6-MLs' thickness of material must be transferred to the surface of the surrounding film.[46] There can be no formation of an intermediate state consisting of a shallow hole where the underlying thickness is less than 6 ML, since such thicknesses are forbidden. A large and sudden mass transfer therefore needs to occur for a pinhole to form to the substrate, and the energy barrier to such an event is high. For thicker films like the 25-ML-thick film studied by H. Yu *et al.*, the kinetic barrier is still higher.

In a film with voids, like the one in Fig. 2.1, the total number of holes does not increase during annealing, presumably for the reason just explained.[45, 46] However, the sizes of the holes increase, because atoms from the void edges can be transferred to the top of the film. The edges of the holes consist, presumably, of steeply stepped walls. Because 6 ML is the minimum stable thickness, the lower steps are intrinsically unstable (see Fig. 2.3), and the system's free energy is reduced if the atoms at the lower steps move upwards to locally thicker film regions. Because this upward motion of atoms from the bottoms of the void walls thickens the film it also lowers local quantum confinement energy. The process leads to increasingly rough film. As

can be seen in Fig. 2.1, mass transfer from the holes to the islands on top of the film is strongly anisotropic: both holes and islands have long thin shapes oriented along the $(1\bar{1}0)$ direction of both the Ag(111) film and the GaAs(110) substrate. During prolonged annealing at room temperature, holes and islands grow along that direction, but scarcely at all in the GaAs$(00\bar{1})$ direction. H. Evans *et al.* examined this phenomenon in detail.[46] Fig. 3 shows a schematic of a hole: alternating step heights are colored dark and light. The sides of the hole that exhibit (100) microfacets are labeled "A," and the sides of the hole that exhibit (111) microfacets are labeled "B." The atoms incorporated along these facets all have four in-plane nearest neighbors. By contrast, microfacets on the short sides of the holes are characterized by $(\bar{1}\bar{1}2)$ orientation, with smaller linear density along the $(1\bar{1}0)$ direction and only three nearest neighbors. Thus, the energy barrier for an atom on a lower step to leave the lattice and migrate out of the hole is lowest on the $(\bar{1}\bar{1}2)$-oriented sides of the hole, and the collective movement of atoms up the stepped wall of these sides is more rapid than at any other wall. Subtleties of this model are discussed by Evans *et al.* [46]

2.2 Stress Effects in Ag(111) Film

The degree and mechanism of strain in epitaxial Ag(111) film on Si(111), Si(100), and GaAs(110) remain open to debate. On one hand, there is evidence that strain does exist in such systems. Ag(111) has a strong Shockley-type surface state in the band gap that exists along its $\Gamma - L$ direction: in bulk Ag,

the energy of this state is about 50 meV below the Fermi energy (at 130 K), but in Ag film on Si(111) this surface state shifts to above the Fermi energy. G. Neuhold *et al.* show that this shift can be accounted for by lattice strain as small as 0.95%.[47] Moreover, as discussed in Chapter 1, Jiang *et al.* have identified a striped superstructure that arises in Ag film grown on Si(100). The stripes run parallel to the underlying Si(001) direction, rotating on alternating Si steps, and exhibit an average separation of about 14 nm.[32] They attribute this to strain effects due to lattice mismatch.

On the other hand, the lattice constant of Ag film on both Si(111) and Si(100) is reported to be very close to that of bulk Ag,[47–49] which would seem to suggest that strain effects do not play a large role in such systems. Furthermore, strain energy typically increases with film thickness, tending to destabilize thick films. This has not been seen in Ag: as will be discussed in Chapter 6, our own data shows that Ag film stability increases with film thickness.

2.3 Adatom and Vacancy Diffusion on the Ag(111) Surface

Because the surface morphology of epitaxial Ag(111) film on Si is dominated by 1-ML islands and pits, it is important to consider how these features evolve. G. Comsa and colleagues studied the evolution of 1-ML pits and holes on bulk Ag(111). Although care should be taken in applying their results to thin films, where surface energy and stress effects may be different, the findings

are relevant to the observations that will be described in Chapter 6.

The evolution of 1-ML islands on Ag(111) is an Ostwald ripening process: atoms evaporate from the step edges of small islands and diffuse to larger islands.[50, 51] The process is driven by the tendency of the system to minimize the free energy of surface steps. First, island coarsening reduces total step length. Second, the step edges of small islands are more energetically costly, due to their small radii of curvature, than straight or large-radius step edges. (Stated differently, the vapor pressure of small islands is larger than the vapor pressure of large islands.[52]) Ultimately, migration of all adatoms to straight steps is energetically favored. Ag adatom diffusion is dominated by hopping to nearest-neighbor sites, with an energy barrier of approximately 70 meV.[53] Adatoms cannot diffuse over step edges or down into pits because of the ES barrier (see Chapter 1): an adatom must remain on its original terrace. The rate at which Ostwald ripening occurs in this system is found to be diffusion-limited (i.e., limited by the speed of mass transport between clusters, as opposed to rate-limited, in which case the rate of attachment and detachment at step edges would control the speed of the process).[51]

Evolution of 1-ML pits proceeds by different mechanisms than does the evolution of islands. Pits do not evaporate: rather, they migrate by Brownian motion across individual terraces, maintaining constant area.[52, 54] The motion of the pits is produced by random edge diffusion of step atoms at the boundaries of the pits.[52] If two pits happen to meet they coalesce to form a new pit whose area is the sum of the areas of the two original pits.

Thus, a terrace consisting of 1-ML pits and islands evolves gradually toward a morphology in which adatom islands have evaporated and coalesced at the ascending side of straight steps, and pits have migrated by random walk trajectories—hence, rather slowly—to descending step edges.

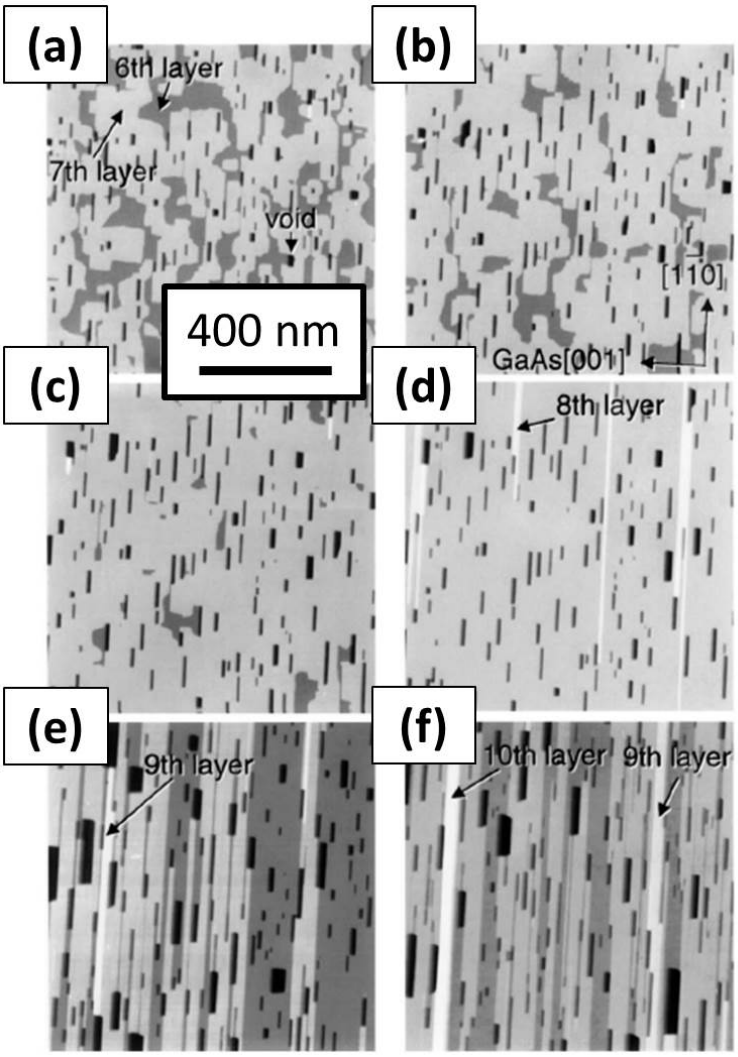

Figure 2.1: Reprinted figure with permission from [45]. Original caption: STM images taken (a) 162, (b) 292, (c) 422, (d) 1387, (e) 4577, and (f) 6363 min. after warm-up to room temperature. Images (a) to (c) show the completion of the 7th layer by transferring Ag atoms from the voids. In image (d), the 8th layer starts to grow on top of the 7th layer, and images (e) and (f) show the formation of the 9th and 10th layers, respectively. Copyright 2001 by the American Physical Society.

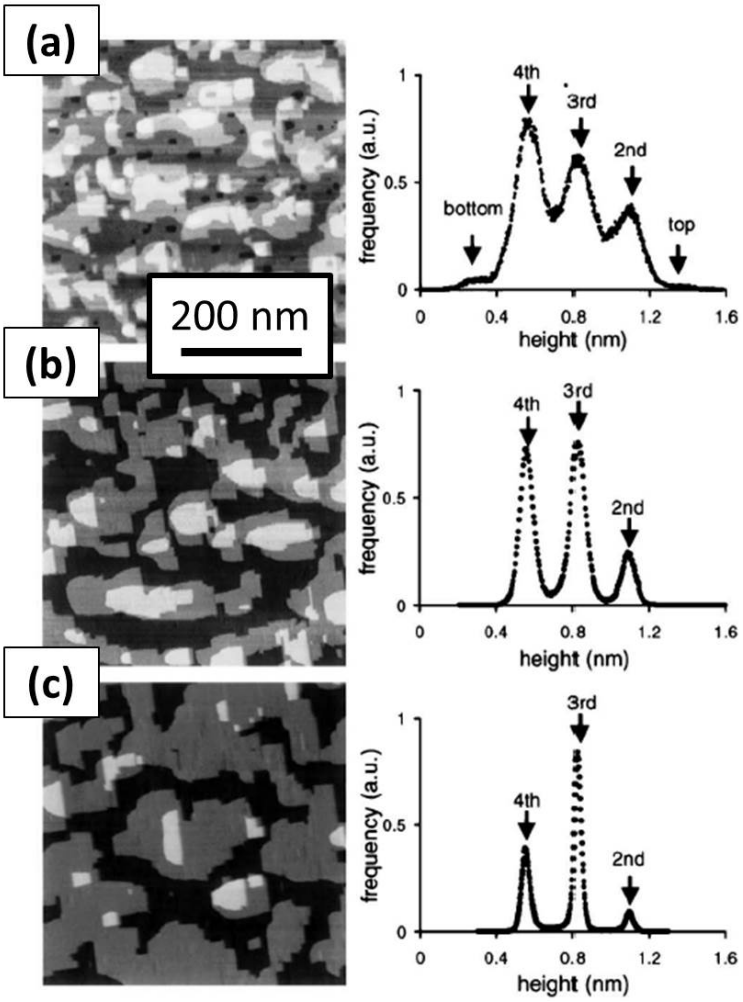

Figure 2.2: Reprinted figure with permission from [45]. Original caption: STM images (left) and the respective height distributions (right) of a 25 ML thick film. (a) and (b) show that at room temperature the initially exposed five layers of film evolve after 13 h. into a morphology with three exposed layers. (c) is obtained after annealing the film to 385 K for 20 min. A further evolution toward a film with two exposed layers is visible. Copyright 2001 by the American Physical Society.

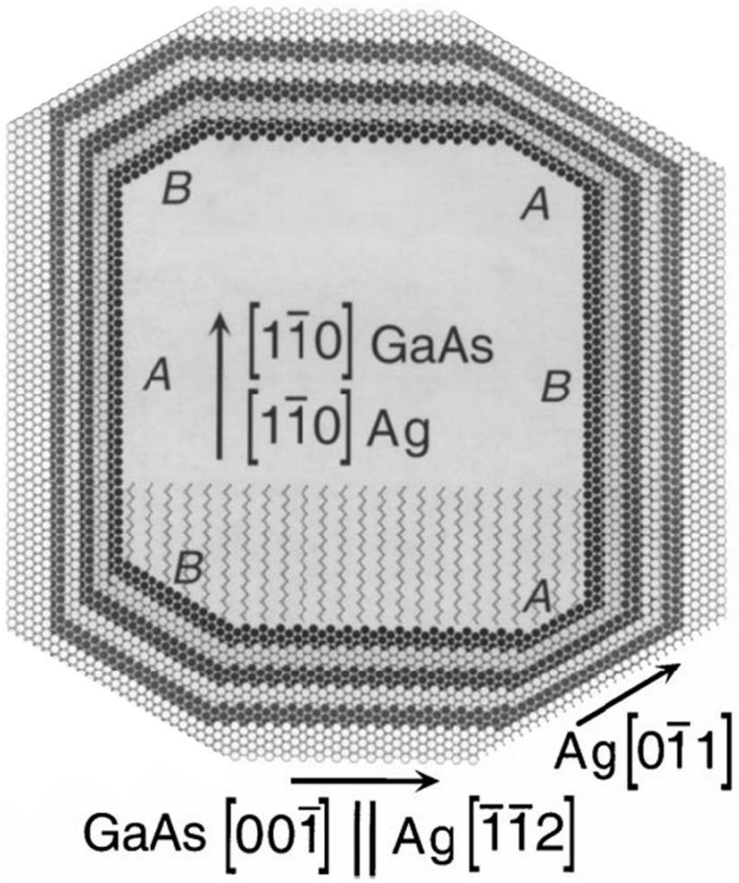

Figure 2.3: Reprinted from [46]. Original caption: Model of void B showing six layers of Ag(111) with six A- and B-type steps with maximum linear density and $\langle 011 \rangle$ orientations. The two top and bottom boundaries are perpendicular to GaAs. The angles formed by the A- and B-type steps are 26°, as determined by cross-sectional scans. This indicates that the terraces are two atoms in width. Note that imaging to provide the detail of the model was not possible and that Ag atoms at the steps are dynamic at 300 K. The base of the void reveals zigzag rows of GaAs. Reproduced with permission from Elsevier.

Chapter 3

Silver as Plasmonics Device Platform: Background and Theory

When an electromagnetic (EM) wave is incident on the interface between a conductor and an insulator, it can couple with collective oscillations of conduction electrons at the conductor's surface. The hybrid oscillation that results is known as a *surface plasmon polariton* (SPP) and in the past two decades has been found to have a wide array of potentially important technological applications. Areas of active research and development focus on the design of both nanostructure- and thin-film-based devices. Many applications have been demonstrated or proposed, including superlensing (*i.e.,* imaging with metamaterial-based lenses capable of surpassing the diffraction limit),[55–58] cancer detection and treatment,[59–61] chemical and biological sensing,[62] optical invisibility cloaking,[63–67] and others.

Plasmonic propagation in conductive thin films is of particular interest for applications in ultrafast circuitry. While modern electronic circuitry features length scales down to the few-nm regime, electronic devices are intrinsically limited with respect to signal speed: resistive and capacitive (RC) delays and dissipative losses make speeds of higher than tens of GHz difficult to

achieve.[68] By contrast, photonic devices operate readily in the THz regime, but are limited with respect to their size scale, requiring dimensions at least on the order of the wavelength of light at the regime in which they operate. A new generation of circuitry based on SPPs could combine the bandwidth of photonic devices with a size scale closer to that of electronic devices.[68, 69]

Plasmonic wavelengths are shorter than those of the EM fields that excite them. Additionally, SPPs are confined tightly to the interfaces where they propagate, leading to high EM energy density. Thus, characteristic SPP length scales are extremely small. It is therefore predicted that plasmonic devices can be fabricated at small enough length scales to allow for on-chip integration of photonic and electronic circuitry. Plasmonic circuit elements analogous to electronic circuit elements have already been demonstrated. SPP waveguides[70, 71] and reflectors[72] together constitute a plasmonic equivalent to the wires used in traditional circuits. In addition, switches, modulators, filters, transistors, and logic elements have all been realized.[73–82] Importantly, these devices can be fabricated on thin films using standard nanopatterning techniques. Until now, however, it has not been possible to fabricate the films themselves in a scalable, industrializable manner.

3.1 Historical Background

Preliminary studies of SPPs date to the turn of the twentieth century. Early work was done by A. Sommerfeld on EM propagation on single metal wires[83] and by J. Zenneck on EM propagation over flat metal surfaces.[84]

However, major work began in the mid-twentieth century, with efforts to explain observed energy losses in fast electrons passing through thin metallic films. Experimental work by G. Ruthemann[85] and W. Lang[86] informed a detailed four-part treatment by Pines and Bohm of oscillations by conduction electrons within the bulk of a metal.[87–90] These are the oscillations now known as "bulk plasmons." Pines and Bohm identified the resonant frequency of these oscillations as $\omega_p = \sqrt{\frac{ne^2}{\epsilon_0 m}}$, now referred to as the "plasma frequency;" $\hbar\omega_p$ is approximately 10 eV for many metals. The findings of Pines and Bohm led to now classic work by R. Ritchie that coined the term "plasmon" and expanded upon Pines and Bohm's theory. This work opened the door to the study of SPPs, predicting an additional "lowered plasma frequency" surface mode at $\frac{\omega_p}{\sqrt{2}}$. Experimental findings by C. Powell and J. Swan[91, 92] supported Ritchie's predictions. Since that time, the study of SPPs and efforts to harness them for device applications have become a major research focus worldwide. An important landmark was the observation in 1998 by T. W. Ebbesen *et al.* of SPP-mediated extraordinary optical transmission (EOT) through metal films patterned with arrays of sub-wavelength holes: this study gave significant impetus to the field and raised interest in the engineering of novel plasmonic devices.[93]

3.2 Basic Theory of Plasmonics

Surface plasmon polaritons are propagating longitudinal charge density oscillations confined to the interface between a conductor and a dielectric and

coupled to an incident electromagnetic field. The charge density oscillation at the interface creates a fluctuating elecric field directed out of the interfacial plane. This oscillating $\vec{E_{SPP}}$ field induces an $\vec{H_{SPP}}$ field in the plane of the interface—see Fig. 3.1(a). The electric field decays exponentially on either side of the interface, as illustrated in Fig. 3.1(b) where the decay lengths in the conductor and dielectric are labeled δ_m and δ_d, respectively.

The basic relationships defining this system are as follows:

1. The SPP wave vector depends on ϵ_m and ϵ_d, the relative dielectric functions of the conductor and the dielectric, by

$$k_x = \frac{\omega}{c}\sqrt{\frac{\epsilon_m \epsilon_d}{\epsilon_m + \epsilon_d}}. \tag{3-1}$$

2. The evanescent field decays exponentially on either side of the interface. The decay length is characterized by wave vectors $\vec{k_{mz}}$ and $\vec{k_{dz}}$ perpendicular to the interface in the conductor and dielectric:

$$\frac{k_{mz}}{k_{dz}} = -\frac{\epsilon_m}{\epsilon_d}. \tag{3-2}$$

   Thus, the decay lengths of the electric field in the conductor and dielectric are $\delta_m = \frac{1}{k_{mz}}$ and $\delta_d = \frac{1}{k_{dz}}$, respectively. See 3.1(b).

The derivation of these equations is based on a Drude-like approach and is fully explained in many texts—for example, see reference [95]. It involves

a great deal of algebra and will not be examined in detail here. In brief, the derivation starts with the assumption of a semi-infinite, non-magnetic conductor, which we treat as a free-electron gas moving relative to a fixed ionic background. Details of the band structure are mostly ignored, although it enters the model via the electrons' effective optical mass m. The electrons' equation of motion is then

$$m\ddot{\vec{x}} + m\gamma\dot{\vec{x}} = -e\vec{E}, \tag{3-3}$$

where γ is a characteristic collision frequency—essentially, damping—and $\vec{E}$ is the electric field of the incident EM wave that excites the SPP. The time dependence of $\vec{E}$ is assumed to be harmonic. From these assumptions it is straightforward to show, using Maxwell's equations, that the complex dielectric function $\epsilon_m(\omega) = \epsilon'_m(\omega) + \imath\epsilon''_m(\omega)$ of the free electron gas is

$$\epsilon_m(\omega) = 1 - \frac{\omega_p^2}{\omega^2 + \imath\gamma\omega} = (1 - \frac{\omega_p^2\tau^2}{\omega^2\tau^2 + 1}) + \imath(\frac{\omega_p^2\tau}{\omega(\omega^2\tau^2 + 1)}). \tag{3-4}$$

Here, n represents the number of conduction electrons per unit volume and τ is electronic relaxation time. In many cases, $\gamma \ll \omega$ for the frequency range of interest, and so Equation 3-4 becomes

$$\epsilon_m(\omega) \approx 1 - \frac{\omega_p^2}{\omega^2}. \tag{3-5}$$

As is well known, (see, *e.g.,* [96]) conductors become transparent above the plasma frequency. Thus, inspection of Equation 3-4 reveals an important requirement on the dielectric function. In the transparency regime, $\omega > \omega_p$, so $\epsilon_m(\omega) > 0$. Obviously, SPP propagation is not supported at frequencies for which the conductor supports freely propagating EM modes. (This is evident if we recall that confinement at the interface requires that the SPP electric field $\vec{E_{SPP}}$ decays exponentially into the bulk of the conductor.) Below the transparency regime, by contrast, $\omega < \omega_p$, and $\epsilon_m(\omega) < 0$. Negative $\epsilon_m(\omega)$ is a necessary (but not sufficient) requirement for SPP propagation.

Figure 3.3 compares the model derived in Equation 3-5 to experimental data for Ag. The figure is taken from reference [97], and uses the symbol ϵ_1 in place of the symbol ϵ_m used elsewhere here. The dielectric function is plotted against the freely propagating wavelength $\lambda = \frac{2\pi c}{\omega}$. As can be seen, the free-electron model (dash-dotted line) correctly predicts the trend of the real part of the dielectric function. The most important observation to be made from this figure is that the negative real part of the dielectric function becomes extremely large at long wavelengths. Notice also that the complex part of the dielectric function, signifying damping, maintains a relatively small value across the range of wavelengths shown here. Ag manifests unusually low damping, as will be discussed below.

Figure 3.2 qualitatively shows the SPP dispersion relation (red solid line) from Equation 3-1. In the limits of large and small k_x, the SPP dispersion asymptotically approaches the linear functions indicated by dashed lines in

the figure. The limiting behavior in each of these cases needs to be examined separately.

Consider first the small-k_x limit, with reference to Equation 3-1. We recall that ϵ_m in this equation is wavelength-dependent. Since $\epsilon'_m(\omega)$ is large at small k_x (*i.e.,* large λ), Equation 3-1 approaches $k_x \approx \frac{\omega}{c}\sqrt{\epsilon_d}$. ϵ_d is typically on the order of $1 \sim 10$, so k_x in this limit is close to its value for a freely propagating EM wave. The significance of this fact becomes clear if we consider Equation 3-2: large $-\frac{\epsilon_m}{\epsilon_d}$ implies $k_{mz} \gg k_{dz}$. Thus, the decay length $\delta_m = \frac{1}{k_{mz}}$ in the conductor is very short, while the decay length $\delta_d = \frac{1}{k_{dz}}$ in the dielectric can be relatively long. It is clear that in the limit of small k_x the SPP mode increasingly resembles an uncoupled EM mode propagating parallel to the interface, with the speed of propagation approaching c.

Now consider the other limiting case, the large-k_x (small λ) limit. By examination of Figure 3.2, we can see that the magnitude of $-\epsilon_m$ is of the same order as ϵ_d in this regime. Turning again to Equation 3-1, k_x becomes very large when $-\epsilon_m$ is close to ϵ_d. To explore the consequences of this fact, take the limiting case where $-\epsilon_m = \epsilon_d$, and substitute this into Equation 3-5. We immediately find that $\omega = \frac{\omega_p}{\sqrt{1+\epsilon_d}}$. Since ϵ_d is on the order of 1, the literature often gives this frequency as

$$\omega_{sp} = \frac{\omega_p}{\sqrt{2}}. \tag{3-6}$$

ω_{sp} is referred to as the "surface plasmon frequency," and is the asymptotic

limit of large k_x, as shown in Figure 3.3. It is the source of the $\frac{\omega_p}{\sqrt{2}}$ dependency observed by Ritchie.

Another important consequence of large k_x, where $-\epsilon_m \approx \epsilon_d$, is that Equation 3-2 gives $k_{mz} \approx k_{dz}$. Thus, the decay length on each of the two sides of the interface is approximately equal. Assuming that optical losses in the dielectric are low, most SPP damping takes place in the conductor. Therefore, significant penetration depth into the conductor causes high losses. For this reason, large-k_x SPPs are characterized by shorter propagation lengths than SPPs with smaller values of k_x.

The large-k_x divergence of the SPP dispersion from the dispersion of freely propagating light (*i.e.,* the "light line") explains a fact already mentioned, that the wavelength of SPPs can be much shorter than that of freely propagating EM waves at the same frequency. As can be seen in Figure 3.3, the SPP wavevector becomes extremely large as the frequency ω approaches ω_{sp}, while the wave vector for freely propagating light increases only linearly in ω.

There is another important fact that stems from the divergence of the SPP dispersion from the light line. We observe that for every ω, with the exception of $\omega = 0$, the light line is characterized by a smaller wave vector—and hence a larger momentum—than the SPP at the same frequency. Therefore, direct coupling between freely propagating modes and SPP modes is forbidden by conservation of momentum. However, there are means of mediating such coupling for device applications. For example, if a prism situated close to the

conducting interface is illuminated at an angle such that total internal reflection occurs at the surface adjacent to the conductor, the evanescent field at the surface of the prism can couple to SPP modes. In this case, the SPP wave vector is related to the wave vector inside the prism by $k_x = k_{prism}\sqrt{\epsilon_d}\cos\theta$, where θ is the angle that the EM field in the prism makes with the normal to the surface of the conductor.[95] Alternatively, if the conducting surface is patterned with a periodic structure—suppose, for simplicity, a 1D structure with period a—the plasmon dispersion line folds over the first Brillouin zone $\frac{\pi}{a}$, and SPP resonances can be excited at discrete wave vectors:

$$k_x = \frac{\omega}{c}\sin\theta \pm n\frac{2\pi}{a}. \tag{3-7}$$

θ is the angle that the incident EM field makes with the normal to the conducting surface. This "grating coupling scheme" will be described in Chapter 7. Freely propagating EM modes can also couple to SPPs by scattering from surface roughness or intentionally fabricated individual structures. In this case, inelastic scattering provides the needed momentum difference Δk_x: $k_x = \frac{\omega}{c}\sin\theta \pm \Delta k_x$.[95, 101]

3.3 Plasmonic Damping

In the preceding discussion the effects of plasmonic damping were, for the most part, assumed to be negligible. This allowed us to establish a simple intuitive picture of plasmonic coupling to freely propagating EM fields. How-

ever, there are many systems of interest where damping can be considerable. Furthermore, the realization of device applications requires a full understanding of plasmonic damping. Therefore, the basic theoretical picture already developed should be supplemented with a brief overview of damping mechanisms.

Plasmonic damping has a number of causes. Chief among these is Ohmic loss in the conductor. This is primarily due to scattering of conduction electrons by ions in the crystal lattice, although electron-electron scattering and electron-phonon scattering also contribute.[68, 102] Ohmic losses are described by the non-zero (positive) imaginary part of the dielectric function.

Another source of loss is radiation leakage. This occurs when SPPs propagate at the surface of a film whose thickness is similar to, or less than, the penetration depth of the electric field into the conductor (*e.g.,* about 25 nm for Ag in the visible and infrared regimes[97]). For such thin films, the electric field of the SPP extends (leaks)through the film and into the substrate. The SPP wave vector $\vec{k_x}$ is different from the wave vector of the associated EM field in the substrate. If at a particular frequency $\vec{k_x}$, $\vec{k_{sub}}$, and $\vec{k_{vac}}$ represent the wave vectors corresponding to that frequency in the SPP, substrate, and vacuum, respectively, then $Re(k_{sub}) = n_{sub}k_{vac}$. n_{sub} is the index of refraction of the substrate at frequency ω. Then phase matching dictates a particular angle α, relative to the normal with the interface, at which radiation leakage propagates: $k_x = n_{sub}k_{vac}\sin\alpha$. Figure 3.4 is a schematic illustrating the relationship between $\vec{k_x}$ and $\vec{k_{sub}}$.

Three-dimensional features on a conductor's surface—either random roughness or individual features—can also constitute loss channels. Just as inelastic scattering of incident light can provide the momentum contribution Δk_x needed for a freely propagating mode to couple to SPPs, inelastic scattering of SPPs can mediate coupling of SPPs back into freely propagating EM modes.[95] This loss mechanism will be discussed in detail in Chapter 7.

Finally, interband transitions have been entirely excluded from the foregoing discussion but are important sources of loss in real systems. They will be treated in the next section.

3.4 Materials for Plasmonic Applications

Not every conductor is a suitable platform for SPP-based devices. A number of factors influence the plasmonic lossiness of a material and the dependence of loss on wavelength. Furthermore, it is necessary to consider whether a material is safe for research and practical for device applications.

For example, consider a subset of metals known for their high conductivity: Ag, Au, Cu, and Al. All exhibit low Ohmic losses and are safe for use. If we define Γ as the total damping rate due to electron-electron scattering, electron-ion scattering, and inelastic scattering from defects and grain boundaries, Ag has the lowest value of Γ and is thus the best conductor.[68]

Another consideration, however, is the real part of the dielectric function, $\epsilon'_m(\omega)$. From Equation 3-2 above, $\frac{k_{mz}}{k_{dz}} = -\frac{\epsilon_m}{\epsilon_d}$. Also, we saw that

$k_{mz} \gg k_{dz}$ implies that $\delta_d \gg \delta_m$. Therefore, ϵ'_m of large magnitude means that there is low confinement in the conductor, resulting in reduced losses. Because $\epsilon'_m(\omega) \approx 1 - \frac{\omega_p^2}{\omega^2}$, maximizing the magnitude of ϵ'_m requires that ω_p be maximized: in short, large ω_p implies that losses are low. Of the four metals considered here, Al has the highest plasma frequency with $\hbar\omega_p = 12.7eV$, and Ag has the second highest, with $\hbar\omega_p = 9.2eV$.

Another important consideration is the energy at which loss due to interband transitions starts to occur. In Au and Cu interband transitions become important at 2.3 and 2.1 eV, respectively, meaning that Au and Cu can support low-loss SPP propagation only in the infrared (IR) regime. The interband transition energy for Al is even lower, at 1.41 eV.

These considerations are summarized in Table 3.1, adapted from West *et al.* [68] Aside from the issues just described, an additional disadvantage of Cu and Al is that both oxidize quickly. Because of its low damping, high interband transition energy, high plasma frequency, and relative chemical inertness, Ag is generally considered to be the optimal metal for plasmonic applications, although applications in the IR frequently make use of Au as well.

Among the alkali metals, Na and K exhibit low losses comparable with those of Ag. However, the challenges of probing these materials in vacuum and the impossibility of out-of-vacuum device applications have limited the research that has been done in this area. Figure 3.5 shows a side-by-side comparison of the real and imaginary parts of the dielectric function for Ag, Au, Al, Na, and K. In Fig. 3.5(b) the properties of Na and K are comparable

Metal	$\hbar\omega_p$ (eV)	Γ (eV)	Onset of Interband Transition (eV)
Silver (Ag)[100, 103, 104]	9.2	0.02	3.9
Gold (Au)[100, 104]	8.9	0.07	2.3
Copper (Cu)[100, 103, 104]	8.7	0.07	2.1
Aluminum (Al)	12.7	0.13	1.41

Table 3.1: Comparison of onset energy for three sources of loss in SPPs propagating in highly conductive metals. Γ is the total damping rate due to electron-ion scattering, electron-electron scattering, and inelastic scattering from defects and grain boundaries. Interband transitions prevent all but Ag from being useful for SPP devices in the visible range. Adapted from [68].

with those of Ag, but in Fig. 3.5(a) Ag is clearly superior.

Additional materials aside from elemental metals have been investigated. Attempts have been made to tune the band structure of Au with transition metals and alkali metals. Despite promising preliminary results and intriguing theoretical proposals, film growth remains challenging; moreover, the alloying can lead to additional and undesirable effects on the electron band structure.[68, 105, 106] Semiconductors have also been studied. For a semiconductor to act as a low-loss plasmonics platform, it needs to have a bandgap larger than the energy range of interest, and it also needs to be very highly doped. Such high doping has been a challenge: for example, InGaAs was reportedly doped as high 7×10^{18} cm^{-3} and supported SPP coupling in the 9–12 μm range, but to extend the range of operation into the visible regime, doping of 3×10^{20} cm^{-3} would be required. What fraction of dopants would be active at such a concentration, and what the carrier mobility might be, are important unanswered questions.[68, 107] At present, the two best candidates

for non-metallic low-loss SPP platforms appear to be indium tin oxide (ITO), which supports low-loss propagation comparable to Ag in both the visible and near-infrared (NIR) regimes,[108–111] and graphene, which is predicted to exhibit excellent low-loss characteristics in the THz regime and intriguing SPP modes not observed in metals.[68, 112, 113] However, the field of graphene plasmonics remains in its infancy, with many theoretical predictions as yet untested.

With metallic SPP platforms, one of the primary issues has been producing and probing flat, smooth films. This is particularly true of Ag films, and was discussed in detail in Chapter 1. Because of the challenges of Ag film growth and stabilization, most plasmonics studies to date have used thermally evaporated polycrystalline films rather than smooth epitaxial films. However, as explained above (Section 3.3), inelastic scattering from surface features allows SPPs to couple into freely propagating light, and can constitute a significant loss mechanism in rough films. Both poor film quality and lack of robustness in Ag film are widely recognized as a major hindrances to the development of low-loss plasmonic devices (*e.g.,* [68]). As an illustration, Fig. 3.6 shows atomic force microscopy (AFM) data from typical epitaxial (left) and polycrystalline (right) films. The polycrystalline film was produced by thermal evaporation onto the native oxide layer of a Si(111) wafer at a base pressure in the low 10^{-6} Torr range. No attempt was made to control the substrate temperature during deposition of the polycrystalline film. The differences in roughness and surface morphology are obvious; the false-color scale has been

adjusted in each case to allow surface features to be seen. The epitaxial film follows the underlying Si steps, and the pale patches on each terrace are 1-ML-high islands. The polycrystalline film exhibits rough morphology: there are deep holes and rounded clumps with diameters on the order of tens of nm. Thus, losses due to inelastic scattering can be high on film of this type.

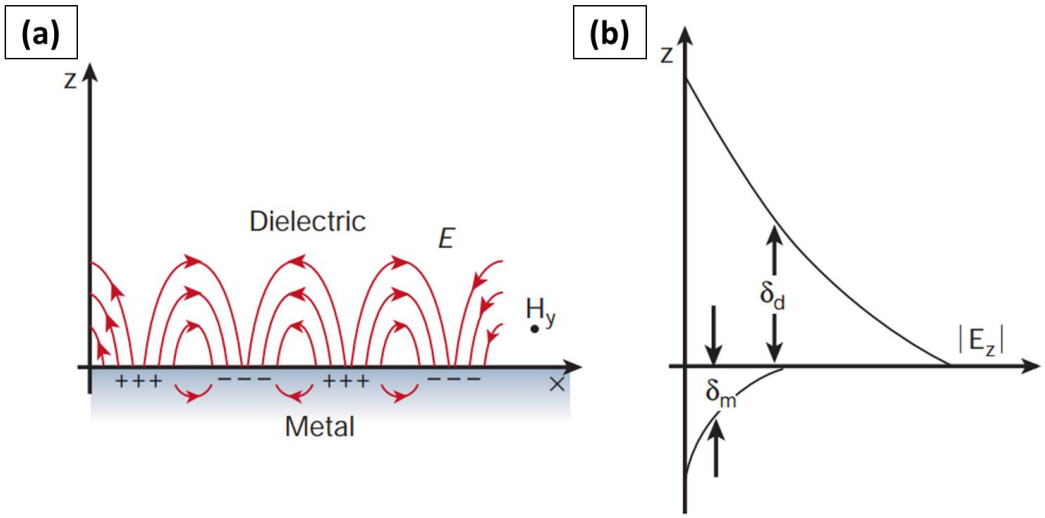

Figure 3.1: Reprinted by permission from Macmillan Publishers Ltd.: *Nature* [94], copyright 2003. Original caption: (a) Surface plasmons at the interface between a metal and a dielectric material have a combined electromagnetic wave and surface charge character. They are transverse magnetic in character ($\vec{H}$ is in the y direction), and the generation of surface charge requires an electric field normal to the surface. (b) This combined character also leads to the field component perpendicular to the surface being enhanced near the surface and decaying exponentially with distance away from it. The field in this perpendicular direction is said to be evanescent, reflecting the bound, non-radiative nature of surface plasmons.... In the dielectric medium above the metal...the decay length of the field [is] δ_d, whereas the decay length into the metal, δ_m, is determined by the skin depth.

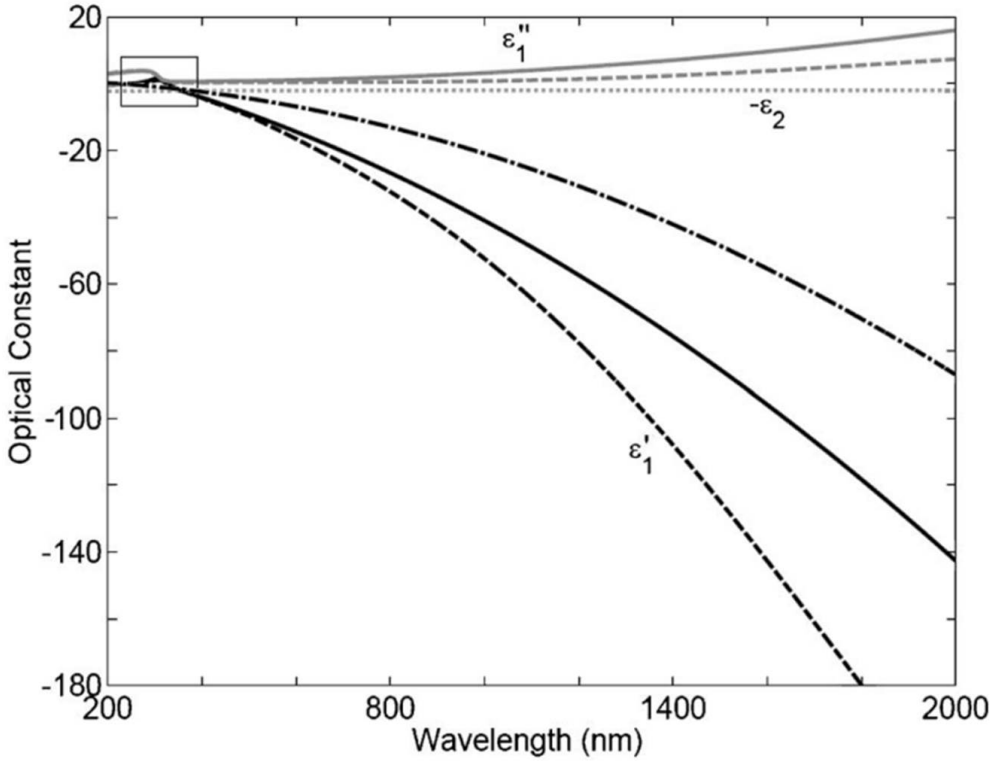

Figure 3.2: Reprinted figure with permission from [97]. Copyright 2005 by the American Physical Society. Original caption: The real and imaginary components of the Ag dielectric function ($\epsilon_1 = \epsilon_1' + \imath\epsilon_1''$) using a free-electron model (dash-dot line type), data from Johnson and Christy (dashed) and the Palik Handbook (solid). For reference, the polynomial fit through Palik's SiO_2 data is also included (dotted, plotted as $-\epsilon_2$). The [boxed region encloses] the region of anomalous dispersion for the Johnson and Christy and Palik data sets.[98–100]

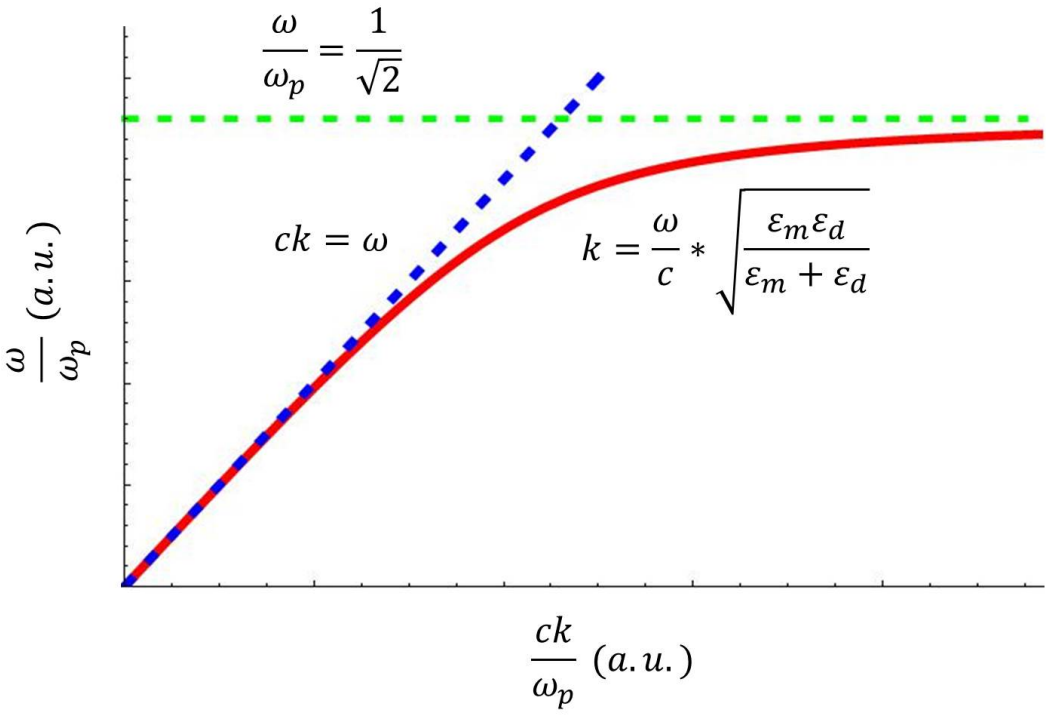

Figure 3.3: Qualitative depiction of the SPP dispersion relation, $k_x = \frac{\omega}{c}\sqrt{\frac{\epsilon_m \epsilon_d}{\epsilon_m + \epsilon_d}}$, shown as a solid red line. The blue dashed line is the dispersion relation for uncoupled light propagating freely in vacuum. The green dashed line is the surface plasmon frequency, $\frac{\omega_p}{\sqrt{2}}$.

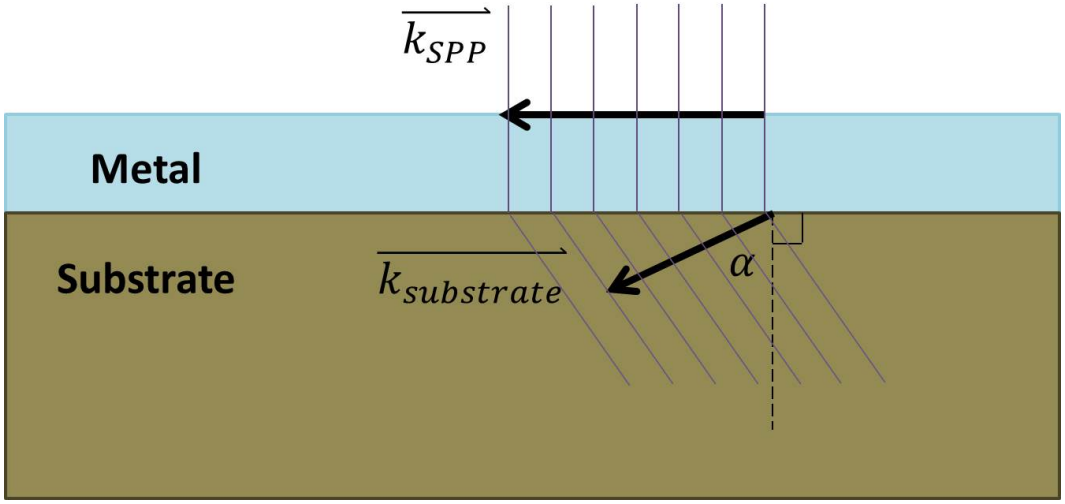

Figure 3.4: Schematic of leakage into substrate. The index of refraction in the substrate and the requirement for phase matching dictate the angle α of radiation leakage.

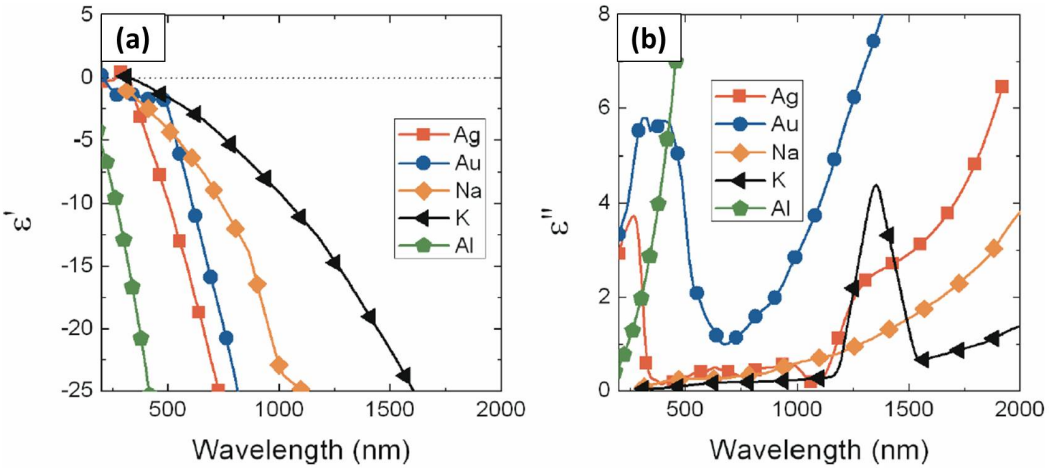

Figure 3.5: From [68]. (a) Real part of the dielectric function for Ag, Au, Na, K, and Al: negative values of large magnitude are associated with reduced SPP lossiness. (b) Imaginary part of the dielectric function for the same metals: small positive values are associated with reduced SPP lossiness. Reproduced with permission.

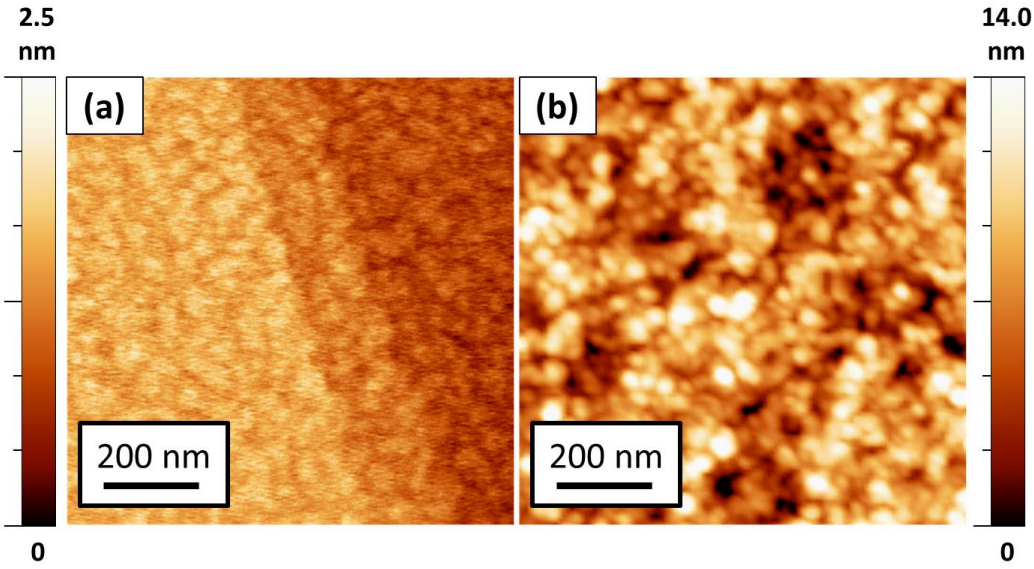

Figure 3.6: Reprinted with permission from [114]. Copyright 2012 American Chemical Society. Atomic force microscopy (AFM) images showing the contrast between atomically smooth epitaxial Ag film and rough thermally evaporated film. Left: epitaxial Ag(111) film on Si(111). Right: thermally evaporated Ag film on SiO_2. Scattering from surface roughness is a major source of loss for SPPs propagating in thermally evaporated film. Reproduced with permission.

Chapter 4

Analysis Techniques

4.1 Scanning Probe Microscopy

Scanning probe microscopy (SPM) allows for non-destructive, high-resolution (up to atomic scale) interrogation of surfaces. SPM techniques are based on the rastering of a probe across a surface of interest: therefore, data acquisition can be slow. However, SPM has tremendous power for probing topographic, electronic, and magnetic features with resolution as good as, or better than, the atomic scale.

4.1.1 Scanning Tunneling Microscopy

Scanning tunneling microscopy (STM), developed and first implemented by G. Binnig, H. Rohrer, Ch. Gerber, and E. Weibel at IBM Zurich in 1982, is a surface science technique for probing a sample's topography and electronic structure with atomic or better resolution. It is typically used to interrogate conductive, solid-state structures in ultra-high vacuum (UHV) environments. When an atomically sharp conductive tip is brought sufficiently close to the surface of a sample, typically to within a few $\mathring{A}$, conduction electrons in the tip and sample can tunnel through the potential barrier that is the vacuum region between them. When a tip-sample voltage is applied (generally no

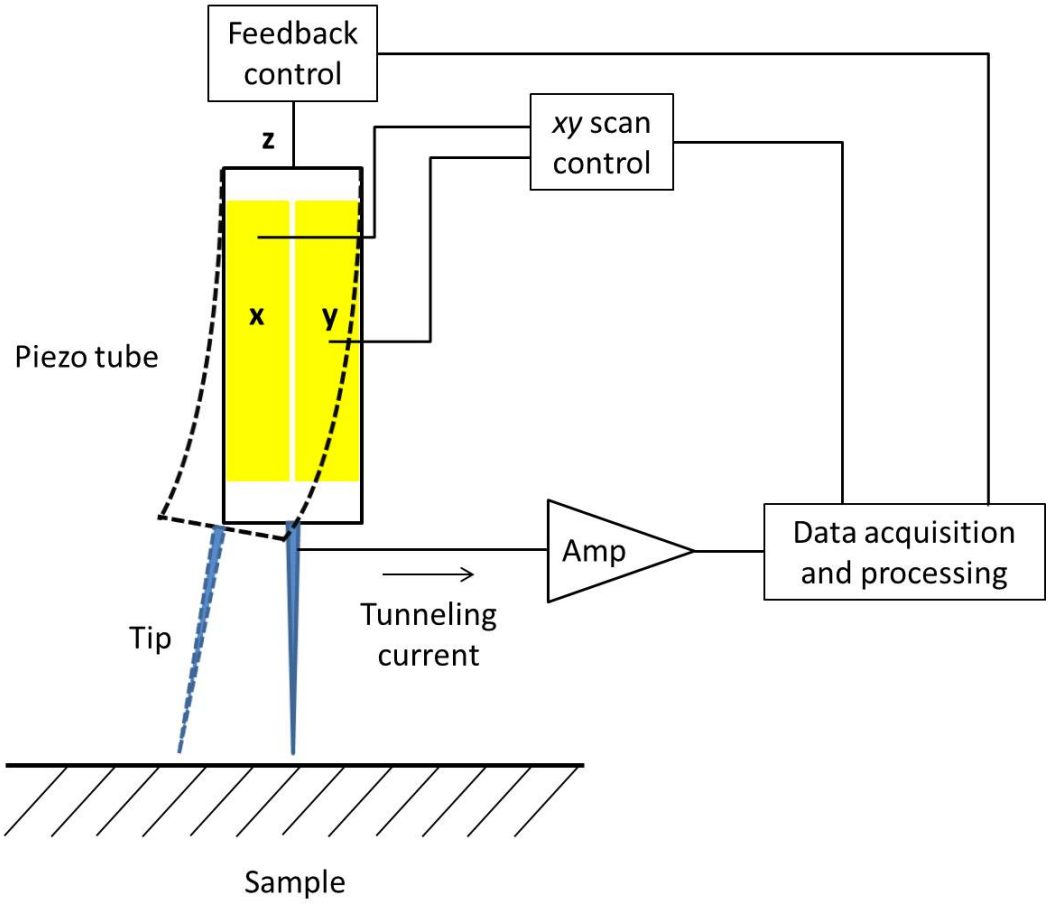

Figure 4.1: Schematic of STM. Not to scale. See text for details.

more than a few volts), a net tunneling current results. The magnitude of this current (typically on the order of 1∼100 pA) is a function of tip-sample separation, as well as of the local electronic structure of the sample near the tip. A schematic—not to scale—is shown in Fig. 4.1.

In the usual implementation of this technique, the tip is attached to a quartered piezoelectric tube[115] that allows its position to be controlled in x,

y, and z. In Fig. 4.1 yellow rectangles symbolize the electrical contacts (often Au) that allow voltage to be applied to the four quarters of the tube to induce it to bend in $\pm x$ and $\pm y$ and raster the tip over the sample surface. Voltage applied along the long axis of the tube (z) causes the tube to stretch. In the most common mode of operation, feedback electronics monitor the tunneling current and apply voltage to extend or retract the tip so that it maintains a constant set-point tunneling current. Data acquisition software records tip height as a function of (x,y) position on the sample surface. This "constant current mode"is the mode used in the experiments described here. Alternatively, in "constant height mode" tip height can be maintained constant with the data acquisition software recording tunneling current as a function of (x,y) position on the sample surface. In order to accurately monitor and control tip height and lateral position, vibrational isolation of the STM scan head is critical. Since tunneling current changes exponentially with the thickness of the tunneling barrier (*i.e.,* tip height above sample surface), a small change in tip-sample distance results in a large change in current.

The greatest power of STM lies not so much in topographic as in spectroscopic analysis—*i.e.,* scanning tunneling spectroscopy (STS). Interpretation of STM and STS data requires on a theoretical understanding of tunneling theory. The Bardeen approach is among the most frequently used,[116] and is set forth clearly by C. J. Chen.[115] Following Chen's exposition, Fig. 4.2 illustrates Bardeen's approach, which sidesteps the difficult problem of solving the Schrödinger equation for the complete tip-sample system by treating the

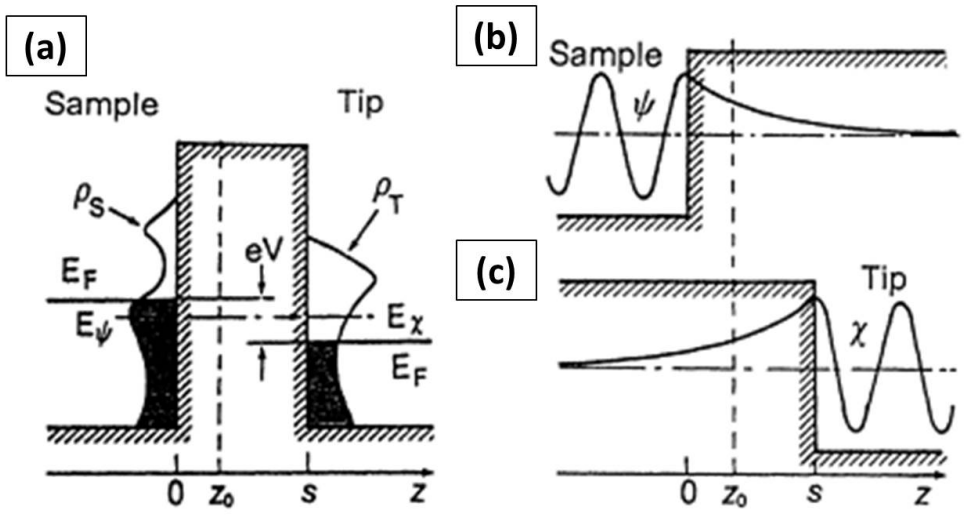

Figure 4.2: From [115]. Original caption: The Bardeen approach to tunneling theory. Instead of solving the Schrödinger equation for the coupled system, (a), Bardeen (1960) makes clever use of perturbation theory. Starting with two free subsystems, (b) and (c), the tunneling current is calculated through the overlap of the wavefunctions of free systems using the *Fermi golden rule*. Reproduced with permission.

tip and sample as two separate subsystems and solving the time-independent Schrödinger equation for each.

Assuming the time-independent solutions can be found—for many common cases, they can—Figs. 4.2(b) and (c) show the approach schematically, with ψ and χ representing stationary electronic states in the sample and tip, respectively, corresponding to eigenenergies E_ψ andE_χ. The density of stationary states is ρ_S in the sample and ρ_T in the tip; the cartoon in Fig. 4.2(a) shows these densities of states for a hypothetical system. Then, Bardeen argued, the probability of tunneling between any two particular states ψ and χ

is determined by the overlap of their wave functions at a separation surface z_0 inside the barrier. The total tunneling current is found by summing these probabilities over all states. More rigorously, we can take the tunneling matrix element to be

$$M = \frac{\hbar}{2m} \int_{z=z_0} (\chi^* \frac{\partial \psi}{\partial z} - \psi \frac{\partial \chi^*}{\partial z}) dS. \tag{4-1}$$

The integral is over a separation surface at $z = z_0$, the choice of which does not have a large impact on the outcome of the calculation.[115] Electron transfer obeys the Fermi golden rule, so the probability of an electron in state ψ tunneling into state $\chi*$ is $\frac{2\pi}{\hbar}|M|^2\delta(E_\psi - E_\chi)$. The sum over all states is

$$I = \frac{4\pi e}{\hbar} \int_{-\infty}^{+\infty} [f(E_F - eV + \epsilon) - f(E_F + \epsilon)] \rho_S(E_F - eV + \epsilon) \rho_T(E_F + \epsilon) |M|^2 d\epsilon, \tag{4-2}$$

where $f(E)$ is the Fermi distribution function. Making the assumptions that $k_B T$ is small compared to the required energy resolution, and that $|M|$ is approximately constant in the energy interval of interest, this statement can be approximated as

$$I \propto \int_0^{eV} \rho_S(E_F - eV + \epsilon) \rho_T(E_F + \epsilon) d\epsilon. \tag{4-3}$$

The tunneling current depends on the electronic density of states (DOS) in both the tip and the sample. For a tip consisting of a free-electron-like

metal, ρ_T is approximately constant, so $\frac{\partial I}{\partial V} \propto \rho_S(E_F - eV)$. Thus, STS, which consists in sweeping voltage at a fixed tip height while measuring tunneling current to determine $\frac{\partial I}{\partial V}$, directly probes the local electronic density of states (LDOS) in the sample.

Other types of spectroscopy are also used: for example, the tip height can be swept while voltage is held fixed. However, these methods were not used in my experiments. Detailed treatment can be found in Refs. [115, 117].

I have made all the measurements described here on metallic or doped semiconductor substrates in a home-built low-temperature STM (LT-STM) system (Pan-type walker, PbZrTi (PZT) scan tube). Chamber pressures were typically in the 10^{-11} Torr range during scanning. I used both electrochemically etched tungsten (W) tips and platinum iridium (PtIr) tips prepared by mechanical methods. The sample temperature during scanning was approximately 78 K. The chamber is mounted on an air table for vibrational isolation. The system is contolled by an RHK SPM-100 controller package. Data analysis was performed using the WSxM software package by Nanotec Electronica.[118]

4.1.2 Atomic Force Microscopy

Like STM, atomic force microscopy (AFM) is a surface-sensitive technique capable of atomic resolution. AFM was developed by G. Binnig and C. F. Quate in 1986 to circumvent STM's requirements for sample conductivity.[119] AFM interrogates tip-sample force interactions (primarily van der

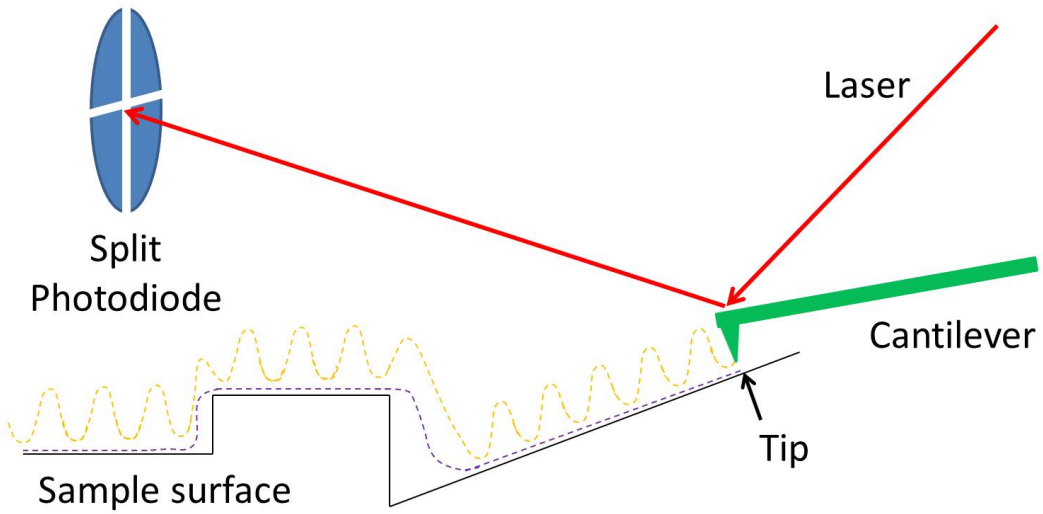

Figure 4.3: Schematic of AFM. Not to scale. Purple dashed line shows tip motion for contact mode, while yellow dashed line shows tip motion for tapping mode. See text for details.

Waals,[117] though a variety of magnetic and electrostatic interactions can be probed), and unlike STM does not normally provide information about electronic structure. A schematic (not to scale) is in Fig. 4.3. Cantilever dimensions are typically on the order of hundreds of μm, and the photodiode commonly sits at a distance of a cm or more from the cantilever. Sample surface roughness can be on the scale of μm to $\mathring{A}$.

The surface is probed by the atomically sharp tip etched at the end of the flexible cantilever. There are many possible modes of operation, and most of these can be broadly categorized either as "contact" or "tapping." Contact mode entails dragging the tip over the sample while recording deflection of the cantilever as a function of lateral position. The disadvantage of contact

mode for many applications is that the tip can damage the sample. In tapping mode, which is the mode used in the studies described here, a piezoelectric element drives the cantilever at its resonant frequency. The tip is brought near the surface of the sample where tip-sample interactions modify the resonant frequency of the cantilever without the tip actually touching the sample. The neutral tip position—*i.e.,* the height of the unflexed cantilever above the sample surface—might be on the order of 1–10 nm; however, ideal tip position varies greatly depending on the sample being probed and the specifications of the cantilever. One does not generally want the tip to "snap to" sample contact, and therefore one must increase or decrease the separation to take account of cantilever elasticity and the magnitude and range of the forces acting between tip and sample.[120] Because contact is minimal, tapping mode is the mode of choice for delicate samples. The motions of the cantilever—in particular, its frequency and amplitude of oscillation—are monitored, and the tip height is adjusted by feedback electronics which maintain a setpoint vibration amplitude chosen by the user. In this way the tip tracks the sample's topographical features (see Fig. 4.3), and control software records tip height z along with a variety of other parameters including oscillation amplitude, frequency, and phase shift as a function of lateral position (x,y). The most common means of detecting cantilever position is optical: a laser is focused on the back of the cantilever, which is polished to a mirror finish for this purpose. The laser's angle of incidence is adjusted so that when the cantilever is in its neutral, unflexed position the reflected laser spot falls at the center

of a circular photodiode detector divided into four quadrants. See Fig. 4.4. As the cantilever moves, the laser spot moves up and down or left and right from its neutral position at the center, thus changing the voltages detected at each of the four photodiodes in a manner that allows the cantilever's motion to be determined by the control computer. If the four diodes are labeled as in Fig. 4.4, and if diodes 1, 2, 3, and 4 generate voltages V_1, V_2, V_3, and V_4, respectively, then vertical cantilever motion is detected as $(V_1+V_2)-(V_3+V_4)$ and horizontal motion as $(V_2+V_3)-(V_1+V_4)$. Vertical cantilever motion is cantilever flexion, the primary interest in most tapping-mode AFM measurements. Horizontal motion is torsional cantilever motion. Since most AFM setups scan in a direction perpendicular to the long axis of the cantilever, torsion results from drag on the cantilever.[121]

AFM can be more tolerant than STM of out-of-vacuum operation. However, if atomic resolution is to be obtained, UHV is usually necessary. Like STM, AFM requires vibrational isolation to maximize resolution and prevent tip crashes. The measurements described here were obtained in ambient conditions (approximately standard temperature and pressure) with a Veeco Multi-mode V commercial AFM setup and dedicated Veeco controller/software package. A BM-4 Biscuit vibration isolation platform from Minus K Technology served for vibrational isolation. I acquired data in tapping mode using etched Si tips. Tips were model TESP from Brüker, with specified resonant frequency between 306 and 350 kHz and spring constant k=20–80 N/m. Veeco tips with matching specifications were also used. Data were analyzed in the

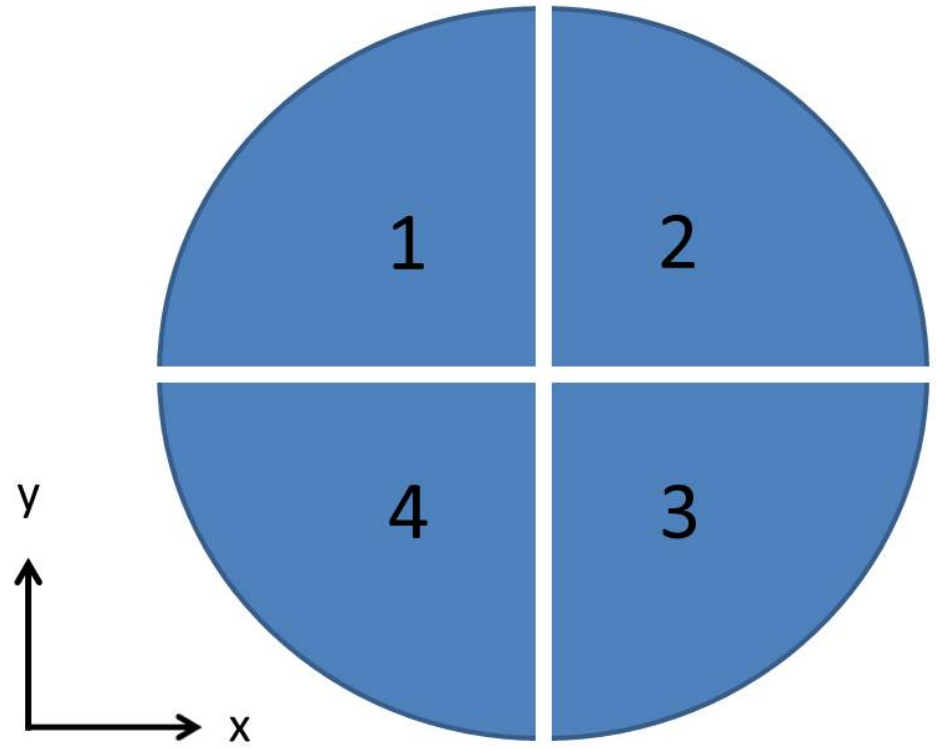

Figure 4.4: Schematic of split photodiode for AFM. The quadrants have been arbitrarily numbered for reference in the text.

WSxM software package by Nanotec Electronica.[118]

4.2 Electron Diffraction Techniques

The use of electron diffraction to investigate crystalline structure originated in the early twentieth century with the pioneering work of C. J. Davisson and L. H. Germer on low-energy electrons, and the independent work by G. P. Thomson on high-energy electrons. Thomson and Davisson shared the Nobel

Prize in 1937 for the "discovery of the interference phenomena arising when crystals are exposed to electronic beams."[122] However, practical crystallographic analysis, especially by diffraction of low-energy electrons, remained for a long time imperfectly realized, due to the difficulties of preparing and maintaining a clean surface. In the 1960s, with improved vacuum conditions and innovation in surface preparation techniques (*e.g.,* ion bombardment and sample flashing), electron diffraction came into its own as a foundational technique in surface science.[123]

The physics of low energy electron diffraction (LEED) and reflection high energy electron diffraction (RHEED) are extremely similar to one another, as are the applications to surface science. The geometries, however, are different, and there are key differences in the information that can be extracted from each technique.

4.2.1 Low Energy Electron Diffraction: Basic Setup and Operation

A typical LEED setup (not to scale) is shown in Fig. 4.5. An electron gun—consisting of a heated cathode and a series of grids to accelerate and focus the electrons that boil off the cathode—creates an electron beam with relatively small energy spread, on the order of a tenth of an eV, and divergence less than 10.[123] The beam emerges with energy on the order of tens to hundreds of eV into a field-free region where it interacts with the sample. Because the electrons have low energy they interact mainly with the surface and penetrate only slightly (a few atomic layers) into the bulk.[124] At the

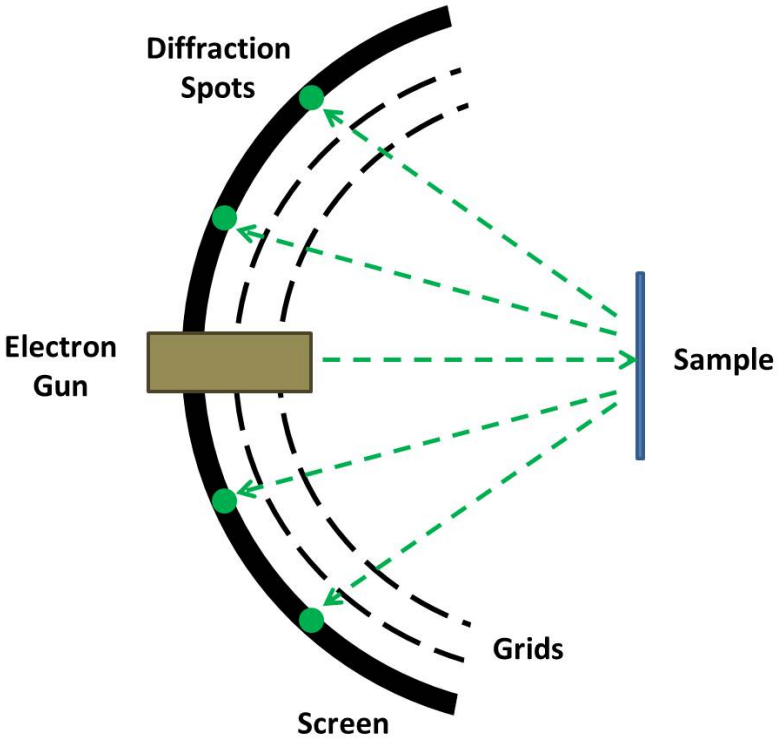

Figure 4.5: Schematic of LEED. Not to scale. For clarity, only two grids are shown: typical systems contain 3–4 grids. See text for details.

sample surface the incident beam can have a diameter on the order of mm, but the coherence width is typically much less, potentially as small as several hundred $\mathring{A}$.[123, 124] After interacting with the sample surface, the electrons scatter back to a phosphorescent screen. The resulting pattern on the screen can be observed from either the gun side or sample side, depending on the design of the system, and can be recorded with a simple camera setup. The

configuration in which the screen is viewed from behind the gun is known as "reverse-view" setup.

In front of the screen there is a set of concentric grids, shown symbolically by two dashed semicircles in the schematic in Fig. 4.5. The most important of these is the innermost grid, which is maintained at a potential equal to that of the sample so the region in which electrons interact with the sample is field-free, and one or two retarding grids, which apply a retarding potential to prevent inelastically scattered electrons from reaching the screen. At the low energies at which LEED operates, inelastic scattering can be significant. By discarding inelastically scattered electrons the retarding grid allows for a simple LEED pattern that can be interpreted purely in terms of elastic scattering processes. The physics of elastic scattering will be discussed below. The phosphorescent LEED screen is at high potential, on the order of a few kV, so electrons passing through the retarding grid are reaccelerated to a high enough energy to efficiently excite the phosphor.

Only samples that possess long-range order exhibit LEED patterns. High-quality samples yield sharp LEED patterns with strong contrast between pattern and background. Defects reduce sharpness and contrast. Therefore, LEED is generally performed in vacuum, to slow the rate of accumulation of surface adsorbates. Since the electron beam scarcely penetrates past the sample surface, LEED only allows for analysis of the surface structure: it gives little to no information about the bulk.

My experiments were performed with a commercial reverse-view LEED

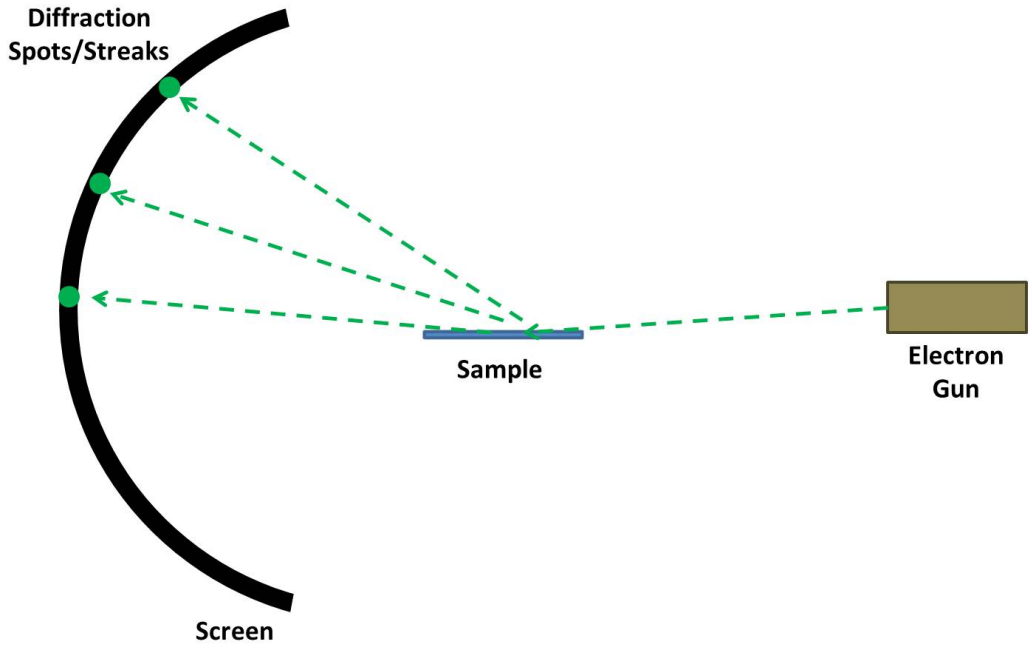

Figure 4.6: Schematic of RHEED. Not to scale. See text for details.

from Princeton Research Instruments, Inc., model RVL 8-120. Data were acquired with a point-and-shoot digital camera (Canon PowerShot G6 with 7.1 megapixels and optical zoom) mounted on a tripod outside the chamber. All experiments took place at base pressures no higher than the low 10^{-10} Torr range.

4.2.2 Reflection High Energy Electron Diffraction: Basic Setup and Operation

A RHEED setup is shown in Fig. 4.6 (not to scale). As in the case of LEED, an electron gun consisting of a cathode and a series of grids and focus-

ing elements creates an electron beam with small angular divergence. Beam divergence on the order of 0.1 mrad as adequate for most applications.[125] There are two key differences between RHEED and LEED: first, the beam energies—RHEED operates in the range of tens of keV, as opposed to the tens of eV range of LEED; and second, the differing arrangements of gun, sample, and screen. LEED features a relatively compact geometry: the gun sits directly in front of the sample, separated from the sample by typically only several cm. The angle of beam incidence on the sample in LEED is not necessarily 90° and can in some setups be controlled, but incidence is usually close to normal. RHEED, by contrast, has an open geometry, as Fig. 4.6 shows. The beam encounters the sample at an oblique angle ($176° \sim 179°$), and the gun and screen are much farther from the sample than in LEED: the desirable RHEED spot size is about 0.1 mm at the screen, and this can be readily achieved by commercial systems with gun-screen distances of 40–70 cm.[125] The screen, as in the case of LEED, is phosphorescent, and can be monitored with a camera of any sort; the screen is typically nothing more than a standard viewport covered with phosphor (and with indium tin oxide (ITO) to prevent charging). Since the beam interacts with the sample at a low angle, the diffraction pattern observed on the screen is essentially a projection of the sample reciprocal lattice along the direction of the beam. Therefore, in order that the full surface symmetry can be seen, RHEED setups usually include a sample holder that can rotate azimuthally. Like LEED, RHEED is operated under vacuum to minimize accumulation of adsorbates on the sample surface.

Good vacuum conditions are also important in RHEED because of the long beam path, along which defocusing could potentially become problematic if there were significant scattering from particles.

Although the beam energy in RHEED is much higher than in LEED, penetration of the incident beam into the sample is generally no more than a few atomic layers.[125] This is because of the glancing angle of the beam: beam momentum in the direction normal to the sample face is minimal.

RHEED exhibits a greater sensitivity to surface morphology than does LEED. Sharp, well-defined diffraction spots arranged in an arc, with strong contrast relative to the background, are the sign of a perfectly flat crystalline surface. A very flat surface with small, out-of-phase domains smaller than the coherence length of the electron beam (typically 100–200 nm in the longitudinal direction and 30–80 nm in the transverse direction) is evidenced by elongation of the diffraction spots into streaks. Streak width and length allow for estimation of average domain size, with streak width scaling as $\frac{2\pi}{L_1}$ and streak length scaling as $\frac{2\pi}{L_2 tan\theta_i}$, where L_1 and L_2 are the average domain dimensions in the directions perpendicular and parallel to the incident electron beam, respectively, and θ_i is the glancing angle of the beam relative to the sample face.[125] In rough growth, transmission diffraction through three-dimensional (3D) surface features of small dimensions ($\leq$ 10 nm thickness) produces spots aligned along lines rather than arcs, with spot spacing inversely related to the spacing of atomic planes in the crystal.[126, 127] Additional diffraction patterns are possible: see *e.g.* Ref. [128].

My experiments were performed with a commercial 15-keV RHEED system from Staib Instruments. Path length from electron gun to sample is approximately 45 cm, and 37 cm the path length from sample to screen. The path length is slightly longer than optimal, resulting in a larger than ideal spot size on the order of a mm. However, for the present experiments spatial resolution is not critical and so beam defocusing is not limiting. The electron gun is shielded with a homebuilt MuMetal sleeve to reduce stray electromagnetic fields. For azimuthal sample rotation, the sample is mounted on a differentially pumped commercial manipulator by Thermionics, Inc., with xyz motion and 360° azimuthal rotation. Sample cooling and heating, as well as growth, can take place on the manipulator while monitoring with RHEED. Data were recorded with a kSA 400 imaging package from k-Space Associates, Inc. This package consists of a charge-coupled device (CCD) camera and k-Space's proprietary software package for real-time image analysis. All experiments were performed under UHV conditions, typically in the low- to mid-10^{-10} Torr range.

4.2.3 Fundamental Principles of LEED and RHEED

The Ewald construction provides a straightforward model for the physics of LEED and RHEED. It makes the following assumptions:

1. All inelastic scattering processes can be neglected, so $|\vec{k_f}| = |\vec{k_i}| = k$, where $\vec{k_i}$ and $\vec{k_f}$ are the incident and diffracted wave vectors, respectively. At RHEED energies, elastic scattering dominates inelastic, so

this assumption is justified. In LEED, inelastic scattering can be considerable, but the retarding grid prevents inelastically scattered electrons from contributing to the observed diffraction pattern.

2. Scattering of the incident electron beam by atoms in the sample lattice is coherent: *i.e.,* there is a fixed phase relationship between the incident and the scattered wave. This follows from the assumption of elastic scattering.

3. At the sample the incident electron beam can be approximated as plane waves. This is a reasonable assumption (considering the small interatomic dimensions upon which diffraction takes place) for many experimental setups if the electron gun is at least several cm away from the sample.

A simple case is depicted in Fig. 4.7. A plane wave, shown as originating from the upper left corner of the figure, is incident elastically with angle θ_i on a 1D square lattice with lattice constant a. Constructive interference occurs if $a\cos\theta_i + a\cos\theta_f = n\lambda$ where n is an integer that indexes a discrete set of angles θ_f at which constructive interference can be observed (*i.e.,* n is the order of diffraction). Rearranging this expression gives $k\cos\theta_i + k\cos\theta_f = n\frac{2\pi}{a}$. Observe that $\frac{2\pi}{a}$ is the reciprocal lattice for this structure.

Generalizing this treatment to three dimensions gives the Laue condition for constructive interference: $\vec{k_f} - \vec{k_i} = \vec{G_n}$, where $\vec{G_n}$ is any vector in

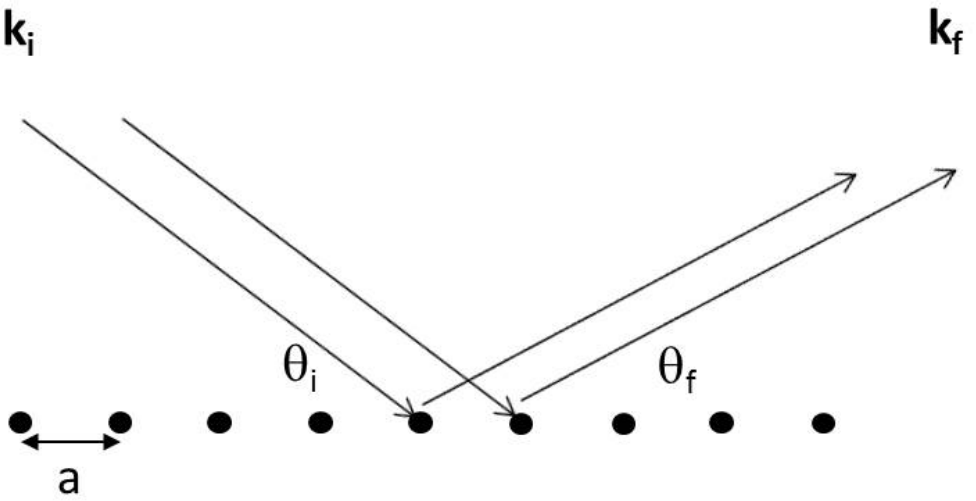

Figure 4.7: Plane wave incident on a 1D array of scatterers.

the reciprocal lattice of a 3D scattering structure. The Laue condition is illustrated in Fig. 4.8 for a square lattice (drawn in 2D for graphical simplicity). Because of the assumption of elastic scattering, $|\vec{k_f}| = |\vec{k_i}|$, both vectors can be represented as radii of the same sphere (or circle, in the 2D case as in Fig. 4.8). Assuming that $\vec{k_i}$ has a fixed angle and magnitude (determined by the beam energy $\frac{(\hbar k_i)^2}{2m_e}$, where m_e = electron mass), we graphically orient $\vec{k_i}$ to point to some reciprocal lattice point. Then the condition for constructive interference is satisfied when $\vec{k_f}$ takes any angle at which it points to a reciprocal lattice point: *i.e.,* any angle at which a reciprocal lattice point sits on the boundary of the sphere (circle). One such angle is illustrated in Fig. 4.8.

Fig. 4.9 depicts the Ewald sphere in 3D, for diffraction from a 1D lattice. Notice that the size of the Ewald sphere relative to the lattice spacing

is not to scale for a real atomic lattice: the planes are drawn with a large spacing, in order to make the diagram clear. The Laue condition is satisfied for any of the circular cross sections created by the intersection of the Ewald sphere with one of the reciprocal lattice planes. The Laue circles formed at the intersections of the sphere and planes constitute the distinctive arc-shaped pattern typical of RHEED data.

If instead the lattice is 2D, the lattice planes in Fig. 4.9 are replaced by rods periodic in two dimensions. Then the Laue condition implies that each order of diffraction, rather than being the edge of a circle, will be a set of periodic points along the edge of the circle. This is what is seen in RHEED data for smooth crystalline surfaces. Notice that in Fig. 4.9 both $\vec{k_i}$ and $\vec{k_f}$ point to the right (into the reciprocal lattice planes). This is correct for RHEED geometry. For LEED geometry the figure would be modified so that one of $\vec{k_i}$, $\vec{k_f}$ pointed up and the other down. The resulting LEED diffraction pattern consists of the points formed by the reciprocal lattice rods piercing the bottom (or top) of the Ewald sphere.

Figures 4.8 and 4.9 show idealized Ewald spheres. In reality both the reciprocal rods and the surface of the Ewald sphere are thickened: the reciprocal rods are broadened by atomic steps, while the Ewald sphere is thickened by the energy spread and angular divergence of the electron beam. Thus, the reciprocal lattice rods and the Ewald sphere intersect not at points but in volumes with a finite extent. This modifies the diffraction pattern by broadening LEED spots and giving RHEED spots a streaky appearance. The streaking

of the RHEED pattern is particularly pronounced where the reciprocal lattice rods cross the Ewald sphere at oblique angles.

4.3 Low Energy Electron Microscopy

Low energy electron microscopy (LEEM) is a non-destructive surface science technique invented by E. Bauer in 1962.[129] It is used to probe chemical, electronic, magnetic, and structural properties of surfaces, and can achieve resolution less than 10 nm. The technique allows for real-time data acquisition in movie form and is thus well-suited to interrogation of kinetic processes. Moreover, it has tremendous power for probing the real-space crystalline structure of ordered surfaces.

Fig. 4.10 is a simplified schematic (not drawn to scale). As the figure shows, the LEEM chamber is shaped like a "Y" (or in some cases a "T"). An electron beam (green dashed line in the figure), produced by the electron gun in the upper right-hand corner of the figure, passes through a set of condenser lenses (purple) that collimate it and accelerate it to high energy, typically 10–20 keV. High electron energy is important for high spatial resolution, and also minimizes the effects of stray electromagnetic fields that might otherwise defocus the beam.[130] The beam passes through a magnetic field at the center of the "Y" and is bent into a path orthogonal to the sample plane. An illumination aperture (not shown in the figure) is interposed, often inside the magnetic field itself, to improve collimation of the beam before it passes through an objective lens (blue, solid boundary) and interacts with the sample (bottom of

the figure). The objective lens is grounded, but the sample is floated at a negative potential very close to that of the impinging electron beam, so that the beam is abruptly slowed before it interacts with the sample: usually the beam energy at the sample is less than 100 eV. The sample and objective lens sit only a few mm apart, so the electrostatic field between objective lens and sample is on the order of 10 kV/mm. The beam is focused not only by the objective lens, but also by this field gradient, and so the sample constitutes an active optical component of the system. On account of the high field gradients (in addition to the requirement that surface contamination be minimized) LEEM is operated only under UHV conditions. Because the electron beam is very slow when it interacts with the sample, its penetration depth is only a few atomic layers, and so the technique is characterized by high surface sensitivity.

At the sample surface, the beam is reflected, scattered, and diffracted. The strong electrostatic field that slows the incoming beam accelerates the outgoing beam to high energy as it moves away from the sample. The beam re-enters the magnetic field: now that the electrons are moving in the direction opposite to that of their first pass, the beam is deflected away from the illumination column and into the imaging column. At the back focal plane of the objective a diffraction pattern (Fourier transform) is created. The diffraction pattern is the LEED image of the sample; see Section 4.2.1, above, for discussion of LEED. A diffraction pattern for the clean Si(111) surface exhibiting a 7x7 surface reconstruction is shown in the figure. A contrast aperture is inserted into the diffraction plane and can be mechanically adjusted to select

a part of the beam that has undergone a particular angle of diffraction or reflection. Transfer lenses (indicated in the figure with dash-dotted borders) are inserted as needed to shift the location of the diffraction plane to a position in the beamline that allows for the insertion of the contrast aperture. Whichever part of the beam has been selected by the contrast aperture then passes through the field lens and intermediate lens (pink in Fig. 4.10), which are coupled. These together are switched into one of two modes, in order either to (a) form a direct-space image of the sample surface (*i.e.,* an inverse Fourier transform) at the image (Gaussian) focal plane, behind the contrast aperture; or (b) allow the LEED pattern to be imaged at that plane. Finally, the projective lenses (pink in Fig. 4.10) magnify the diffraction or real-space image and project it onto a microchannel plate (MCP) connected to a video acquisition system. A direct-space image of a Si(111) 7x7 surface at about 600°C is shown next to the MCP in the figure. A more detailed explanation of the functions of the various parts of the system is contained in reference [131].

Fig. 4.11 shows all the lenses fully labeled. As this figure shows, the geometry of LEEM can allow for an evaporative deposition source, such as a K-cell or electron beam evaporator, to be installed at an oblique angle to the sample. This permits studies in which growth is observed in real time.

The ability to use various diffracted parts of the beam to create real-space images is a key feature of LEEM. If the directly reflected LEED spot is used for imaging, the imaging mode is referred to as "bright field," and the resultant video image approximately resembles a scanning electron microscope

(SEM) image. (The physical interpretation of the image, however, is quite different from SEM, since SEM operates at beam energies on the order of keV, whereas LEEM electron energies are typically on the order of a few eV by the time they interact with the sample. Moreover, LEEM images are obtained by a "true imaging" process, as opposed to the rastering process used in SEM; LEEM data are therefore acquired in real time.) On the other hand, if a higher-order diffraction spot is selected for imaging, the resulting image will show illumination only in those regions of the sample surface that produced diffraction at the chosen angle. This is "dark-field imaging mode."

An example of dark-field mode, taken from our work, is shown in Fig. 4.12. The sample is a Si(100) substrate that has been flashed to remove the native oxide layer. The right-hand panel of Fig. 4.12 shows the diffraction pattern for for the same surface. It consists of two superposed diffraction patterns from the Si(100) 1x2/2x1 reconstructed surface, each rotated at 90° relative to the other. The rotated domains are known to correspond to 90° rotations in the direction of dimer rows on alternating crystal steps. The left-hand panel is the real-space image acquired by imaging from one of the first-order diffraction spots: for example, possibly the one circled in yellow in the right panel of the same figure. Bright regions are steps from which diffraction produced the selected LEED spot. Dark regions correspond to steps where dimer rows are oriented at 90° relative to those on the bright steps.

The LEEM technique does not generally yield topographic data that are easy to interpret, and in cases where topographic data are the primary

goal, SPM methods are usually superior. However, atomic steps are often clearly visible in LEEM data. This is because the electron beam—which can be treated as a plane wave field at the sample surface—interferes with itself when it is reflected from the top and bottom edges of a single atomic step.[132]

In a similar manner, quantum size effects are observed when electron waves reflected at a thin film/vacuum interface interfere with those reflected from a film/substrate interface.[133] Obviously, this requires that electron penetration depth into the sample be at least as long as the electron wavelength. Therefore, whether or not this effect is seen depends on both film thickness and beam energy.

The LEEM studies described here were performed on a commercial Elmitec III LEEM system. The sample stage can be cooled to approximately 115 K. Ag deposition was carried out, at different times, by both electron-beam evaporation and K-cell. Deposition and sample interrogation can take place simultaneously. Chamber pressures were typically in the 10^{-10}–10^{-9} Torr range during growth (although occasionally as high as 10^{-8} Torr). When growth was not taking place, chamber pressures were generally in the 10^{-11}–10^{-10} Torr range.

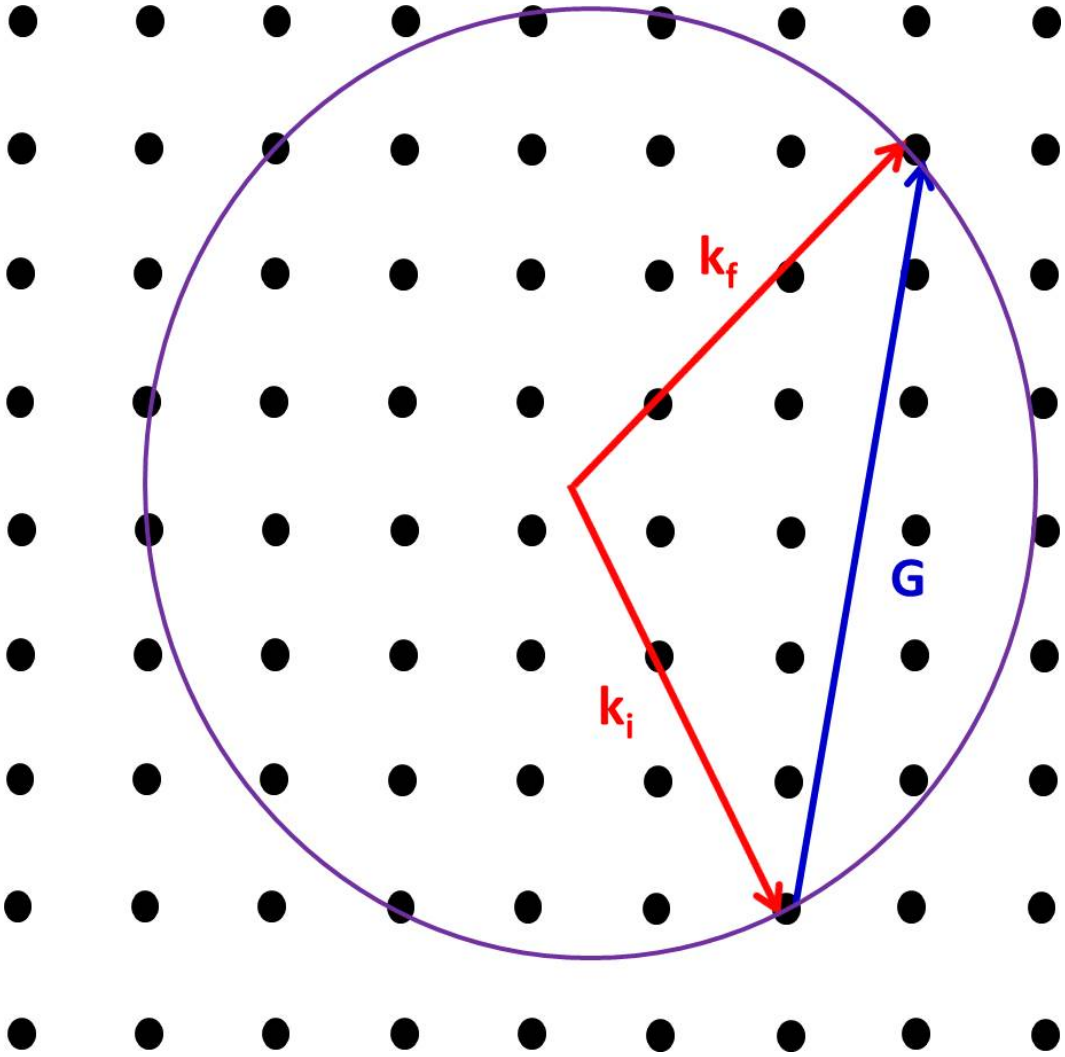

Figure 4.8: Illustration of Laue condition.

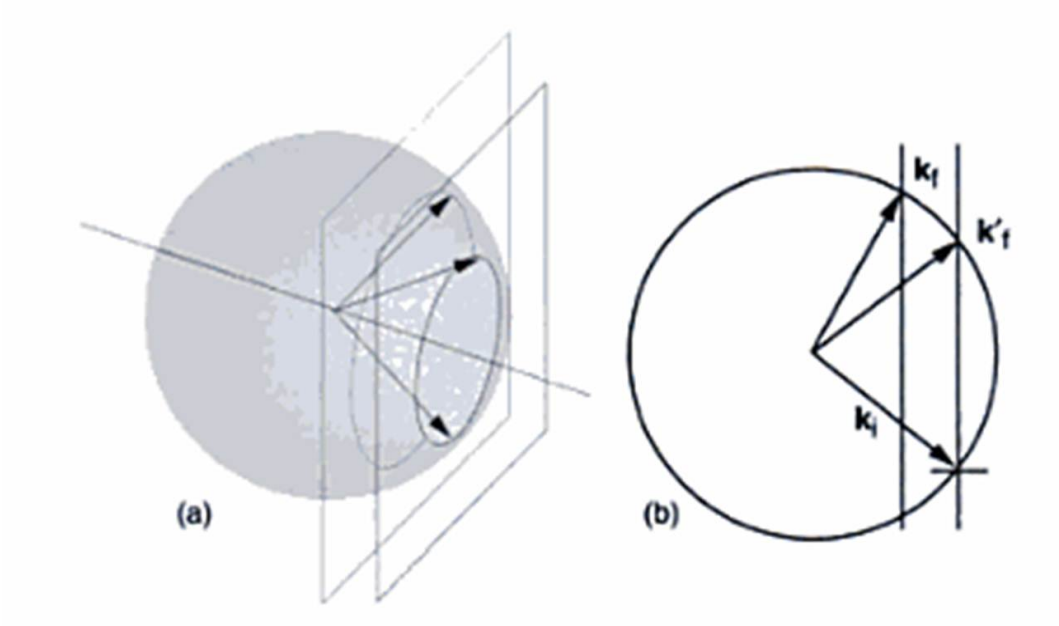

Figure 4.9: Ewald sphere in 3D, for diffraction from a 1D lattice. From [125], copyright 2004. Original caption: Ewald construction for a 1D row of scatterers. (a) Perspective view of the construction showing Laue zones. (b) Side view of the construction. Reprinted with the permission of Cambridge University Press.

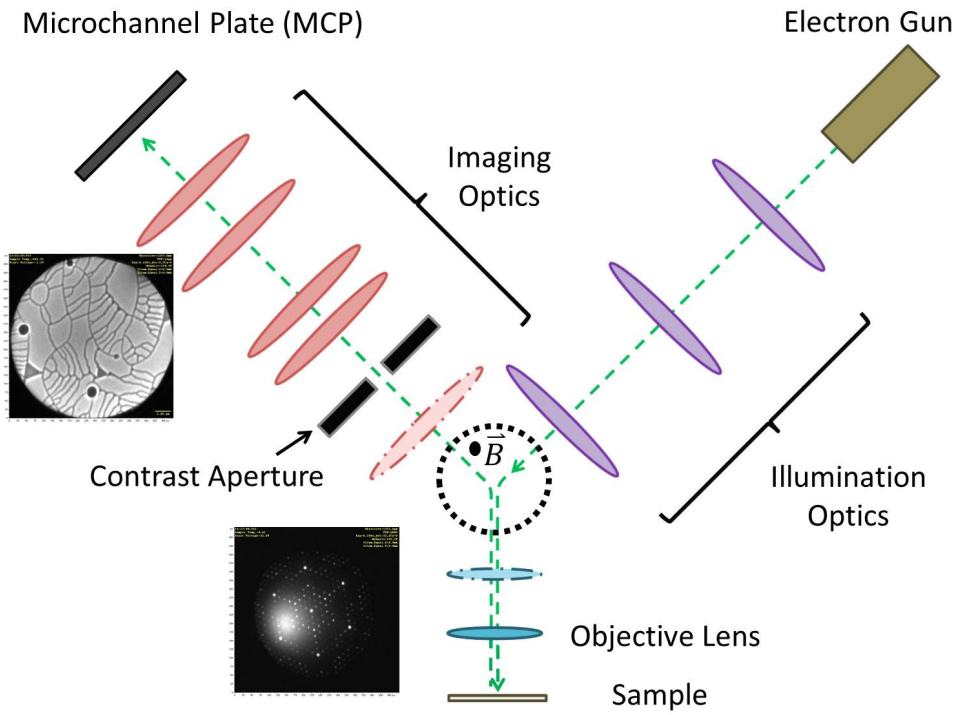

Figure 4.10: Schematic of LEEM. An example of a LEED image (clean Si(111) 7x7 surface) is inset at lower left, and a real-space image (same surface, approximately 600°) is in the upper left.

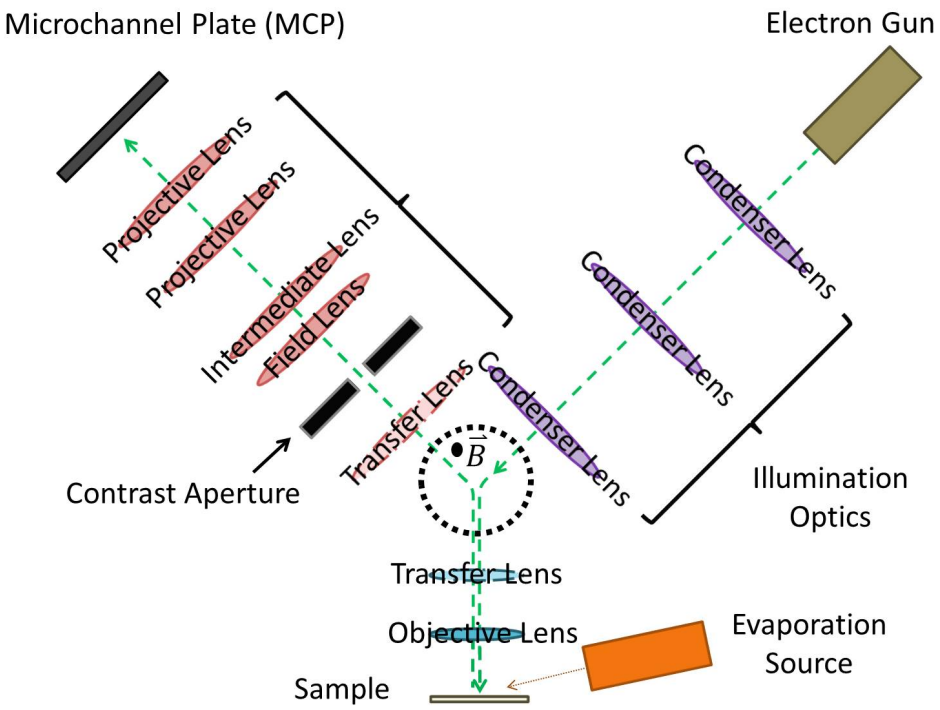

Figure 4.11: Schematic of LEEM, with components labeled. Position of optional deposition source is shown.

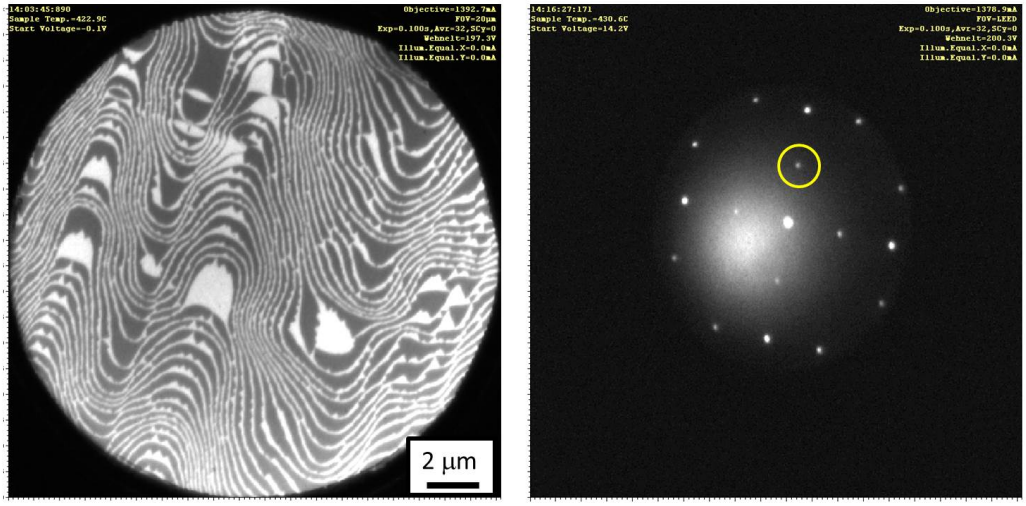

Figure 4.12: Left: dark-field image of clean Si(100) surface, 1x2/2x1 reconstruction. Right: LEED pattern for the sample shown on the left. The circle shows which order of diffraction was used to obtain the real space image.

Chapter 5

Studies of Ag Film Growth on Si

5.1 Construction of Home-Built System for Metal- Semiconductor Heteroepitaxy

For epitaxial growth of Ag films, I designed and built an MBE system dedicated exclusively to growth of metal-semiconductor heterostructures. Previous to the establishment of this system, we had grown metal films on semiconductor substrates using a set of compact home-built evaporators which were incorporated into each of our analysis chambers for small-scale growth studies. The dedicated MBE system makes film growth more efficient, particularly the growth of thick ($\sim$ 10s of nm) films. It has also allowed us to implement a system of capping with dielectric materials to stabilize films for out-of-vacuum use.

5.1.1 Preexisting Compact Evaporator Design

For systems operating under UHV, a set of simple, inexpensive, and extremely compact home-built evaporators allows us to incorporate basic epitaxial growth capabilities into a wide variety of analysis chambers. The design consists of a conical, hand-wound tungsten (W) filament basket into which Ag shot (99.999% purity from ESPI Metals) is loaded directly without the

use of a crucible. By flowing current through the filament, we evaporate the Ag. This simple effusion cell is shielded from the sample by a shutter into which a quartz crystal monitor (Maxtec, Inc. sensor crystal on Au, 6 MHz) is incorporated. The whole design can be mounted on a single 2.75" conflat flange. A schematic is shown in Fig. 5.1.

There are two major drawbacks to this approach to evaporation. First, the W filament basket is necessarily small, since the evaporator is compact by design, and since a basket containing a large volume of Ag would require impractically large currents for evaporation. Because of the basket's small capacity, frequent venting and replenishing of the Ag source is necessary; this results in major experimental delays, especially when thicker films are grown.

The second drawback is the incorporation of the crystal monitor directly into the shutter. Although this allows for a convenient, compact geometry, it means that the deposition rate can only be monitored when the shutter is closed, since only when the shutter is closed is the embedded crystal in a direct line of sight to the source. Since the temperature of the source cannot be directly monitored, there is no straightforward way to identify fluctuations in the evaporation rate during growth.

5.1.2 Dedicated MBE Chamber for Metal-Semiconductor Heteroepitaxy

In order to address these issues, I designed and built a dedicated MBE chamber for metal-semiconductor heteroepitaxy. I made the initial drawings

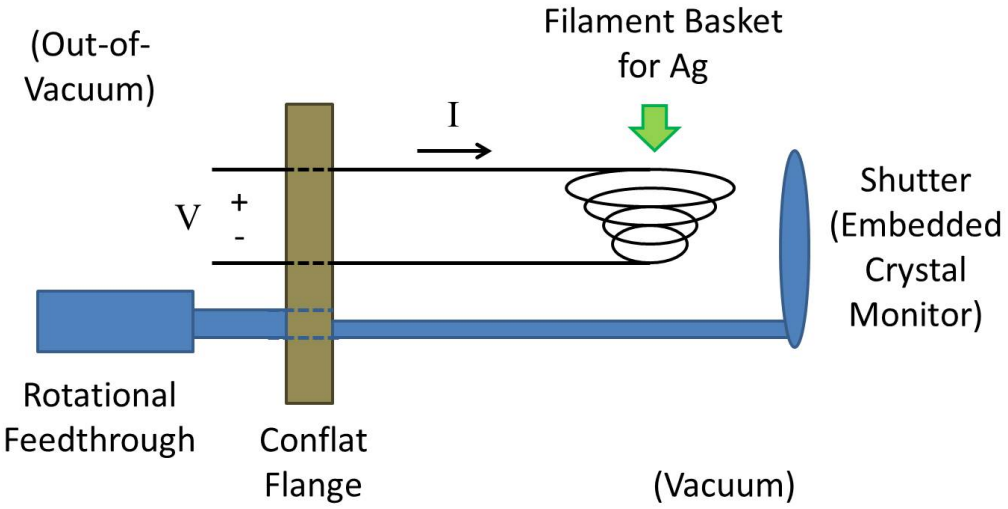

Figure 5.1: Schematic of compact evaporator. See text for details.

using SolidWorks with assistance from Dr. Jisun Kim. The machining and welding was performed in the University of Texas Physics Department machine shop. The chamber—which operates in the pressure range from high 10^{-11} to low 10^{-10} Torr—is built around a four-port, water-cooled MBE flange based on designs by former lab member Professor Arthur Smith (currently at Ohio University) and by SVT Associates, Inc. Each of the flange's four ports allows for either an effusion cell or an electron-beam evaporator to be mounted on a 2.75" CF flange, and each is shielded by its own shutter. We use commercial Knudssen effusion cells ("K-cells") purchased from SVT Associates, with pyrolytic boron nitride (PBN) crucibles. The effusion cells include a C-type thermocouple for temperature monitoring, and are controlled by Eurotherm 2408 programmable proportional-integral-derivative (PID) controllers that al-

low the temperature of the source material (and, thus, the evaporation rate) to be controlled to within approximately 1°C. Water at 4°C is continuously flowed through the interior of the growth flange and through jackets around each of the growth ports by a closed-cycle chilling system. A water-cooled quartz crystal monitor (Maxtec, Inc. sensor crystal on Au, 6 MHz) allows for deposition calibration. A commercial RHEED system by Staib Instruments allows for *in situ* growth monitoring and can also be used for growth calibration. RHEED data is collected and analyzed using kSA400 RHEED software by k-Space Associates, Inc. A commercial sample manipulator from Thermionics, Inc., features x, y, and z motion and a differentially pumped rotational platform so the sample can be rotated during RHEED analysis. The sample growth stage is home-built. It allows for direct heating, and also for sample cooling to temperatures below 100 K using a continuous flow of liquid N_2. The temperature of the sample stage is monitored by a K-type thermocouple.

Since the MBE chamber became fully functional in 2009, it has been incorporated into a larger cluster of home-built systems that provide additional analysis capabilities. An LT-STM system (liquid N_2 or liquid He operating temperature, Nanonis control system) built by Huan Li and a LEED analysis chamber are connected to the MBE chamber by a UHV transfer line designed and built by Dr. Jisun Kim and Dr. Chendong Zhang, so samples can be transferred among the three chambers without breaking vacuum. A schematic is in Fig. 5.2.

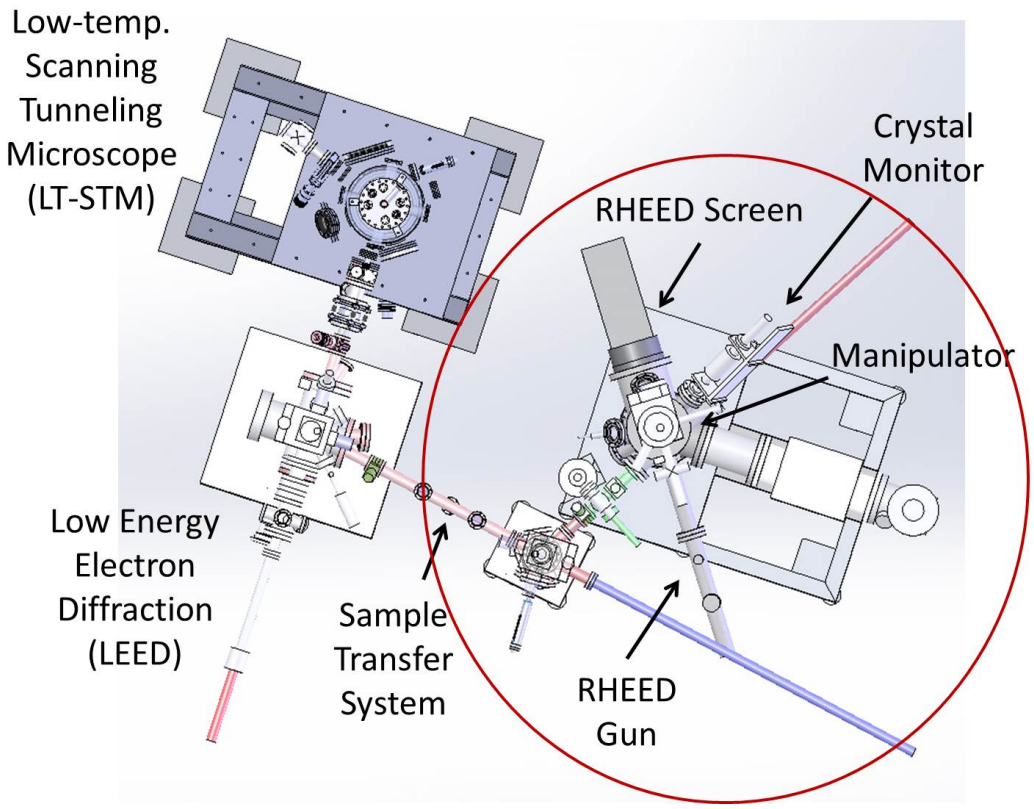

Figure 5.2: Schematic of MBE chamber coupled with STM and LEED analysis chambers.

5.2 Sample Preparation

Silicon substrates are prepared by flashing with direct current heating to between 1100° and 1300°C in UHV. This flashing removes the native oxide layer from the Si surface, and also reconstructs the surface—to a 7x7 reconstruction, in the case of Si(111), or 1x2/1x2, in the case of Si(100). The use of fast direct-current heating allows for localized heating of the sample with minimal heating of the sample holder and stage; thus, the chamber pressure

can remain in the 10^{-10} Torr regime throughout the flashing process. After flashing we confirm the surface reconstruction using STM, LEED, or RHEED.

Before growth, the sample is cooled on the sample holder to below 100 K. At low temperature, the Si(111) 7x7 surface reconstruction persists, but the Si(100) 1x2/2x1 surface structure is modified and becomes c(4x2). Ag is deposited at an approximate rate of 1 $\AA$/min. The oriented nanocluster structure of the as-deposited Ag is observable by RHEED (Fig. 5.3). No more than 2–4 nm of Ag are deposited: inferior film quality results from thicker deposition. When deposition ends, the sample is annealed at room temperature for from one to a few hours. The time of annealing is not critical. If thicker film is needed, the sample is again cooled, and the procedure is repeated as many times as is necessary. With careful control of growth parameters, the film can remain atomically flat for many growth cycles: see Fig. 5.4.

5.3 Additional Data and Analysis

Fig. 5.5 shows LEED and direct imaging data for Si(100) substrate preparation and Ag deposition. Panel (a) shows the LEED pattern from clean Si(100) surface immediately after flashing. The pattern indicates two surface reconstructions, 1x2 and 2x1, rotated at 90° relative to each other (circled with different colors in the inset). This is due to the well-known rotating of dimer rows on adjacent steps that was described in Chapter 4. The LEEM dark-field image in Fig. 5.4(b) shows the corresponding real-space image of the sample surface; here the alternating rotated surface lattices are clearly evident

as dark and light steps. Fig. 5.4(c) shows the LEED image that emerges during deposition of 10 ML at 115 K (before annealing): the pattern is quite sharp, showing two co-existing Ag(111) 1x1 surface structures (circled with different colors in the inset). Imaging in dark-field mode from either of the two reciprocal lattices, as in panel (d), reveals that the crystalline orientation of the Ag is rotated through 90° on adjacent steps, maintaining a definite relationship to the underlying Si(100) dimer rows on each terrace. Because the sample has not yet been annealed, the Ag morphology consists of clusters; nevertheless, the clusters show a particular crystalline orientation with respect to the substrate. This finding agrees with the RHEED data for Ag on Si(111) in Fig. 5.3: the Ag(111) 1x1 pattern is already established before annealing, with the only difference between the top and bottom panels being the clustered versus flat film morphologies.

It is of interest that epitaxial Ag(111) preferentially adopts the (111) orientation on a wide variety of semiconducting and insulating substrates. It is likely that this is due to Ag(111) having lower surface energy than other orientations; the likelihood that surface energy is an important contribution to the total free energy of these systems is supported by the tendency of the system to form round clusters (with low surface-to-volume ratio) during deposition (see Figs. 1.1 and 1.2 in Chapter 1). L. Vitos *et al.* calculate surface energies of 1.172, 1.200, and 1.238 J/m^2 for Ag(111), (100), and (110), respectively.[135]

It is also of interest that the Ag(111) clusters and film adopt a par-

ticular rotational orientation with respect to the underlying Si surface. The (111) surface of the Ag film has a hexagonal close-packed (HCP) structure. The Si(111) 7x7 surface, too, is characterized by a hexagonal symmetry, as is the c(4x2) surface structure assumed by Si(100) at low temperature. As explained in Chapter 1, the Ag film and underlying semiconducting substrate are believed not to bond chemically: the film is stabilized by a combination of surface energy minimization, QSEs, and charge spilling, with only weak interaction between the film and substrate. It is therefore not clear what role, if any, is played by lattice matching in this system. As discussed in Chapter 2, the degree of strain in Ag film grown on Si and GaAs remains open to question, as does its effects on morphology and electronic structure. (The lattice mismatch between the surface lattice of the substrate and the Ag bulk lattice in the (111) direction is 3.3% for Si(111) 7x7 and 24% for Si(100) 1x2.) However, the clear preference for a particular rotational orientation on Si suggests that some definite interaction does exist. In the case of Ag(111)/Si(111), controlled heating to around 110° initiates dewetting and recovers the Si(111) 7x7 pattern (presumably, through pits extending down to the substrate: the overlayer LEED pattern continues to dominate the image), indicating that the surface reconstruction survives under the overlayer after growth and annealing: see Fig. 5.6. It is therefore not unreasonable to consider that the hexagonal symmetry between the substrate surface reconstruction and the overlayer might play a role in determining the crystalline orientation of the overlayer. On the other hand, the low-temperature c(4x2) phase of Si(100) is typically seen at low tempera-

ture only, leaving as an open question the details of Ag(111)/Si(100) interface after annealing to room temperature. These intriguing questions merit further study.

5.4 Ge Capping for Film Stabilization

Our fundamental understanding of the processes underlying dewetting of Ag film out of vacuum remains limited, as discussed in Chapters 2 and 6, but interaction with air greatly accelerates film degradation. Therefore, we have been motivated to use a uniform capping layer to isolate Ag film from interaction with atmospheric species. I and Dr. Jisun Kim developed a method, which we currently use, for capping flat Ag film with a layer of amorphous Ge. After growing and annealing Ag film, we verify film quality using STM or electron diffraction. We then recool the Ag film to liquid N2 temperature. Using a K-cell with PBN crucible as our Ge evaporation souce, we deposit 1–2 nm on our Ag sample at a rate of 0.5 $\mathring{A}$/min. During deposition the RHEED pattern disappears, consistent with the interpretation that the Ge overlayer is amorphous. Subsequent scanning with AFM reveals that the overlayer is smooth, with only sub-nm roughness on individual terraces: see Fig. 5.7.

More information is in Chapter 6.

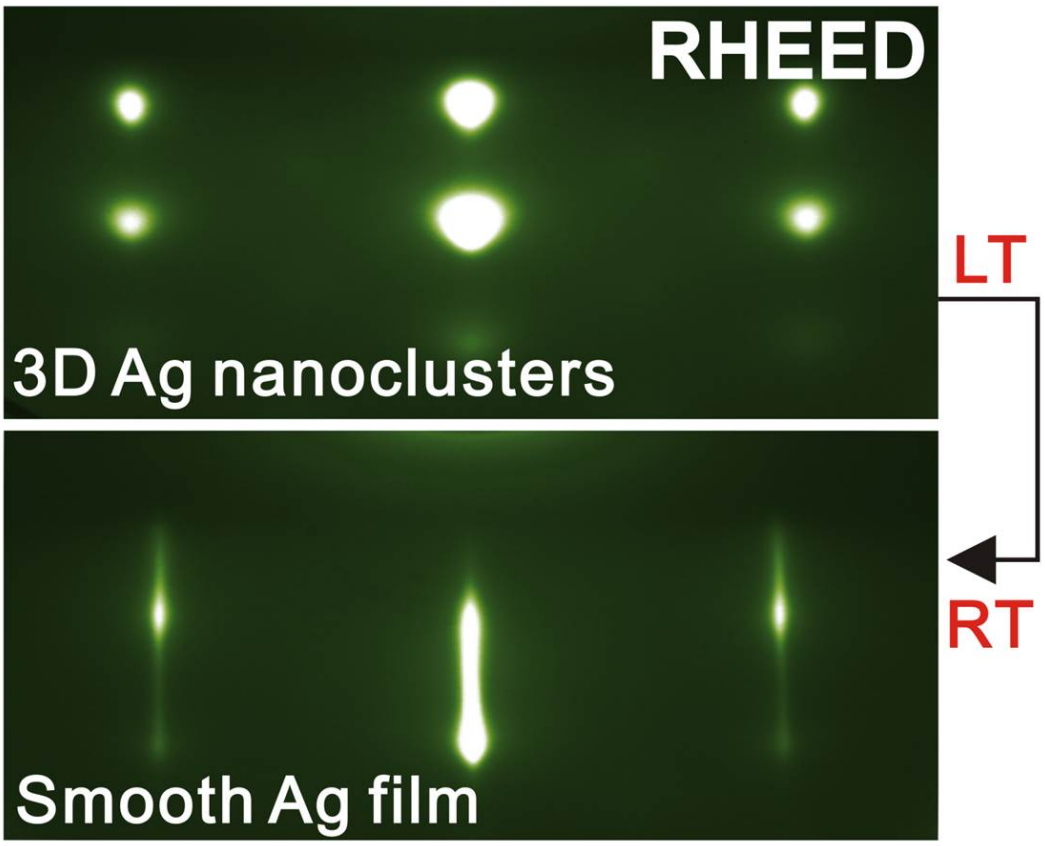

Figure 5.3: From [134]. Top panel: RHEED data acquired before annealing of Ag on Si(111). The large spots indicate nanocluster morphology. Bottom panel: RHEED data acquired after annealing. The streaks indicate flat film, and their geometry is consistent with the Ag(111) 1x1 crystalline surface structure. The spots in the top panel follow the lines of the streaks for the Ag(111) 1x1 pattern, indicating that the 3D clusters are crystalline, and that they are rotated in the same direction as the Ag film in the bottom panel. Reprinted with permission from AAAS.

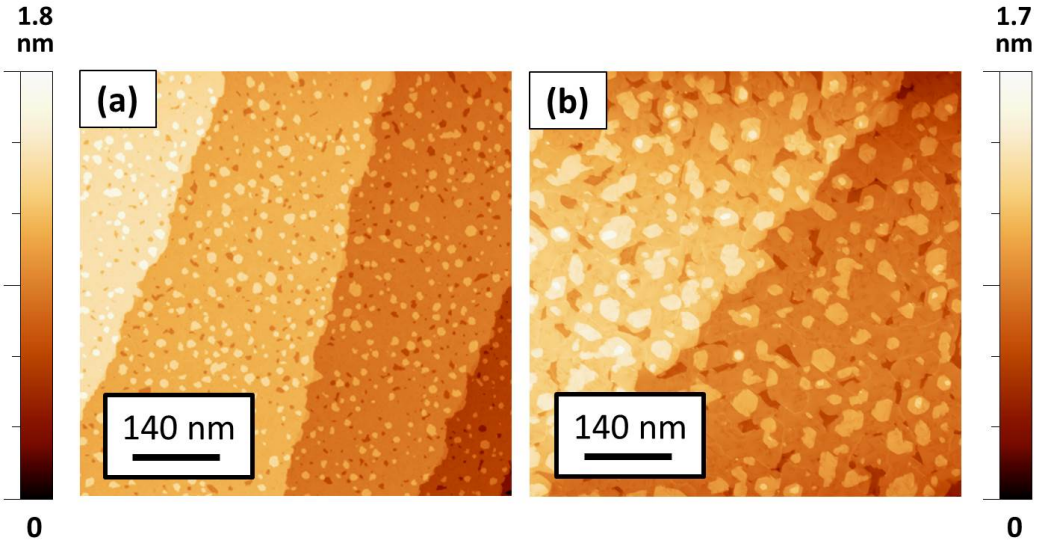

Figure 5.4: STM topography of epitaxially grown Ag film on Si(111). Data acquired by Dr. Jisun Kim. Left panel: morphology after one growth cycle. Total thickness is 10 ML. Right panel: Morphology after three growth cycles. Total thickness is 30 ML. After multiple growth cycles the film remains smooth, with predominantly only 1 ML surface roughness. Scanning temperature: 78 K.

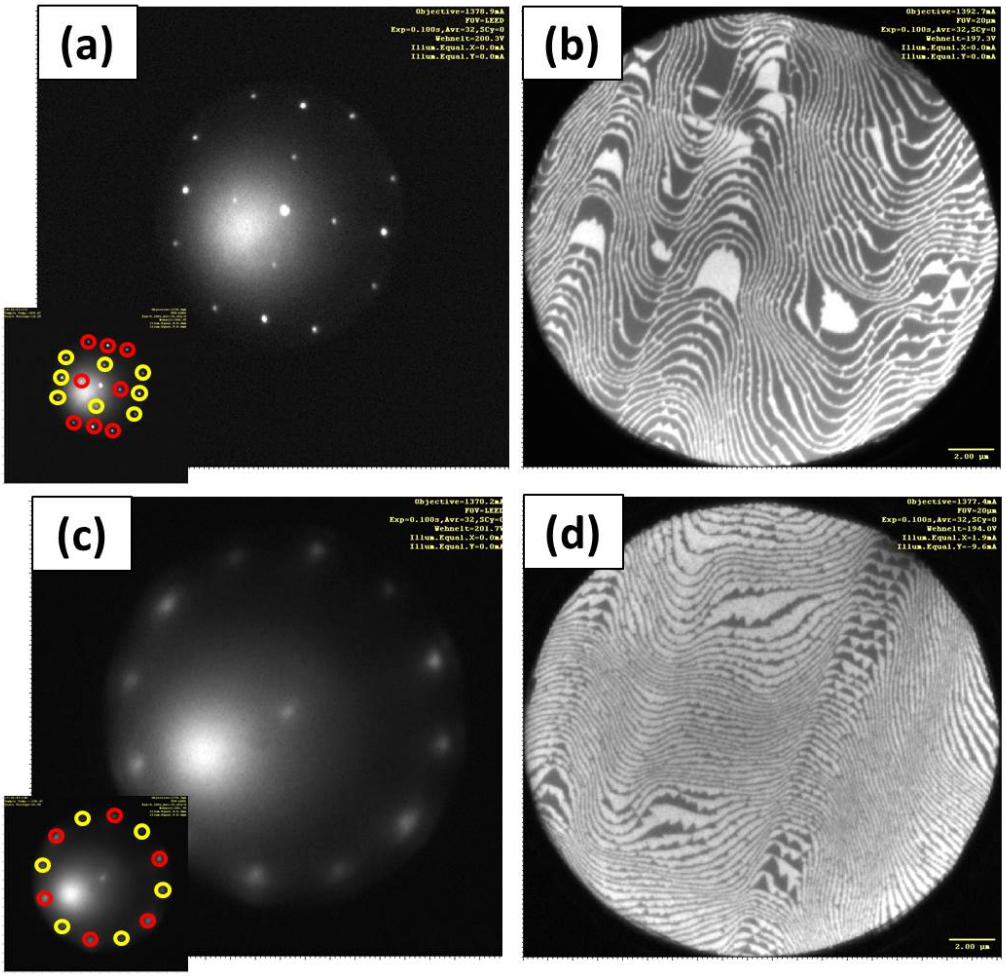

Figure 5.5: Preparation of Si(100) substrate and deposition of Ag (carried out at Sandia LEEM facility). (a) LEED of clean Si(100) surface after flashing. 2x1 and 1x2 patterns are indicated in the inset with red and yellow circles, respectively. (b) Dark-field image of the clean Si(100) sample from (a). Alternating bright and dark steps correspond to alternating dimer row directions on adjacent steps. (c) LEED acquired during deposition at 115 K. The Ag clusters already exhibit a preferred crystallinity and orientation with respect to the substrate. LEED shows two coexisting Ag(111) 1x1 domains rotated at 90° with respect to each other: in the inset, red and yellow distinguish the two domains. (d) Dark-field image acquired from (c), confirming that the two Ag rotational domains correspond to adjacent substrate steps.

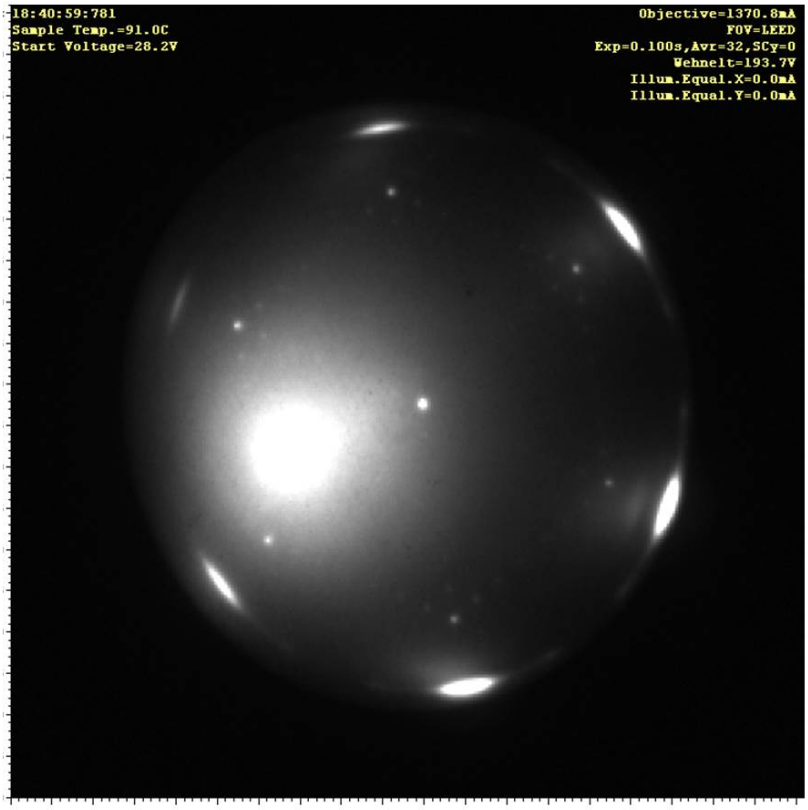

Figure 5.6: LEED pattern acquired after heating Ag(111)/Si(111) to initiate dewetting. The Ag(111) 1x1 pattern remains dominant, but the Si(111) 7x7 pattern begins to reappear.

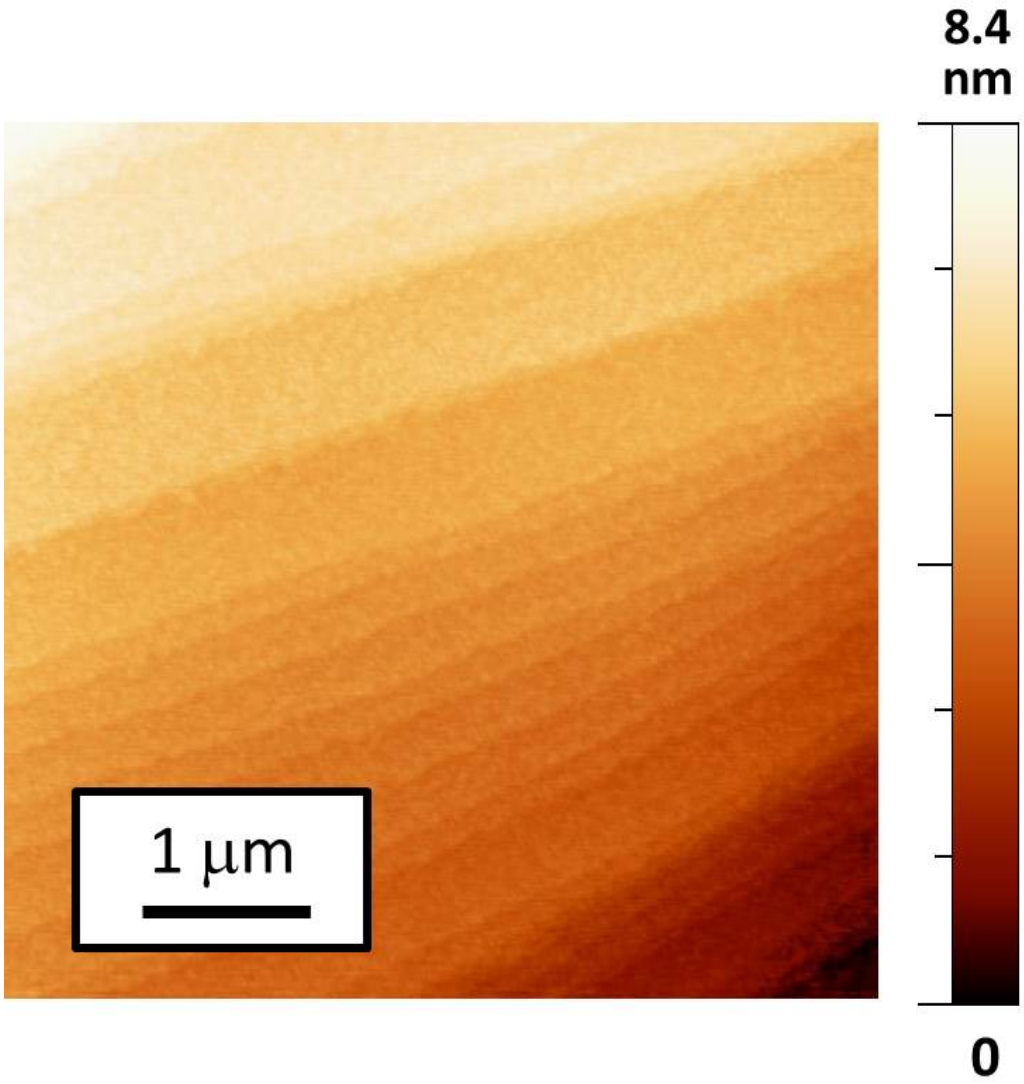

Figure 5.7: AFM image of Ge-capped 20 ML Ag(111) film on Si(111). Capping thickness is 2 nm. Data was obtained in ambient conditions after 29 days' exposure to ambient conditions. Roughness on individual terraces is sub-nm. See Chapter 6 for discussion of the efficacy of Ge capping to arrest dewetting processes.

Chapter 6

Investigation of Dewetting Mechanisms in Ag Films on Si

As discussed in Chapter 2, the dewetting of epitaxial Ag film on Si has yet to receive significant attention in the literature. Fundamental issues, including whether or not the film is strained and what might be the nature of the interface with the substrate, remain open to doubt. Ultimately, it is important to understand the physical and chemical processes that drive dewetting in this system. At the present time, though, the morphological changes that take place during dewetting have not even been identified. I have undertaken scanning probe and LEEM studies to characterize the evolution of film morphology for various film thicknesses held under vacuum at room temperature and at elevated temperatures. I have also investigated the morphological changes that occur when film is exposed to ambient conditions (*i.e.,* out of vacuum, room temperature) and have evaluated the efficacy of using thin dielectric capping (with Ge) to arrest dewetting under those same conditions.

6.1 Evolution of Ag(111)/Si(111) in Ambient Conditions

For this study, I prepared epitaxial Ag films on Si(111) and exposed them to ambient conditions. I monitored the evolution of the film morphology using AFM (tapping mode, ambient conditions—see Chapter 4 for details). That this AFM is capable of resolving the Ag film's initial ±1-ML roughness, and that the ±1-ML morphology survives at least briefly after the film is removed from vacuum, is demonstrated by Fig. 6.1. Here, a 20-ML film was scanned by Dr. Jisun Kim within a few hours after it was removed from vacuum. The substrate steps and the 1-ML-high islands on the terraces are clearly visible.

I prepared 10- and 20-ML films. The first sign of film degradation in each was the appearance, within about one day out of vacuum, of pinholes surrounded by raised rings. Fig. 6.2 shows these pinholes on (top) 10-ML-thick film and (bottom) 20-ML-thick film. A detail of one of the pinholes is included for the 20-ML film. The pinholes have roughly uniform diameters of about 100 nm. As can be seen in the detail, even after the formation of the pinholes, the area on the terraces remains extremely smooth, with 1-ML-high islands still the only visible features aside from the pinhole. The pinholes form preferentially but not exclusively at step edges: in the scan of the 20-ML-thick film both of the two pinholes are at step edges, while in the scan of the 10-ML-thick film 28 of the 36 pinholes (78%) are at step edges. The density of pinholes is much higher on the 10-ML film than on the 20-ML film, but

it is not possible to say whether this is because the 10-ML film is degrading more quickly or whether it is because the substrate of the 10-ML film is much more highly stepped than the other substrate. (The substrates have identical specifications and are from the same batch, but the 10-ML sample was flashed under strain due to details of the sample holder geometry. Flashing under strain can create highly stepped surfaces like the one seen here.)

After the formation of pinholes on the first day out of vacuum, no additional pinholes form. Thus, it seems likely that these may be a strain relief mechanism of some sort, rather than—for example—a chemical phenomenon, which would be expected to continue occurring with prolonged exposure. The pinholes do, however, evolve within about a day of their appearance: a roughened structure develops in the center. This can be seen in Fig. 6.3 in the third day out of vacuum. From this point, the 10-ML film exhibited a progressive, spreading roughening as shown in Fig. 6.3. The 20-ML film, too, degraded progressively, but with the formation of an irregularly pitted morphology, as seen in 6.4. The morphological evolution was not uniform, but proceeded at different rates on different regions of the samples, as can be seen in the two right panels of Fig. 6.4. Also, the 20-ML film evolved somewhat more slowly than the 10-ML film: features with heights on the order of tens of nm appeared within about 5 days and 8 days on the 10- and 20-ML films, respectively.

6.2 Room Temperature Evolution of Ag(111)/Si(111) under Vacuum

This study was conducted identically to the study under ambient conditions, except that the film in this case was stored in UHV conditions rather than air. Only 10-ML-thick film was investigated. The film was stored at room temperature and scanned with LT-STM. In sharp contrast with what was seen in air, the film in vacuum did not dewet at all over the time period of the study (9 days). On the contrary, the film smoothed. The upper left panel of Fig. 6.5 shows the original morphology after growth and annealing. The upper right panel shows the film morphology after 9 days in vacuum. There are fewer islands on the terraces, and the pits have ripened. The bottom panel shows the cross section taken along the arrow indicated in the upper right panel. The results agree with the model described in Section 2.3. Islands have evaporated, with adatoms migrating to ascending steps. On a slower time scale, pits are ripening; random walk motion eventually brings them to descending step edges where they cease to exist. Collective atomic motion toward the ascending step edge causes the topmost Ag layer to retreat from the decending step edge: see the bottom panel in Fig. 6.5.

The results of this study are in good agreement with those described in Section 2.1 for Ag film on GaAs(110), when thick film without pinholes was annealed in vacuum. There, too, annealing in vacuum led to film smoothening.

6.3 Dewetting at Elevated Temperatures: A LEEM Study

Dewetting in ambient conditions occurs on a relatively short time scale and is therefore easy to observe. However, it is difficult to isolate the thermal, kinetic, and possibly chemical processes that drive dewetting in this complex case. Investigation of the same system in UHV conditions simplifies the problem, particularly by minimizing the contribution of surface chemistry; but the evolution of the system at room temperature is so slow that it is difficult to study.

An alternative is to study the evolution of the system in UHV conditions at elevated temperatures, to speed the dewetting process and shed light on thermal processes that contribute to dewetting. Using LEEM, we are able to observe the evolution of the film in real time, and at the same time to acquire data on sample crystallinity. The Sandia CINT LEEM facility allows for heating the sample while simultaneously acquiring data.

6.3.1 Dewetting of Ag(111) on Si(111)

For this study we again examined 10- and 20-ML-thick Ag film on Si(111). In agreement with our findings for dewetting under ambient conditions, film thickness was seen to increase film stability. Moreover, 20-ML film was found to dewet through the nucleation of pits while 10-ML film exhibited a progressive generalized roughening, as seen in ambient conditions.

Fig. 6.6 shows the evolution of 10-ML film heated from room temperature to 110°C. Panel (a) shows the film immediately after growth and

annealing to room temperature. The visibility of the atomic steps (marked with black arrows in the figure) indicates that the film is smooth. When the film is heated to about 50°C, three domains emerge: one follows the step edges, one is dominant on the terraces, and one appears as speckles on the terraces. If the temperature continues to rise, these three domains exhibit a complex interplay. In particular, the boundary of the domain near the step edges fluctuates and moves on a time scale of minutes. The meaning of these three domains becomes clear if we sweep the sample voltage while measuring reflected intensity at each domain. This is the LEEM "I-V" technique: because reflected intensity is high when there are few states for electrons to tunnel into, an intensity peak corresponds to low density of states in the sample. In our case, clear oscillations are observed in the LEEM I-V spectrum at low energies. These are the QSEs described in Section 4.3. The three distinct quantum size oscillations seen here (panel (d)) suggest that the three domains are thickness domains. Although it is not possible without further investigation to unambiguously identify these three states with particular numbers of atomic layers, it seems reasonable that, here again (as seen in Section 6.2 above), we are seeing the collective motion of the topmost layer of Ag atoms toward the ascending step edge. In that case, the dark grey domain is either a +1 ML-Ag domain at the ascending step edge or a −1 ML-Ag domain at the descending step edge. The motion of the domain boundary would then be explainable as due to random atomic migration along the step edge, and the white speckles on the terrace as either 1-ML-deep pits (if the dark grey region

is +1 ML-Ag) or 1-ML high islands (if the dark grey region is −1 ML-Ag). As the temperature is further increased to over 100°C, generalized roughening takes place, with the emergence of multiple domains and holes that expose the Si substrate.

Much greater stability against dewetting is observed in the case of 20-ML-thick film: no morphological changes are evident at temperatures lower than approximately 160°C. At that temperature, random defects on the surface suddenly begin to nucleate localized dewetting. An example is shown in Fig. 6.7. The feature in Fig. 6.7(a) consists of three elements which are common to all the features produced by localized dewetting in this system: a core region from which dewetting begins (light grey with apparent structure in this image); a secondary region that grows outward from the initial core after the temperature surpasses 200°C (dark grey in this image); and a halo region that surrounds the entire defect. For this particular sample LEED reveals three coexisting crystalline domains: bare Si(111), Ag-Si(111) $\sqrt{3}x\sqrt{3}$ R30°, and Ag(111) 1x1. Fig. 6.8 shows dark-field LEEM data acquired from the same sample at another region. Imaging from the Si(111) diffracted beams gives panel (a): the bright regions here are the core regions from which dewetting was first observed to nucleate, so the core nucleation regions are evidently pits to the bare Si substrate. Imaging from the $\sqrt{3}x\sqrt{3}$ diffracted beams gives the image in panel (b): the part of the pits that formed when the temperature surpassed 200°C. We can infer, then that the halo-like structure surrounding each dewetting feature is Ag that piled on the terrace as the pit grew. This

interpretation is confirmed by AFM (panel (c), acquired under ambient conditions), which reveals not only the pit surrounded by piled Ag but also smooth and rough regions on the bottom of the pit that presumably corresponded to the locations of bare Si(111) and $\sqrt{3}x\sqrt{3}$, respectively, before the sample was removed from vacuum.

Interestingly, the partially dewetted film shown in Fig. 6.7 is still extremely smooth, aside from the pits. This can be seen in panel (b) of the same figure, where the LEEM focal plane has been shifted to image atomic steps. The morphology—smooth film punctured by discrete pits—is qualitatively similar to the morphology in the left and center panels of Fig. 6.4 for 20-ML film dewetting out of vacuum.

6.3.2 Dewetting of Ag(111) on Si(100)

Although Ag dewetting on Si(100) was not investigated as fully by us as was dewetting on Si(111), intriguing preliminary results have been obtained. Film was grown to 10-MLs' thickness and then heated in the same manner as that which was described in the previous section. Figure 6.9(b) shows sample morphology after heating to only 136°C: it has a "wormy" appearance. Figure 6.9(a) shows both the rotated Ag(111) 1x1 patterns and the Si(100) 1x2/2x1 pattern, indicating that dewetting has exposed the underlying substrate. Dark-field data from the Ag 1x1 diffracted beams is shown in Fig. 6.10. Surprisingly, there are four distinct domains. The dominant Ag 1x1 LEED pattern corresponds to the image on the left. It is easy to see that

this domain indeed covers more of the sample surface than does the other domain, which is imaged in the right panel. Why one of the two should be dominant is not clear. More strangely, each of these domains itself consists of two inequivalent domains. What distinguishes these two inequivalent domains is a topic that merits additional study. The diffracted beam corresponding to each domain is circled in the inset LEED image and color-coded to an arrow indicating that domain in the real-space image.

6.4 Efficacy of Ge Capping as a Means to Arrest Dewetting

The method of capping Ag films with amorphous Ge was discussed in Chapter 5. We have established that this technique is highly effective for stabilizing Ag film against dewetting. Figure 6.11 shows results. Panel (a) is AFM topography of an epitaxial Ag film capped with 2 nm Ge and stored in ambient conditions for 29 days. Panel (b) is AFM topography of an identical Ag film that was not capped (see Section 6.1 and Figure 6.4 for more details about this sample). The uncapped sample was only exposed to ambient conditions for 8 days, but consists of discontinuous irregular features tens of nm in height.

The success of Ge capping for stabilization of epitaxial Ag films will be further discussed in Chapter 7.

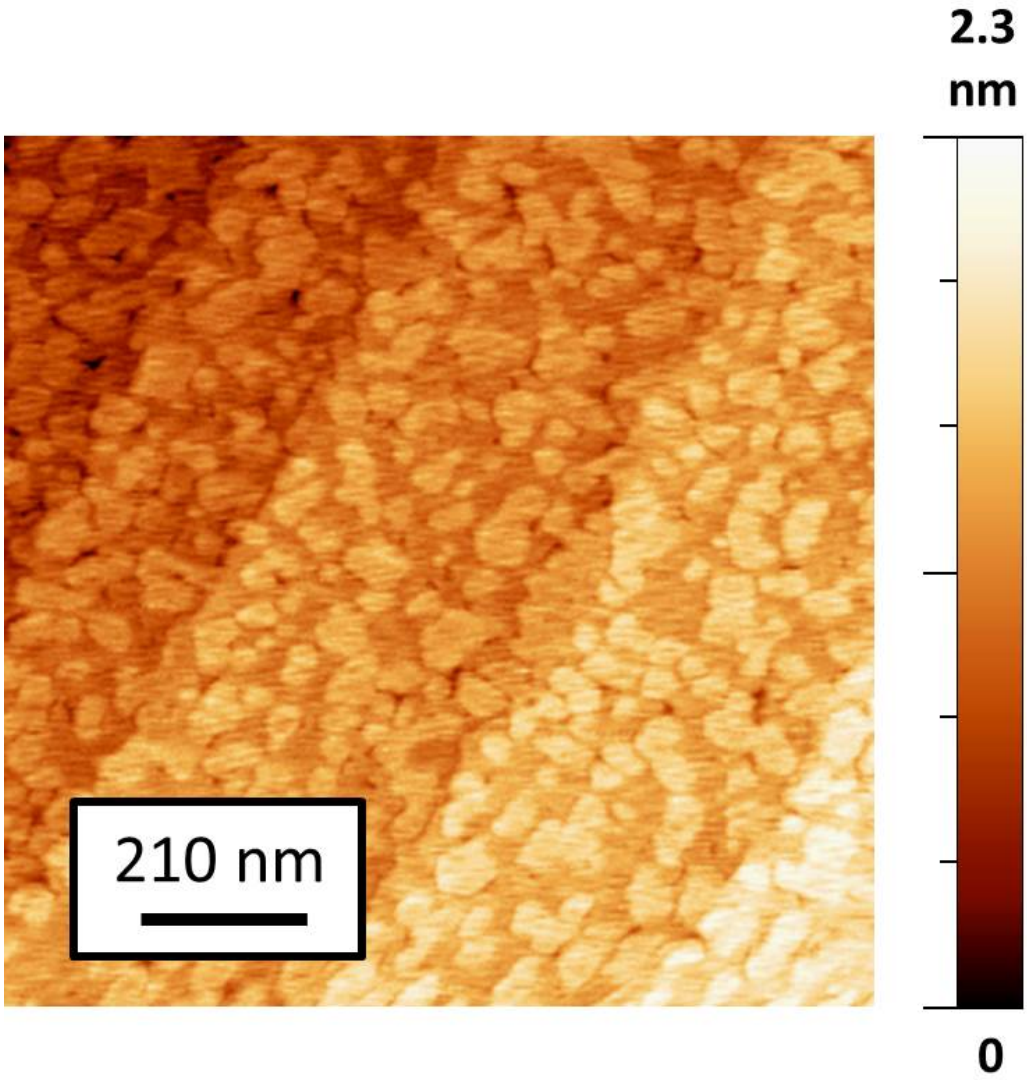

Figure 6.1: 20-ML-thick Ag film on Si(111), scanned with AFM in ambient conditions within a few hours of removal from vacuum. Underlying substrate steps and 1-ML islands on terraces are clearly visible. Data acquired by Dr. Jisun Kim.

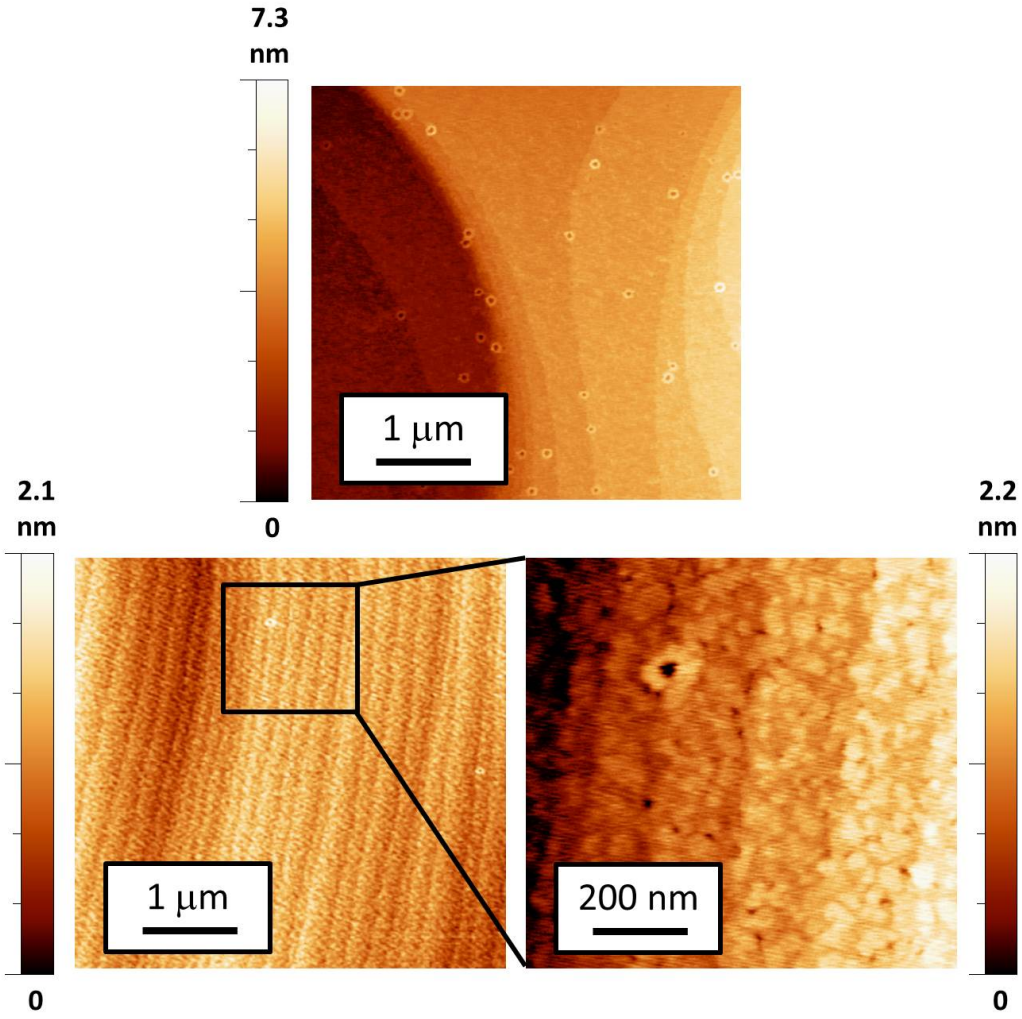

Figure 6.2: Within about 1 day out of vacuum, pinholes appear on the surface of thin epitaxial Ag film. Otherwise, the film on the terraces remains flat with ±1-ML roughness. (Top) 10-ML-thick film on Si(111). (Bottom left) 20-ML-thick film on Si(111). (Bottom right) Detail from scan at left, showing pinhole and terrace morphology. Area of detail is as indicated in left-hand panel.

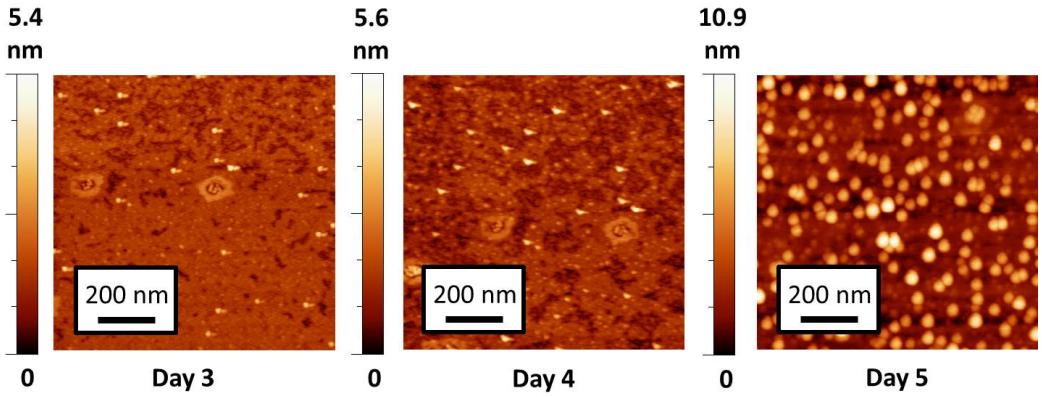

Figure 6.3: Continued evolution of 10-ML-thick film in ambient conditions. Although no new pinholes appear in the film, a generalized roughening takes place. After 5 days the film exhibits large irregular structures on the order of tens of nm in height.

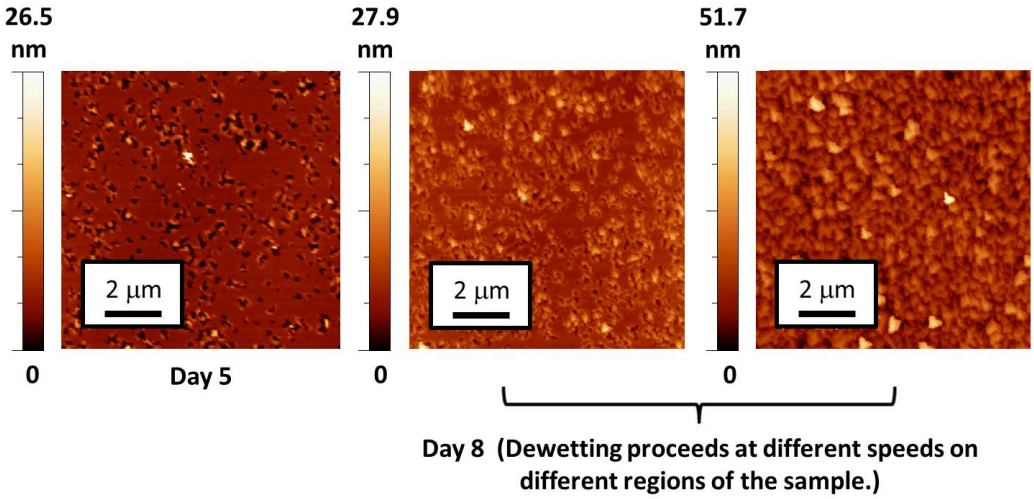

Figure 6.4: Continued evolution of 20-ML-thick film in ambient conditions. Although no new pinholes appear in the film, a generalized roughening takes place. After 8 days the film exhibits large irregular structures on the order of tens of nm in height. The middle and right panels show scans acquired on the same day and within only a few hours of one another, from different regions of the sample. Evidently, dewetting progresses at different rates across the sample surface.

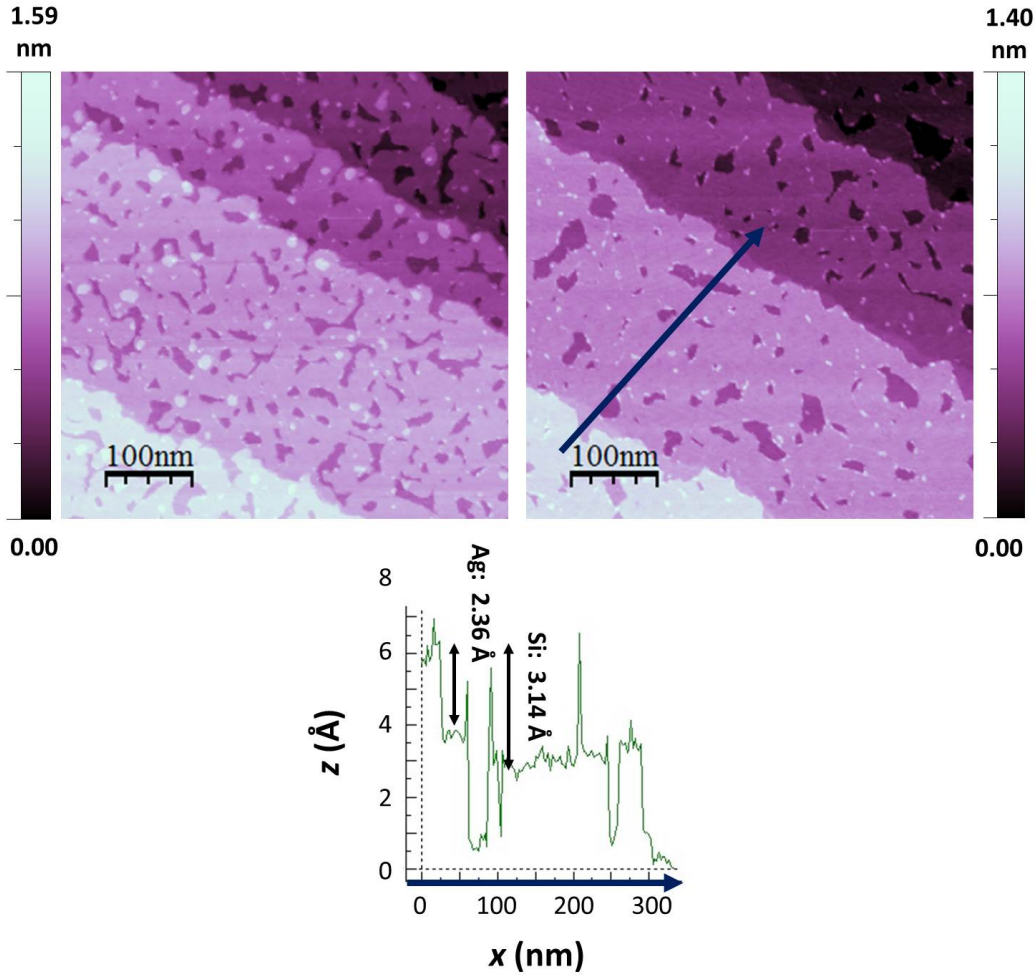

Figure 6.5: Morphological evolution of 10-ML epitaxial Ag film on Si(111) stored at room temperature in UHV for 9 days. Upper left panel: Initial film morphology after growth and annealing to room temperature. Upper right panel: morphology after 9 days at room temperature. Lower panel: cross section taken along arrow shown in upper right panel. Topmost layer of Ag atoms (2.36 $\mathring{A}$ atomic layer thickness) is retreating from the decending step edge defined by the underlying Si substrate (3.14 $\mathring{A}$ step height).

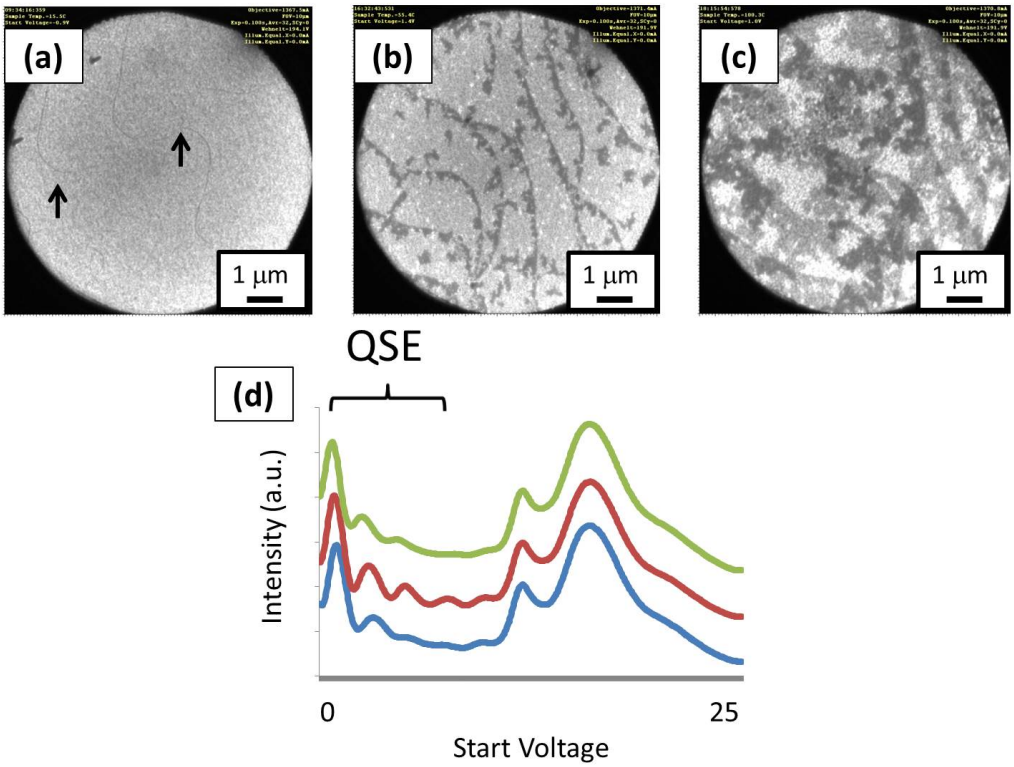

Figure 6.6: Dewetting of Ag on Si(111) at elevated temperature. (a) Room temperature. The film is smooth, as evidenced by the visibility of atomic steps (marked with black arrows). (b) Same film after heating to 70°C. Three domains are now visible: they appear dark grey, medium grey, and white at this beam energy. (c) Same film after heating to 110°C. Multiple domains now coexist. (d) The three domains in panel (b) exhibit distinct QSEs in the LEEM I-V curve, indicating that they correspond to three different thickness domains.

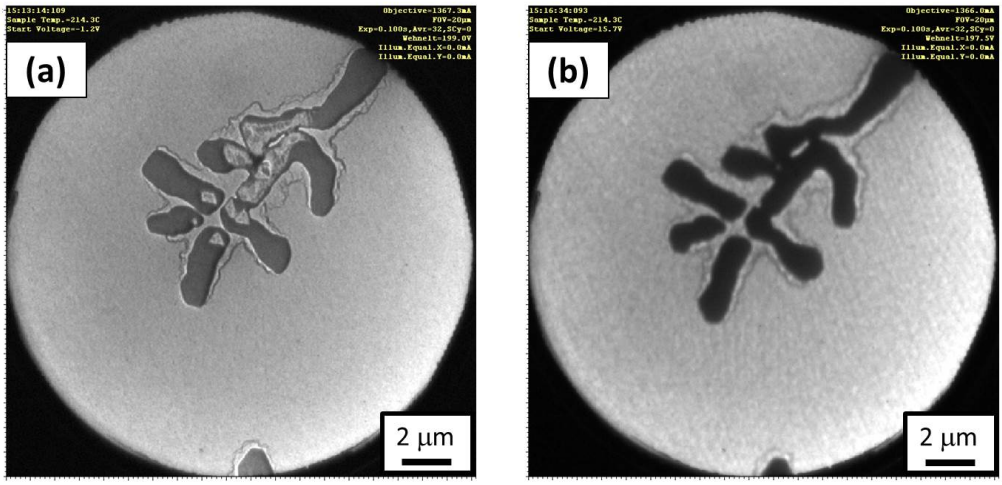

Figure 6.7: (a) In 20-ML-thick film, defects nucleate localized dewetting at around 160°C. The feature shown here developed as temperature was ramped from 160° to approximately 215°C. (b) Same feature as in (a). With the focal plane shifted (see Chapter 4), atomic steps become visible, indicating that most of the film's surface remains smooth despite localized dewetting.

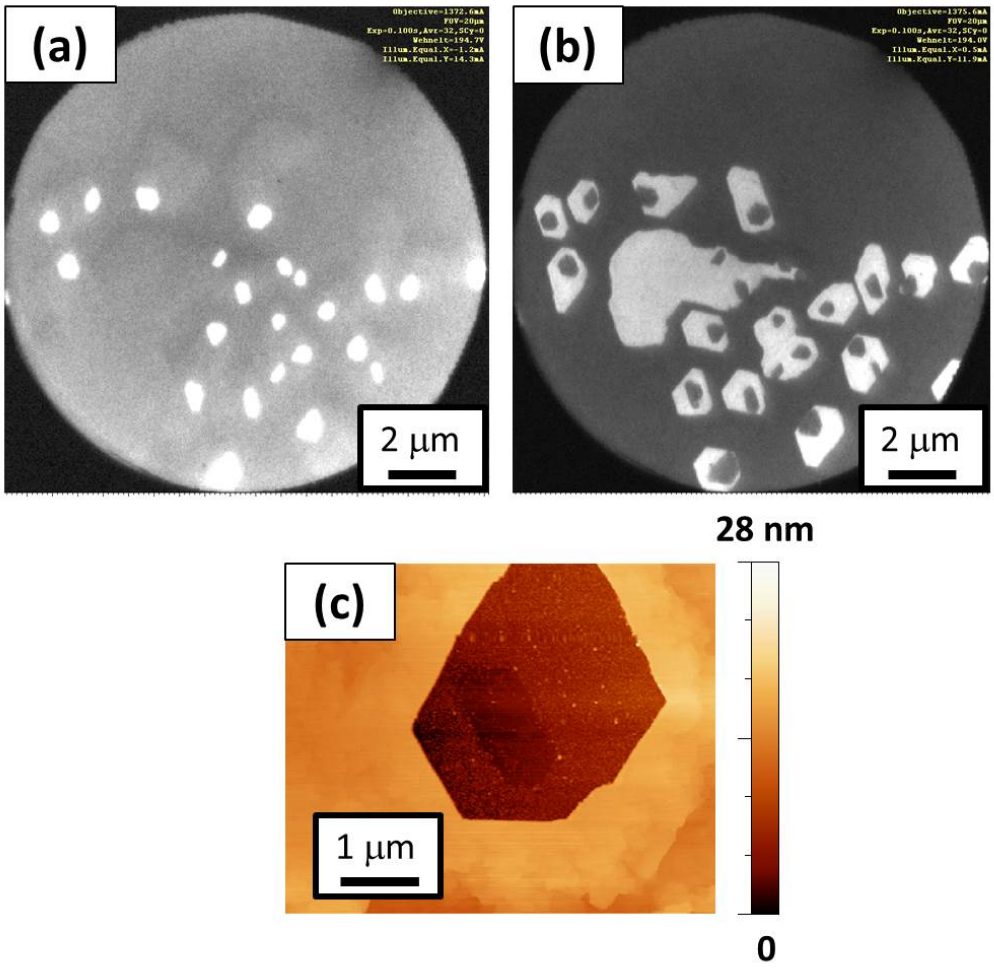

Figure 6.8: Dark-field LEEM data (top two panels) and AFM (bottom panel) reveal the structure of dewetted pit features. (a) Regions that appear bright in this image are bare Si(111), and are evidently the initial nucleation sites of dewetting. (b) Regions that appear bright are Ag-Si(111) $\sqrt{3}x\sqrt{3}$ R30°. These are the regions that emerge after the sample is heated above 200°C. (c) AFM confirms the morphology deduced from LEEM data (*i.e.*, that dewetted features are pits to Si surrounded by piled Ag).

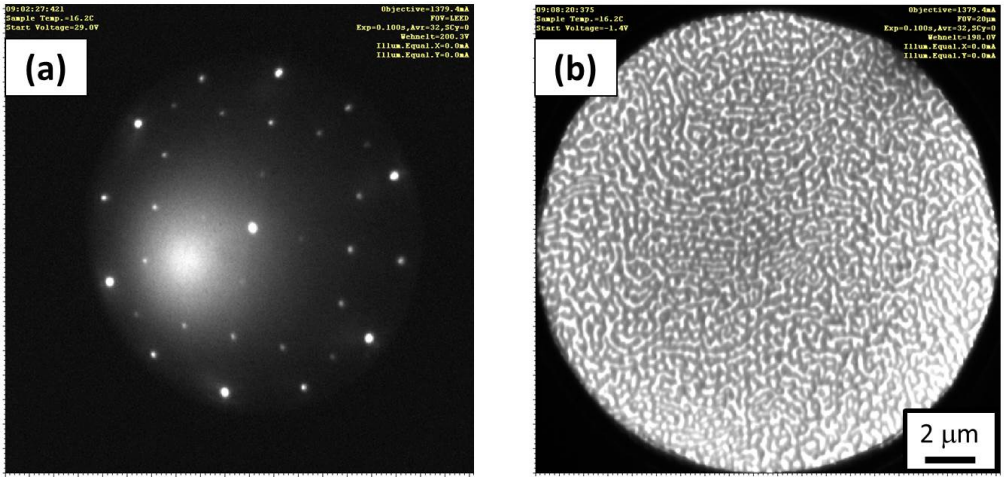

9

Figure 6.9: Ag on Si(100) after heating to 136°C. (a) The LEED pattern shows both Ag(111) 1x1 (with two domains rotated at 90° relative to one another) and Si(100) 1x2/2x1, indicating that dewetting has exposed the bare substrate. One of the Ag 1x1 patterns is now dominant over the other. (b) Bright-field LEEM data shows a "wormy" morphology.

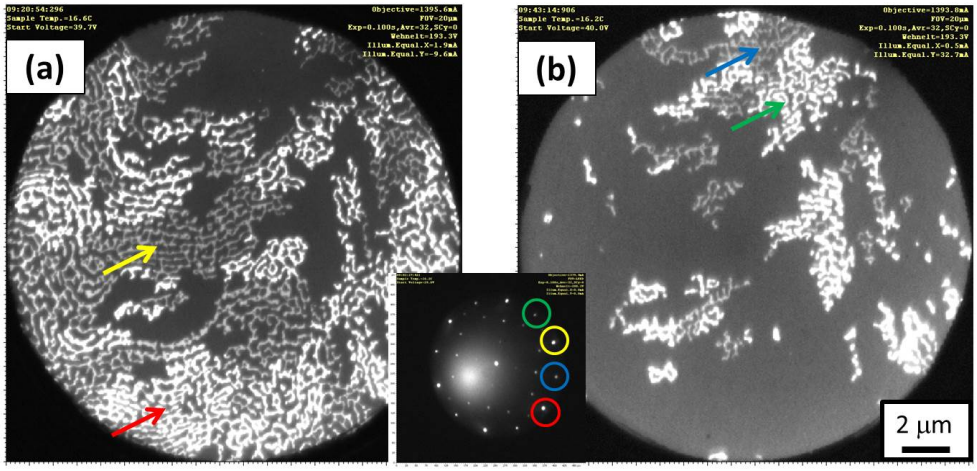

Figure 6.10: Four separate domains emerge after heating to 136°C: two from each of the rotated Ag(111) 1x1 domains. What distinguishes the two inequivalent domains that arise from each of the Ag 1x1 domains is unclear. The diffracted beam corresponding to each domain is circled in the inset LEED pattern and indicated with an arrow of matching color in the real-space image.

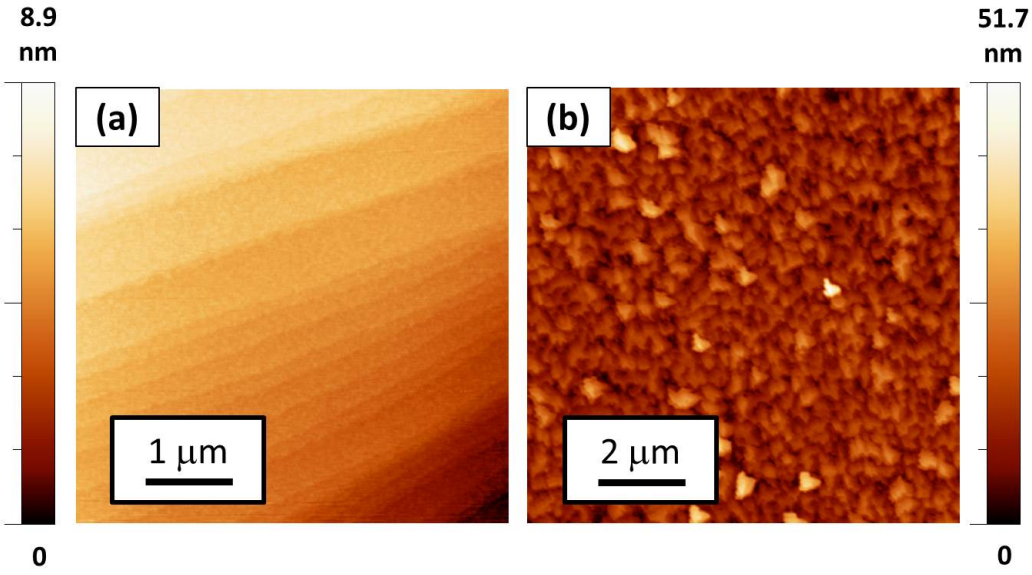

Figure 6.11: (a) 20-ML-thick epitaxial Ag film capped with 2 nm amorphous Ge. Terraces are characterized by sub-nm roughness. (b) 20-ML-thick uncapped epitaxial Ag film on Si(111), from Fig. 6.4.

Chapter 7

Realization of Low-Loss Plasmonic Devices Using Ag Film on Si

By demonstrating two devices whose operating frequencies span the wavelength range from visible to far-infrared we have established that epitaxial Ag film is a plasmonic device platform that is superior to traditional Ag film plasmonic platforms. The success of the first device, a continuous-wave green semiconductor nanolaser, shows that epitaxial Ag exhibits low plasmonic losses in the visible range and that Ge-capped Ag is robust for device applications in ambient conditions (*i.e.,* standard temperature and pressure (STP)). The second device, a thick (80 nm) uncapped film patterned with an array of holes, enabled us to use extraordinary optical transmission (EOT) to assess the relative plasmonic lossiness of epitaxial and rough polycrystalline film in the mid- to far-infrared regimes, and to determine that lower levels of loss occur in epitaxial film. EOT data also demonstrate that thick epitaxial film can be patterned and optically probed in air over a time scale as long as weeks to months, and yield important insights into the morphological evolution of thick epitaxial film.

7.1 Visible Regime: Green Semiconductor Nanolaser

7.1.1 Motivations and Background

Surface plasmon amplification by stimulated emission of radiation (SPASER), first proposed by Bergman and Stockman in 2003,[136] is conceptually analogous to light amplification by stimulated emission of radiation (LASER). While a laser generates coherent photon emission, a SPASER emits coherent SPPs. A SPASER cavity, analogous to a laser cavity, is formed between SPP reflectors that act as "end mirrors." SPPs, like photons, are bosons, so all SPPs in a cavity can occupy an identical quantum state, and population inversion can be achieved in a gain medium placed adjacent to the surface of a conductor within the decay length of the evanescent field.

Interest in SPASERs has been motivated partly by their potential for use as optical interconnects in hybrid photonic/electronic devices. In integrated circuits (ICs) and devices that employ ICs, interconnects are the wiring that connects circuits or parts of circuits. As device sizes have shrunk, wire diameters have shrunk as well, with resistance increasing accordingly (as $\frac{\rho L}{A}$where ρ = material resistivity, L = wire length, and A = wire cross sectional area). The result is unwanted heating and delays (both in signal propagation and in signal rise time) proportional to resistance.[137] These effects can be particularly problematic for long interconnects linking circuits that are far away from each other on separate chips. A study by N. Magen and colleagues in 2004 found that "in a state-of-the-art high-performance microprocessor designed for power efficiency," more than 50% of dynamic power

consumption was interconnect power dissipation.[138] The International Technology Roadmap for Semiconductorswhich maintains a working group devoted solely to this topic and includes in each of its reports a chapter on challenges relating to interconnectsnoted in its 2011 report that "for the long term, material innovation with traditional scaling will no longer satisfy performance requirements," and that "interconnect innovation" is necessary.[139] Optical interconnects might offer an alternative to traditional metallic wiring, as the ITRS Interconnect Working Group concluded in the same year, noting that advantages would include high bandwidth operation, noise immunity, and low-power operation. However, as the group also observed, implementation of optical interconnect schemes has been hindered in part by the challenges of integrating optical interconnects and electronic circuitry, particularly as regards optical/electrical conversion.[140]

SPASERs can potentially mediate the optical/electrical conversion. An electrically pumped SPASER could, for example, be activated by a traditional electronic circuit to inject a signal into a plasmonic waveguide that acts as an optical interconnect. SPASERS could also be used as amplifiers, to counteract damping of signals in long plasmonic interconnects or in other types of plasmonic circuitry.

For circuitry applications, SPASER dimensions need to be small, not only because of the fundamental engineering imperative to minimize device size for the sake of higher device density on-chip, but also because reducing SPASER size can reduce power consumption and decrease switching time.[102]

From the point of view of electronics for computational applications, decreased switching time translates into faster signal processing. The requirement for miniaturization highlights the importance of using a SPASER, as opposed to a traditional laser, whose cavity dimensions need to be at least on the order of the wavelength inside the laser cavity. SPASERs, by contrast, taking advantage of the tight confinement of SPPs at the surface of a conductor and the shortness of the plasmonic wavelength relative to the corresponding free space wavelength, can be characterized by mode volumes up to 100 times smaller than the diffraction limit. This will be discussed below.

7.1.2 Background: Device Design

Our device design follows upon the work of R. F. Oulton *et al.* [141, 142] In a 2008 computational study, Oulton and colleagues proposed and simulated an SPP waveguiding scheme in which a high-permittivity dielectric cylindrical nanowire is placed in close proximity to a conducting surface (long axis of the nanowire parallel to the surface). The nanowire is separated from the surface by an additional layer of low-permittivity dielectric. The authors simulated a range of nanowire diameters (all on the order of 100s of nm) and varying nanowire-conductor separation distances (ranging from a few nm to 100 nm), in order to calculate electromagnetic (EM) field distributions, cross-sectional mode areas, and propagation lengths for single-mode propagation at λ =1550 nm.

For large nanowire diameters d and separation distances h, Oulton *et*

al. found that the nanowire functions as a cylindrical waveguide, with EM energy concentrated primarily at the waveguide core. This case is illustrated in Fig. 7.1(c) for a simulated nanowire of diameter 400 nm separated by 100 nm from a conductor. In the limit of small nanowire diameter and large separations from the conductor, by contrast, the lowest-loss mode is an SPP mode. For nanowires of intermediate diameter, or for large-diameter nanowires very close to the conductor, a coupled mode emerges at a critical nanowire-conductor separation distance. The coupled mode—shown in Fig. 7.1(d) for a nanowire diameter of 200 nm and separation distance of 100 nm—resembles both the uncoupled cylindrical waveguide mode and the uncoupled SPP mode, inasmuch as the EM energy distribution extends across the nanowire and down to the surface of the conductor. However, if the nanowire is brought still closer to the surface of the conductor, the coupled mode evolves into a mode that resembles neither of the uncoupled modes: the EM energy becomes primarily confined to the small mode area in the dielectric gap between the nanowire and the conductor. This case is illustrated in Fig. 7.1(e) and 7.1(f) for medium-diameter (200 nm) and large-diameter (400 nm) nanowires, respectively. Of particular interest is the fact that the propagation lengths for the coupled modes are comparable to, or even longer than, corresponding SPP modes. Fig. 7.1(b) shows propagation length as a function of nanowire diameter at several separation distances. For reference, the calculated SPP propagation length at an interface between a metal and an oxide is shown by the upper dashed line, and the propagation length at an interface between a metal and

a semiconductor is shown by the lower dashed line. The relatively low losses in the gap mode are due to the fact that this mode is propagating in the low-permittivity dielectric region rather than at the surface of the metal, where Ohmic losses can be high. The hybrid mode is characterized by an effective index of refraction that depends on the effective indices of refraction of both the fundamental cylinder mode, $n_{cyl}(d)$, and the SPP, n_{SPP}.

A waveguide of the design just described becomes a SPASER if the nanowire contains a gain medium. Oulton and his colleagues reported in 2009 the demonstration of a SPASER consisting of a cadmium sulfide (CdS) nanowire on thermally evaporated Ag film, with magnesium fluoride (MgF_2) as the few-nm-thick low-permittivity gap layer.[142] The ends of the nanowire constitute the reflecting ends of the SPASER cavity, due to the discontinuity there in the effective index of refraction. The authors used a Ti:sapphire (pulsed) laser to optically pump the nanowires at a wavelength of 405 nm, and observed lasing at close to 490 nm.

7.1.3 Experimental Procedure: Fabrication of Device

Our device geometry is similar to that of Oulton *et al.,* [142] but with critical differences in choice of materials. Instead of the MgF_2 which Oulton and colleagues used as a gap material, we use SiO_2 (atop the thin lossy layer of Ge that was deposited to prevent the epitaxial Ag film from dewetting). More importantly, whereas they used a CdS nanowire, we use a core-shell nanorod consisting of a gallium nitride (GaN) shell and an indium gallium

nitride (InGaN) core (14% In composition). By replacing CdS with InGaN, we increase the gain coefficient in our device by approximately 50 times (assuming that the gain coefficient of InGaN is similar to that of GaN). Finally, and most critically, the rough, thermally evaporated Ag film in their device was replaced in ours by smooth epitaxial Ag film.

I grew a 40-nm-thick epitaxial Ag film on Si(111) using 4-nm deposition cycles. The substrate temperature was approximately 90 K during growth. Scanning the sample with STM, I found the final root mean squared (RMS) surface roughness to be on the order of a few $\mathring{A}$. After film growth, I and Dr. Jisun Kim capped the film with 2 nm amorphous Ge, as described in Chapter 5. The fact that the Ge was indeed amorphous, and that the Ag film was entirely covered, was established by use of *in situ* RHEED: the Ag(111) 1x1 RHEED pattern vanished completely during deposition and no new discernible RHEED pattern emerged, leaving only diffuse uniform scattering to indicate that there was no long-range order within a depth of a few ML below the sample surface. Once the film was capped with Ge, it could safely be removed from vacuum without risk of dewetting, and we shipped it to our collaborators in the research group of Professor Shangjr Gwo at National Tsing Hua University (NTHU) in Taiwan. They used electron beam evaporation in UHV to deposit an additional 5-nm-thick layer of SiO_2 onto the sample.

Using an established method,[143] members of the group of Professor Gwo grew an array of vertically-aligned InGaN@GaN core-shell nanorods (GaN shell and InGaN core) by plasma-assisted MBE on a Si(111) wafer.

The nanorods grow along the wurtzite polar c-axis direction, with diameter approximately 50 nm and length 33 μm. The InGaN filling factor is approximately 1/3, as can be seen in Fig. 7.2. The nanorods were suspended in isopropanol and dispersed onto the epitaxial Si/Ag/Ge/SiO_2 sample. Because of the nanorods' hexagonal geometry and smooth facets, the nanorods lie flat on the SiO_2 spacer layer, as illustrated in Fig. 7.2(a), and the gap thickness between the nanorod and film is even. Additional information about the nanorods' crystallinity and composition is shown in Fig. 7.2(c).

A control sample was fabricated in identical manner on 20-nm-thick polycrystalline Ag film deposited by electron-beam evaporation onto a quartz substrate. Deposition took place in a UHV environment. The as-grown film was scanned with SEM and did not exhibit any discontinuities visible within the limits of resolution (< 5 nm) of the SEM.

7.1.4 Experimental Procedure: Optical Probing

Optical probing was carried out by the Professor Gwo's research group. The nanorods were pumped optically with a continuous wave (CW) semiconductor diode laser at 405-nm wavelength. The sample was mounted in a liquid-He-flow tunable-temperature cryostat, and tests were carried out at both 78 K and 8 K. Single-nanorod optical excitation and emission collection were performed with a single 100$\times$ objective lens characterized by numerical aperture NA = 0.55 in confocal geometry. Emission was measured with a spectrometer connected to a liquid-nitrogen-cooled charge-coupled device.

7.1.5 Results

Figure 7.3 summarizes the optical data for the device based on smooth epitaxial film. In Fig. 7.3(b) solid circles represent data for intensity versus pump power density, and half-filled circles represent data for peak linewidth versus pump power density. Blue indicates data for tests at 78 K, and red indicates tests at 8 K. The onset of lasing can be identified by the characteristic S-shaped kink in the relationship between pump power density and measured output intensity, and also by the simultaneous plateauing of linewidth-narrowing as a function of pump power density. The lasing threshold can be identified as 3.7 kW/cm^2 for 78 K and 2.1 kW/cm^2 for 8 K, which corresponds to 100 nW and 56 nW per individual nanorod, respectively. The onset of lasing was confirmed, additionally, with a measurement of the second-order photon correlation function $g^{(2)}(\tau)$ by the collaborating research group of Professor Wen-Hao Chang. This data is contained in Fig. 7.4. Emission was collected by a Hanbury Brown and Twiss (HBT) interferometer with 50/50 beam splitter, Si avalanche photodiodes, and time-correlated single-photon counting electronics. Below the lasing threshold, $g^{(2)}(\tau = 0) > 1$, indicating spontaneous emission. Above the lasing thresholds, $g^{(2)}(\tau) = 1$ for all τ, indicating the temporal coherence of lasing.

Fig. 7.3(a) plots measured lineshape as a function of pump power, and Fig. 7.3(c) plots lineshape as a function of sample temperature. The onset of lasing at pump power between 3.5 kW/cm^2 (green) and 4.7 kW/cm^2 (purple) is accompanied by the emergence of a sharp, narrow lineshape consisting of

distinct peaks at 510 and 522 nm. Fig. 7.3(c) reveals the emergence of this same lineshape at pump power 8.3 kW/cm^2 when the sample temperature is lowered below 120 K. The inset to Fig. 7.3(a) shows the far-field laser spot: contrast fringes are clearly visible, indicating spatial coherence.

Defining the nanorod's long axis (the wurtzite c-axis) as x, and letting the y-axis lie in the plane of the Ag film, ratios of measured x- to y-polarization were found to be 96% for the 510-nm mode and 60% for the 522-nm mode. Additional details are given in [134].

By contrast, no lasing was observed in the device based on polycrystalline film. A side-by-side comparison of the "light-light" (L-L) curves—*i.e.,* plots of pump power density versus measured output intensity—for devices based on epitaxial and polycrystalline film is shown in Fig. 7.5. Both panels show data acquired at 8 K, the lowest temperature at which we were able to acquire data in this experiment. Fig. 7.5(a) shows the L-L curve for the epitaxial device: the "kink" region of steeper slope s, indicating the onset of lasing, is easily identifiable. In Fig. 7.5(b) there is no kink, and hence no lasing. It is important to emphasize that the device based on smooth epitaxial film exhibited lasing at 120 K (see Fig. 7.3) under CW pumping, whereas the device based on rough thermally evaporated film exhibited no lasing even when the temperature was decreased to 8 K and even under pulsed pumping.

7.1.6 Analysis of Results: Role of Film Quality

In 2009, Oulton *et al.* wrote that "the technical challenge of constructing...plasmonic lasers lies in ensuring good contact between the nanowire and the planar optical film...contact is limited by film roughness [if the nanowires themselves exhibit atomically smooth facets]."[142] In particular, the authors emphasize that film roughness leads to gap-width variation. Using thermally evaporated Ag films, they achieved an RMS film roughness of about 1 nm and gap width variation less than 2 nm. The few-$\mathring{A}$ surface roughness of our device is a significant improvement over that earlier work.

Several sources of loss can increase the lasing threshold of the SPASER: as discussed in Chapter 3, these include Ohmic loss, radiation leakage to the substrate, and emission to outside the cavity. It is in the last of these where lies the most significant difference between SPASERs based on epitaxial and on rough thermally evaporated film. On epitaxial film, SPPs couple out of the cavity into coherent SPP emission and into freely propagating coherent and polarized EM modes only at the two ends of the nanorods. By contrast, on thermally evaporated film SPPs are coupled out of the cavity not only at the nanorod's ends but also in random directions due to scattering at rough surface features all along the cavity's length. A theoretical study of emission from the cavity was undertaken by the research group of Dr. Gennady Shvets. The nanolaser and film were simulated in 3D using finite element analysis in the COMSOL software package: discussion can be found in reference [134]. To characterize the effects of surface roughness on the lasing threshold, a rough

surface was simulated with random features 10 nm in peak-to-valley height. This surface is shown in Fig. 7.6(e). Fig. 7.6(d) shows the simulated Poynting flux (symbolized by white arrows whose size indicates magnitude) from a nanolaser based on the surface shown in Fig. 7.6(e): as can be seen, there is significant random scattering out of the cavity in multiple directions. For comparison, emission from a cavity based on smooth continuous film was also simulated, and is shown in Fig. 7.6(a). The mode volume for this simulated rough cavity is three times that for the simulated device based on smooth film (1.13×10^{-20} m^3 for the rough cavity, as opposed to 4×10^{-21} m^3 for smooth film).

An additional simulation was performed for an Ag film that is granular in addition to being rough. A morphology based on the findings of H. Wei *et al.* [144] for thermally evaporated Ag films on glass was modelled: random small grains with irregular boundaries and a characteristic length of 20 nm. The interstices between these grains were taken to be vacuum ($\epsilon_0 = 8.8541878 \times 10^{-12}$ F/m). Based on the findings of Wei and colleagues for the thickness dependence of the filling fraction of the Ag grains, 90% was estimated as the appropriate filling fraction for 28-nm-thick thermally evaporated film like that used in our experiment. The results are shown in Fig. 7.6(b): comparing the Poynting flux with that in Fig. 7.6(a) it is easy to see that random scattering from the cavity is higher for the granular film. The simulated mode volume 1.77×10^{-20} m^3 for the granular film is four times the mode volume for the smooth continuous film, and about 1.5 times the mode volume for a rough but

continuous film. Such poor cavity confinement is a critical contributing factor to the increased lasing threshold observed in our experiment for the device based on thermally evaporated film.

7.2 Infrared Regime: Extraordinary Optical Transmission through Thin Ag Film

7.2.1 Motivations and Background

Although our SPASER provides compelling evidence that surface roughness plays a primary role in damping SPPs in Ag films in the visible range, it does not directly address the causes of SPP damping at longer wavelength regimes. In order to study plasmonic damping in the mid- and far-infrared regimes, we used extraordinary optical transmission (EOT) to quantitatively compare the strengths of SPP resonances in epitaxial and rough polycrystalline films at these longer wavelengths. T. Ebbesen and his colleagues showed in 1998 that a periodic array of holes fabricated in a metallic film can mediate coupling between SPP resonances on the top and bottom surfaces of the film.[93] They investigated the case of circular holes with diameters smaller than the wavelength of incident light: the hole diameters were on the order of hundreds of nm, while the incident wavelengths spanned the range 1000–2500 nm. Theory set forth by H. A. Bethe in 1944 predicts that transmission efficiency—defined as $\frac{TransmittedIntensity}{IncidentIntensity}$ divided by the fraction of the surface area occupied by holes—is proportional to $(\frac{a_0}{\lambda})^4$. Hence, for a small hole radius and a large incident wavelength, transmission efficiency is expected to be very

small.[145] From an alternative point of view, if one considers the hole array to be a grating, then zero-order transmission intensity would be expected to fall off for large wavelengths as $I \propto \lambda^{-1}$. By either analysis, transmission through an array of sub-wavelength-diameter holes is predicted to be small. Nevertheless, Ebbesen *et al.* observed strongly enhanced transmission at particular long wavelengths. Their conclusion was that periodic hole arrays couple incident light of particular frequencies into SPP resonant modes and mediate coupling between SPP resonant modes on the top and bottom surfaces of a film. The SPP modes can then recouple, again at the locations of the holes, into radiative modes, with the result that a detector positioned behind the film will measure strong transmission at certain wavelengths that are much longer than the hole diameter.

To understand these results, consider a flat metallic surface patterned with a periodic structure. We define the momentum wave vectors (*i.e.,* reciprocal lattice) of the structure as $G_x = \frac{2\pi}{a_{0x}}$, $G_y = \frac{2\pi}{a_{0y}}$, where a_{0x} and a_{0y} are the periodicities in the x and y directions, respectively. Suppose that an EM plane wave with wave vector $k_0 = \frac{2\pi}{\lambda}$ is incident upon this structure, and let θ be the angle that the incident wave makes with the normal. Then momentum matching dictates that an incident wave will be able to couple to a surface plasmon resonance if

$$k_{SPP} = k_0 \sin\theta \pm nG_x \pm mG_y, \tag{7-1}$$

where n and m are integers. Recalling also that $\vec{k_{SPP}}$ is related to the

free-space wave vector of incident light by the relation

$$k_{SPP} = k_0 \sqrt{\frac{\epsilon_d \epsilon_m}{\epsilon_d + \epsilon_m}}, \tag{7-2}$$

only discrete plasmonic resonances will be excited, dependant on both the incident wavelength and the angle of incidence.[69] Minimally damped (i.e., "strong") plasmonic resonances are identifiable by sharp transmission peaks of high intensity. By comparing the strength and sharpness of transmission intensity maxima through epitaxial and rough polycrystalline films, we can compare plasmonic damping in the two types of films.

7.2.2 Experimental Procedure: Fabrication of Device

For this study I fabricated a 79-nm-thick epitaxial Ag film on Si(111). (Si wafer was low-doped with Ph (n-type doping), and specified by the manufacturer as 1500–2500 Ω-cm. Wafer thickness was specified as 400μm.) I deposited 4 nm in the first deposition cycle, and 5 nm in each deposition cycle thereafter. The substrate temperature was approximately 110–130 K during growth. I used LEED to confirm the sample crystallinity after each annealing. Fig. 7.7 is the LEED pattern after the final growth cycle. It is the characteristic one for Ag(111) 1x1, with spots that are relatively sharp and clear, indicating the expected long-range order and a definite crystalline orientation. A second film of polycrystalline Ag grown to the same thickness on the native oxide layer of Si(111) was also prepared as a control. Because of the thickness of the film used in this experiment, film dewetting was slow and Ge capping

was not necessary (see Section 7.2.5 for more information on film dewetting).

After the films were removed from vacuum Dr. Bohong Li, of the research group of Professor Xianggang Qiu at the Beijing National Laboratory for Condensed Matter Physics and Institute of Physics, Chinese Academy of Sciences, used ultraviolet photolithography and reactive ion etching (RIE) to pattern the epitaxial and thermally evaporated films with square arrays of circular holes. The hole diameter was 3 μm, and the array period was 6 μm. (The epitaxial film was out of vacuum for approximately 2–4 weeks for shipping, and was thereafter stored in a clean environment at a pressure of 0.1–1 Torr.) For purposes of illustration, Figs. 7.8(a) and (b) show SEM images of patterned polycrystalline and epitaxial Ag films, respectively. The epitaxial film shown here is not the one used in our optical measurements, but was prepared in a manner identical to that used to make the samples we investigated. We did not use SEM to scan our primary sample because we did not want to damage the sample by exposure to the electron beam. As can be seen, the hole diameter in the SEM here is slightly smaller than the hole diameter used in our actual study. The polycrystalline film is the film that was actually used in our measurements, but the SEM was obtained after our study of that film was complete.

7.2.3 Experimental Procedure: Optical Probing

The technique used to probe the samples was Fourier transform infrared spectroscopy (FTIR). The FTIR data was obtained by Dr. Bohong Li and

Professor Xianggang Qiu. The setup is indicated schematically in Fig. 7.9. Taking the sample plane to be the xy plane, as in the figure, the sample was rotated in 2° increments around the y axis. The incident beam—which was focused on the Ag side of the sample (from the right, in the figure)was limited by a 5-mm-diameter diaphragm, and passed through a linear polarizer so that transverse electric (TE) and transverse magnetic (TM) data could be acquired at each measurement angle. Transmission intensity was measured with a detector on the Si side of the sample (on the left, in the figure). MIR data was collected with a liquid-nitrogen-cooled mercury cadmium telluride (MCT) detector, while FIR data were collected with a liquid-helium-cooled bolometer.

Spectra were also obtained, in an identical manner, for transmission through a bare Si(111) substrate from the same wafer, but with native oxide left on the surface. The transmission spectra of the Ag/Si samples were normalized with respect to the spectra of bare Si.

Spectra were obtained from the epitaxial sample in the mid-infrared (MIR) range within 1–2 months of the original sample fabrication, and in the far-infrared (FIR) within 3 months. From the polycrystalline film, spectra were obtained within about 4 months of fabrication. Except when being patterned and probed, the samples were stored at 0.1–1 Torr. We can roughly estimate the total time that the samples spent in ambient conditions, from the time of fabrication until the spectroscopic studies were complete, to be several weeks.

7.2.4 Results

The normalized spectra of transmission intensity are shown in Fig. 7.10 (reproduced from [114]). Panels (a)–(f), on the left, show normalized transmission intensity represented by false color. Resonances are identifiable as sharp borders across which intensity changes rapidly. The false color scale has been modified in each panel, in order to make the resonances as visible as possible. The horizontal axis represents wavelength. The leftmost column contains MIR data, while the second-to-left column contains FIR data. The vertical axis represents incident angle θ relative to the sample normal (see Fig. 7.9). Panels (g)–(l), on the right side of the figure, show details of individual spectra acquired at $\theta = 20°$, with the vertical axis now representing normalized transmission intensity. In all columns the top and middle rows contain data acquired from the polycrystalline control sample and the epitaxial sample, respectively. The bottom row shows simulated transmission spectra produced by our collaborators in the group of Dr. Gennady Shvets. The simulations were created using the COMSOL software package, with Ag modeled as a flat perfect electric conductor (PEC): $\epsilon_{PEC} \to -\infty$. As explained in Chapter 3, the magnitude of the real part of the dielectric function of Ag blows up for long wavelengths. The real part of the relative permittivity of Ag is Re(Ag)$\approx$ -1100 at 6 μm, and the absolute value continues to increase with wavelength.[146] By contrast, Re(Air)$\approx$ 1 and Re(Si)$\approx$ 11.9 (relative permittivities), so -Re(ϵ_{Ag}) $\gg$ Re($\epsilon_{Dielectric}$) at both interfaces, and we can treat ϵ_{Ag} as effectively infinite. This justifies modeling Ag as a PEC in this wavelength range.

The simulated false color spectra include black lines as guides for the eye, showing the locations of resonances and labeled "air(m,n)" or "Si(m,n)" depending on whether they represent plasmonic resonances at the air/Ag or Si/Ag interface. The indices m, n refer to the momentum-matching condition discussed above (Equation 7-1). The far-right column includes a dashed blue line to highlight the location of the Si(1,0) mode; likewise, a dashed red line highlights location of the air(1,0) mode in the second column from the right.

7.2.5 Analysis of Results

In addition to the predicted EOT resonances indicated by black lines in panels (c) and (f) of Fig. 7.10, a subtle structure is observable in the transmission data, including resonances that appear split or asymmetrical. These features are due to so-called "Wood's anomalies:" essentially, they are interference between higher-order diffraction modes of the periodic structure.[147, 148] The set of Wood's anomalies constitute a band structure which can interfere with the SPP-mediated EOT band structure, leading to abrupt changes in transmission intensity along or across the EOT bands. This can be seen, for example, at $\theta = 40°$, $\lambda = 16.4$ μm, where the Si(1, $\pm$1) and Si(-1, 0) bands cross, with an abrupt shift of intensity along both bands.

Since the simulated PEC represents an ideal case with minimal plasmonic damping, the simulated transmission intensity (see false color scales) is higher than the intensity data collected from either the epitaxial or polycrystalline film. Also, transmission intensity through the epitaxial film is higher

than through the polycrystalline film. Despite the low transmission intensity in the case of the polycrystalline film, however, the main features of the FIR spectrum (second column from left) are preserved both there and in the epitaxial film, and the locations of the resonances as a function of wavelength and angle are well predicted by simulation. In the MIR spectra, too, the locations of longer-wavelength resonances predicted by simulation are in good agreement with the data from both the epitaxial and polycrystalline films. The major difference between polycrystalline and epitaxial film is observed in connection with the air(1,0) resonance. This resonance dominates the simulated MIR spectrum and is extremely sharp in the spectrum acquired from the epitaxial film. However, in the spectrum from the polycrystalline sample, this resonance loses both its sharpness and strength, a fact that is emphasized by the details at 20° that constitute the second column from the right: the air(1,0) resonance in both the simulation and the epitaxial transmission data is manifested by a clear peak on the long-wavelength side of a sharp cutoff and a distinct dip, while in data from the polycrystalline film the peak is reduced to a weak shoulder on the short-wavelength side of the much-more-distinct Si(2,0) peak. For the sake of contrast, the far-right-hand column in the same figure shows a detail (also at 20°) of the Si(1,0) resonance, which is sharp and well-defined in each case.

As discussed in Chapter 3, SPP damping has, in general, several causes. One of these is Ohmic losses in the metal. Another takes place at features and random roughness at the metal's surface: here, loss due to inelastic SPP scat-

tering occurs, as does loss due to SPP coupling into radiation.[95] Ohmic loss and scattering due to patterned features are, presumably, similar in the epitaxial and polycrystalline samples. However, surface roughness is very different, as can be seen in Fig. 3.6 in Chapter 3. The linewidth of EOT transmission intensity bands is determined by the propagation length of SPPs at a film's surfaces: $\Gamma = \frac{\lambda^2}{2\pi n_{eff} L_{SPP}}$ where L_{SPP} is the propagation length and Γ is the linewidth.[149] Conversely, plasmonic damping reduces bands' sharpness. Thus, in the data acquired here, the sharpness of the epitaxial air(1,0) band relative to the polycrystalline air(1,0) band is a key indication of the relative plasmonic lossiness of that interface in the two types of films: in the polycrystalline film, random surface roughness leads to a significant increase in loss due to SPP radiative coupling and inelastic scattering.

We also considered the possibility that air-side damping in the epitaxial film was caused not by scattering but by the formation of a lossy layer on the epitaxial film—for example, a surface oxide. In order to address this question, we used the x-ray photoemission spectroscopy (XPS) facilities at the University of Texas Center for Nano- and Molecular Science, with assistance from Dr. Hugo Celio. I prepared a 10-nm-thick epitaxial Ag film and a 15-nm-thick polycrystalline Ag film, and exposed both of them to air at room temperature for about 36 hours. Dr. Celio and I performed XPS lineshape analysis of the Ag 3d signal. No oxide signal (either AgO or Ag_2O) was detectable on either type of film, although sub-detection levels (e.g., 1–2 ML oxide) might have been present. Trace amounts of carbon (C) and oxygen (O)

were easily eliminated by a brief, 1-second sputter, pointing to the presence of no more than a few monolayers of organic adsorbates. No other signals were significant, aside from Si and SiO_2 signals from the polycrystalline sample, due to thickness fluctuations and possible pinholes to the substrate. In applying these results to the interpretation of our original data, the key question is how thick a lossy layer might have accumulated in the 2–4 weeks that our original samples spent out of vacuum before they were probed. Assuming, for the sake of argument, that 1.5 ML oxide or adsorbate were to accumulate on the film every 36 hours, then after 4 weeks there would be a lossy layer of 7 nm thickness. The evanescent SPP field in the MIR range is on the order of 1 μm, and is still longer at longer wavelengths. Thus, a lossy layer of 7 nm or even more would have a minimal effect on SPP damping. More importantly, a significant lossy layer would lead to a shifting of the dispersion relations shown in Fig. 7.10 above. No shifting is observed: the positions of the air-side resonances are identical in the polycrystalline and epitaxial films, and agree with the locations predicted by simulation. Thus, we can safely conclude that the primary cause of increased damping in air-side SPPs on the polycrystalline film is scattering and radiative losses due to surface roughness, rather than losses due to the presence of an additional lossy layer.

Scattering and radiative losses on the air side of the polycrystalline film are compatible with the model of film morphology shown schematically in Fig. 7.11. The model epitaxial film, depicted on the right, is flat and smooth on both the air and Si sides of the film. The model polycrystalline film, on the

left, consists of clusters that are rounded on top but flat and smooth on the bottom surface where they are in contact with the Si substrate. Evidently, the Si side of the polycrystalline film is similar in smoothness to the Si side of the epitaxial film, with the result that SPP resonances at that interface are sharp and similar in lineshape to those of the epitaxial film. This model of film morphology is supported by the work of P. Nagpal *et al.,* [150] who showed that ultra-flat surfaces capable of supporting SPP propagation with low loss could be obtained by "stripping" rough, thermally evaporated film from its substrate to expose its smooth underside.

A footnote to this experiment sheds light on epitaxial Ag film dewetting. After the data shown above was collected, the epitaxial film was held in a drying cupboard at room temperature for about 2 years, and then the optical measurements were repeated. The results are shown in the bottom row of Fig. 7.11. The first three rows show details, taken from the original data discussed above, of the air(1,0) resonance. Each column represents a particular incident angle, with the angles indicated at the heads of the columns. The horizontal and vertical axes are wavelength and transmission intensity, respectively. The air(1,0) band is highlighted with a region of shading. In the two-year-old epitaxial film the sharpness of the air(1,0) resonance has degraded, and the line shape appears to be approaching that of the polycrystalline film. This is compatible with the interpretation that the morphology of the epitaxial films surface is transforming to resemble that of the polycrystalline film, presumably by roughening at the top surface, and possibly by clustering. An SEM image

was taken of the degraded film, and is shown in Fig. 7.12(c), together with the original SEM images of the original patterned polycrystalline (Fig. 7.12(a)) and epitaxial (Fig. 7.12(b)) films from above.

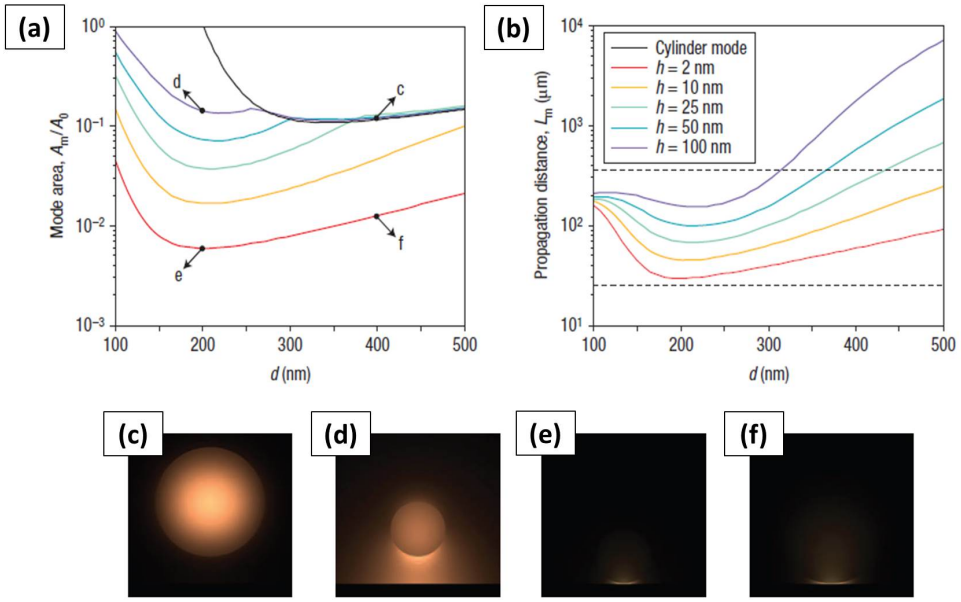

Figure 7.1: From [141]. Original caption: propagation distance, mode area, and field distributions of the hybrid mode. (a) [Normalized] mode area, $\frac{A_m}{A_0}$ versus cylinder diameter d for different gap widths h (colored lines), compared with the mode area of a pure cylinder mode (black line). [A_0 is the diffraction-limited mode area in free space, $A_0 = \frac{\lambda^2}{4}$. A_m is the calculated mode area of the hybrid mode.] (b) The hybrid mode's propagation distance (colored lines), compared with those of pure SPP modes at metal-oxide (upper dashed black line) and metal-semiconductor (lower dashed black line) interfaces. (c)–(f) EM energy density distributions for $[d, h] = [400, 100]$ nm (c), $[d, h] = [200, 100]$ nm (d), $[d, h] = [200, 2]$ (e), and $[d, h] = [400, 2]$ nm (f), corresponding to the points indicated in panel (a). The key in the inset of (b) applies throughout. Reprinted by permission from Macmillan Publishers Ltd: *Nature Photonics*, copyright 2008.

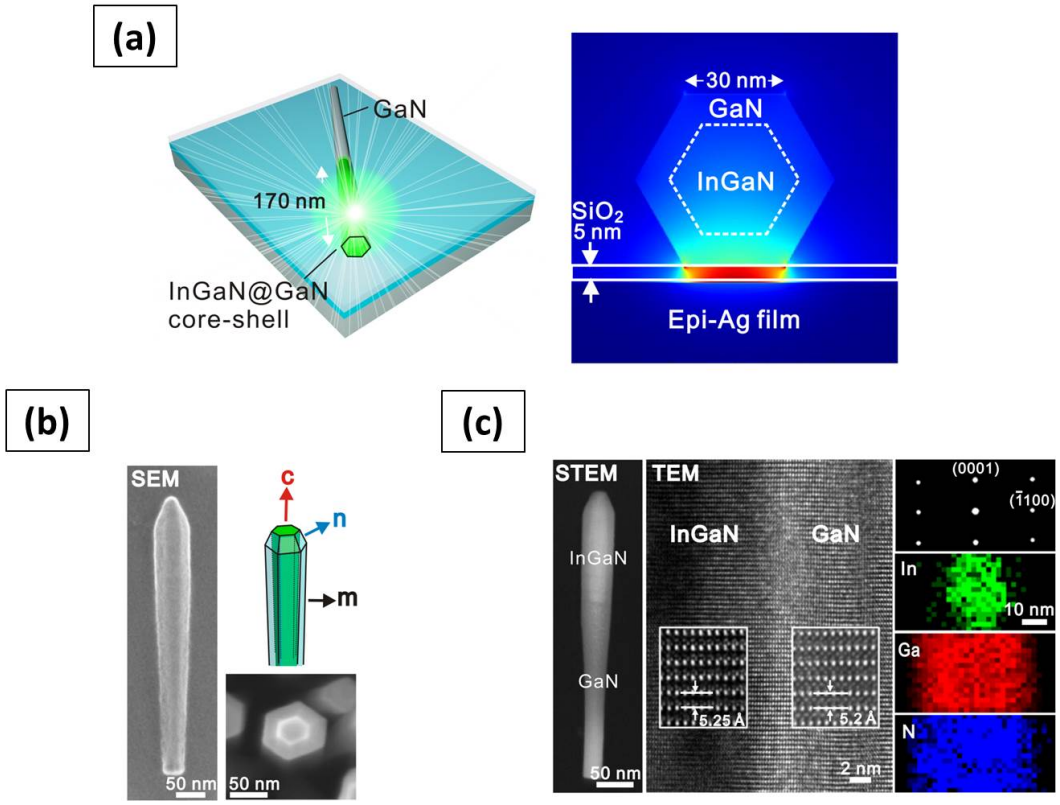

Figure 7.2: From [134]. Original caption: (a) Schematic of device: a single InGaN@GaN core-shell nanorod on SiO_2-covered epitaxial Ag film (28 nm thick). The energy density distribution (right) is calculated by [the group of Dr. Gennady Shvets using] the eigenmode method. (b) SEM images of InGaN@GaN core-shell nanorods. The left-hand SEM image shows the actual nanorod on epitaxial Ag film that was used for all lasing measurements. (c) Scanning transmission electron microscopy (STEM) and transmission electron microscopy (TEM) structural analyses of a single-crystalline InGaN@GaN core-shell nanorod. The bright area inside the nanorod in the high-angle angular dark-field STEM image indicates the presence of the InGaN core. The elemental mapping images obtained by energy dispersive x-ray spectroscopy are used to confirm the core-shell structure and to estimate the In composition in the InGaN core (∼14%). [Data in (c) obtained by the research group of Professor Lih-Juann Chen of National Tsing-Hua University, Taiwan.] Reprinted with permission from AAAS.

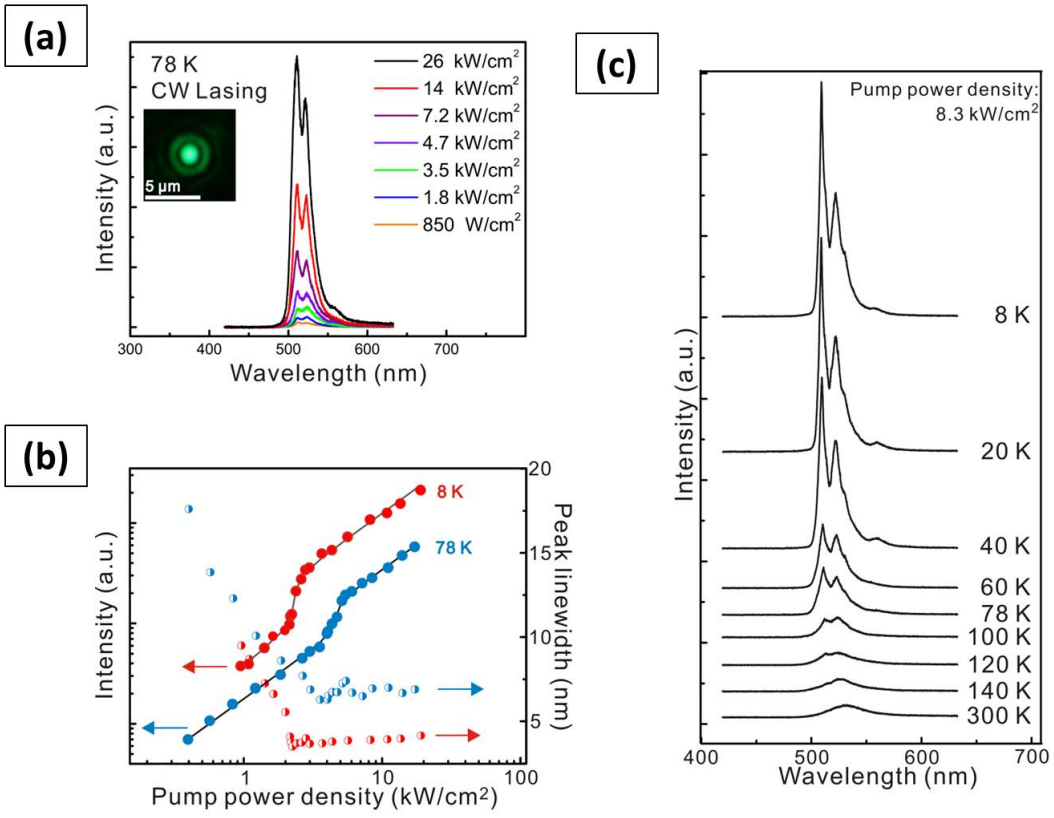

Figure 7.3: From [134]. Original caption: (a) Lasing spectra for pumping by a CW 405-nm semiconductor diode laser. Inset: Far-field laser spot with contrast fringes indicative of spatial coherence resulting from lasing.... (b) Temperature-dependent lasing thresholds of the plasmonic cavity. The...plots at the main lasing peak (510 nm) are shown with the corresponding linewidth-narrowing behavior when the plasmonic laser is measured at 8 K (red) and 78 K (blue), with lasing thresholds of 2.1 and 3.7 kW/cm^2, respectively. (c) Temperature-dependent lasing behavior from 8 to 300 K. [All intensity data are given in arbitrary units (a.u.).] Reprinted with permission from AAAS.

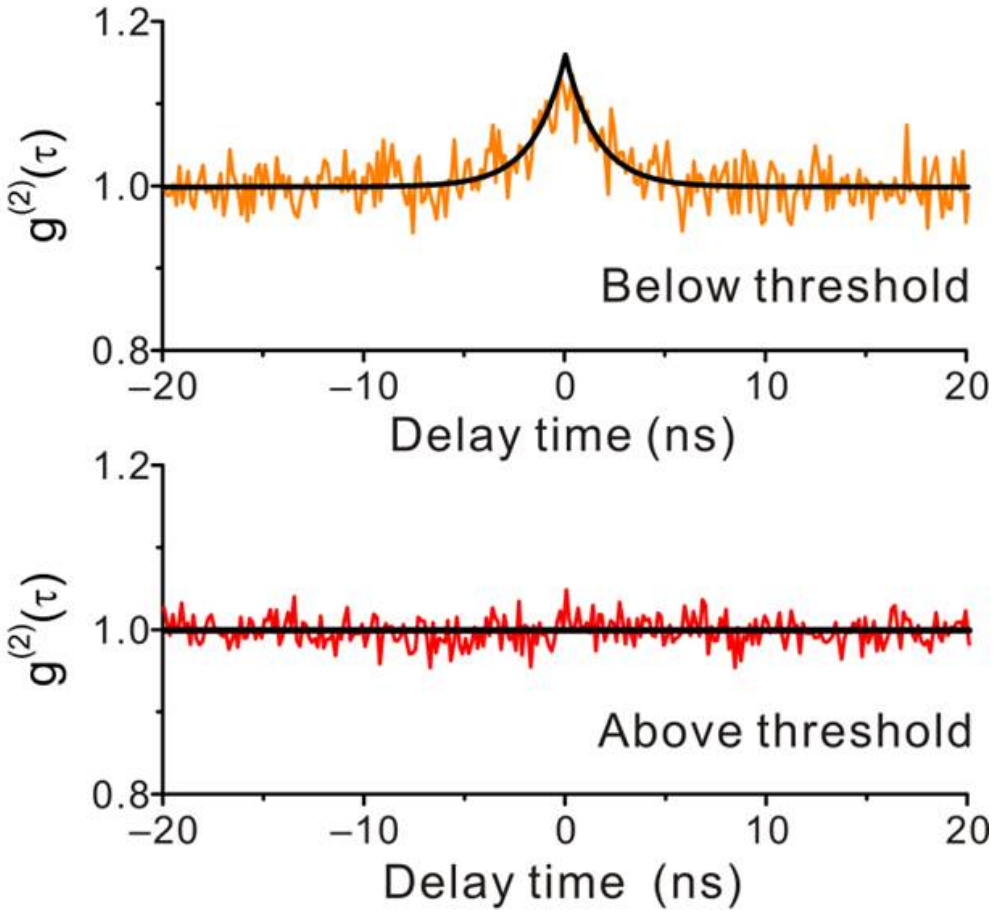

Figure 7.4: From [134]. Original caption: Second-order photon correlation function measurements [made by the research group of Dr. Wen-Hao Chang at National Chiao-Tung University, Taiwan] at 8 K. Reprinted with permission from AAAS.

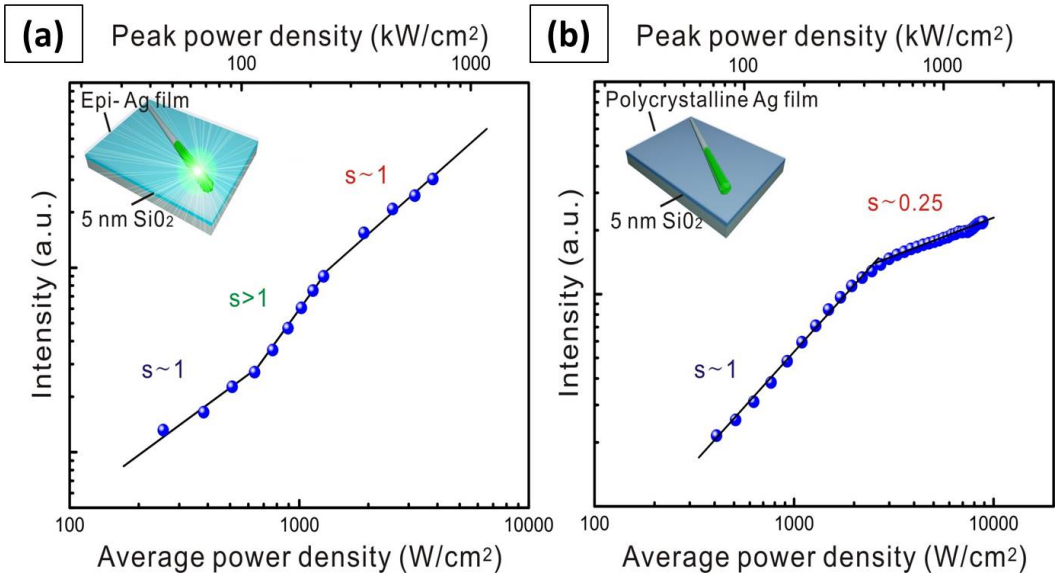

Figure 7.5: From [134]. Original caption: Side-by-side comparison of L-L curves under pulsed pumping conditions for single nanorods placed on two types of Ag films (epitaxial Ag-on-Si film vs. polycrystalline Ag-on-quartz film). We obtained these curves at 8 K using a pulsed semiconductor diode laser (PicoQuant) with the following characteristics: 405 nm wavelength, 70 ps pulse width, and 80 MHz repetition rate. (a) The "S"-shaped lasing curve can be clearly observed for the case of epitaxial Ag film. (b) The L-L curve for a single InGaN@GaN core-shell nanorod deposited on polycrystalline Ag film. Under these pumping conditions, we cannot observe lasing on polycrystalline film for pumping power densities up to 9 kW/cm^2 (i.e., peak pumping power density 1.6 MW/cm^2). The onset of slope s less than one ($\sim$0.25) at peak power densities greater than 450 kW/cm^2 indicates that local, transient heating effects start to play a significant role in output intensity. Reprinted with permission from AAAS.

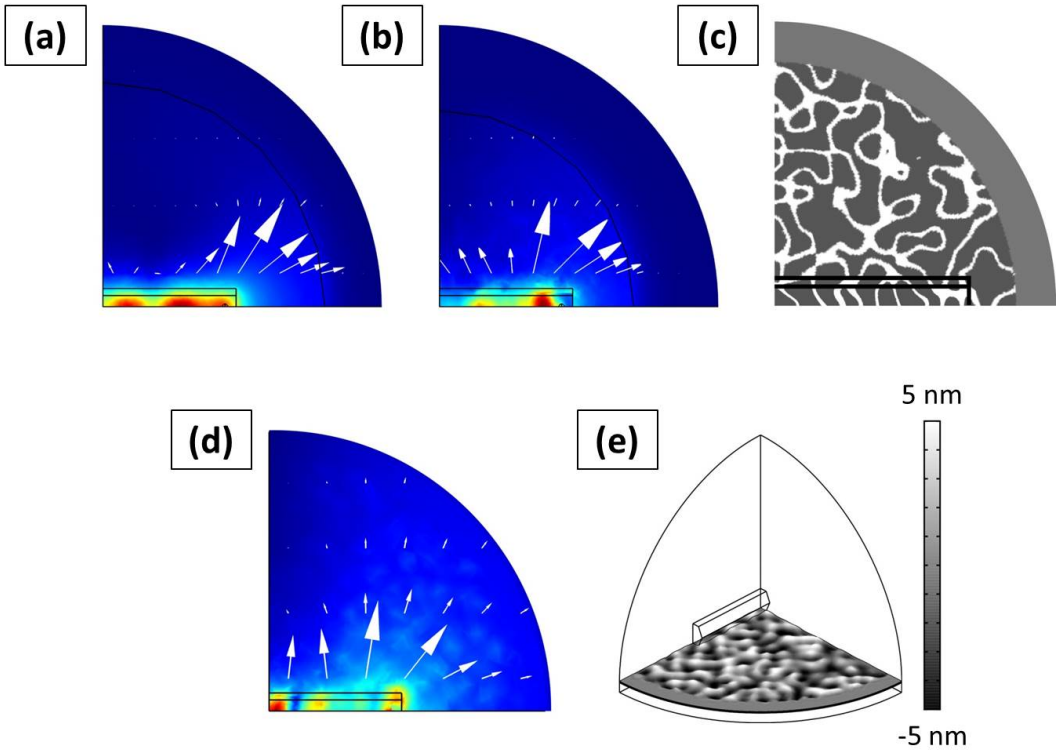

Figure 7.6: From [134]. Original caption: Plasmonic resonances, with the nanorod placed on top of (a) an atomically smooth Ag film, (b) a granular Ag surface with domain walls, and (d) a roughened Ag surface with non-uniform thickness. The color maps show the electric field, $|\vec{E}|$, 10 nm above the surface, and the arrows indicate the Poynting flux. (c) Map of the Ag permittivity used to represent the granular surface in (b). White area represents the grain boundaries with [relative permittivity] ϵ =1. (e) Illustration of the surface deformation simulated in (d). Reprinted with permission from AAAS.

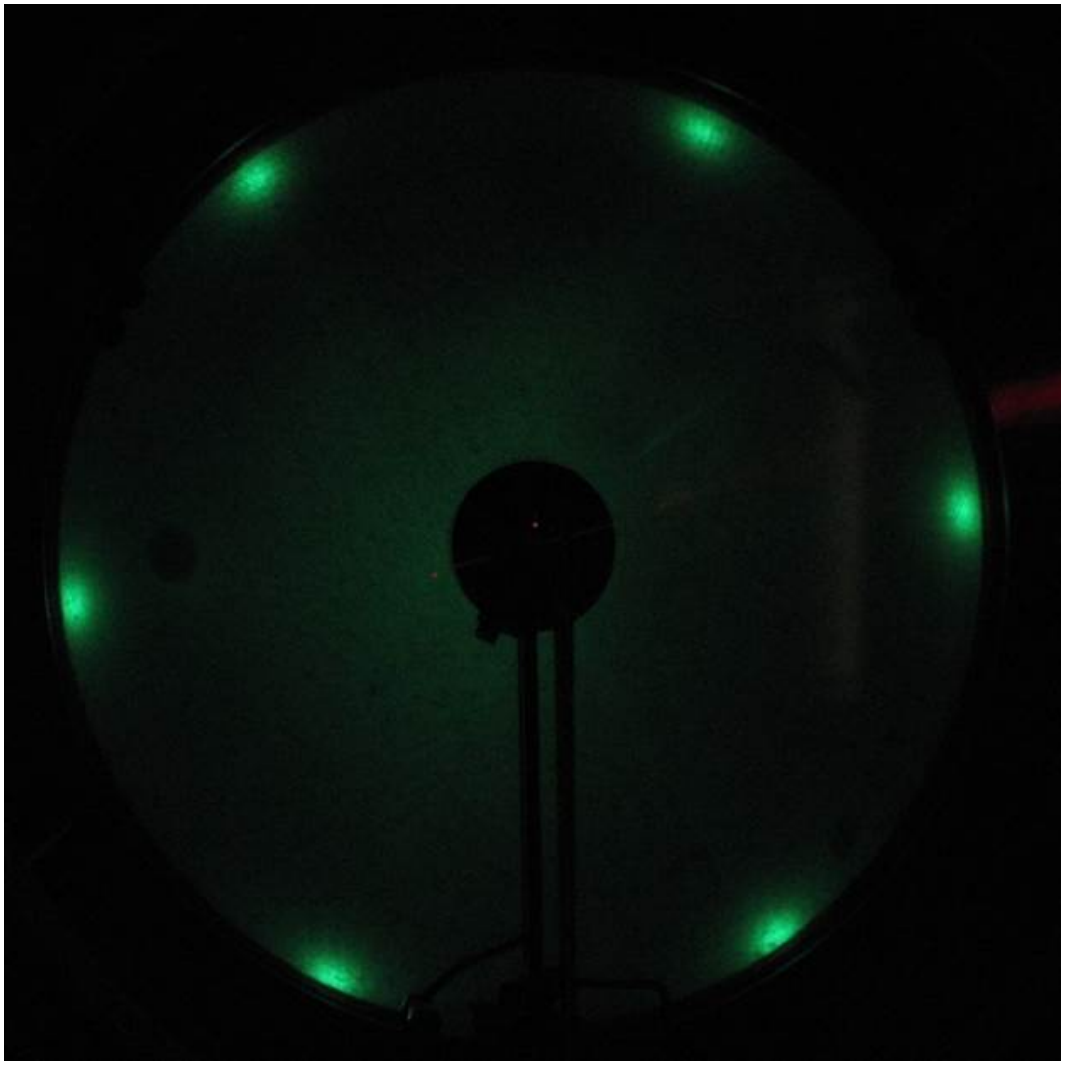

Figure 7.7: LEED pattern acquired after final epitaxial growth cycle for EOT device. Pattern indicates good Ag(111) crystallinity with 1x1 surface structure.

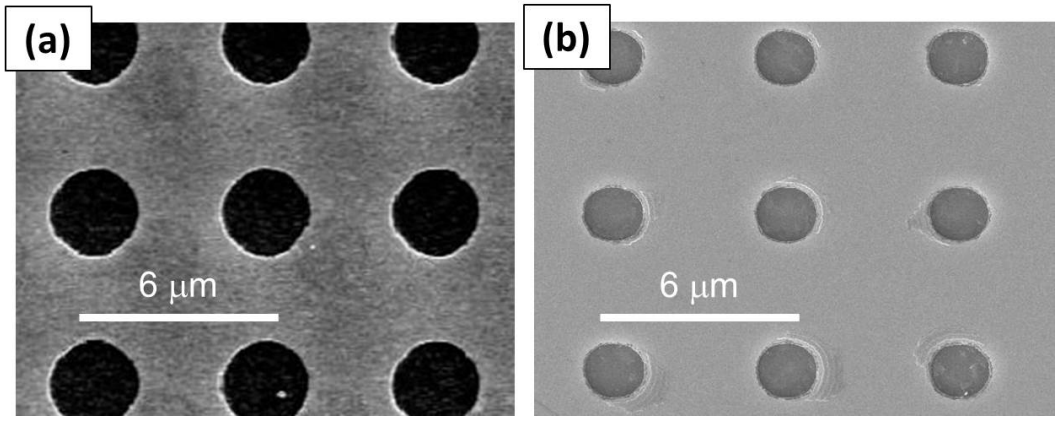

Figure 7.8: From [114]: SEM images of patterned Ag films. (a) Thermally evaporated polycrystalline film. (b) Epitaxially grown film. Reprinted with permission. Copyright 2012, American Chemical Society.

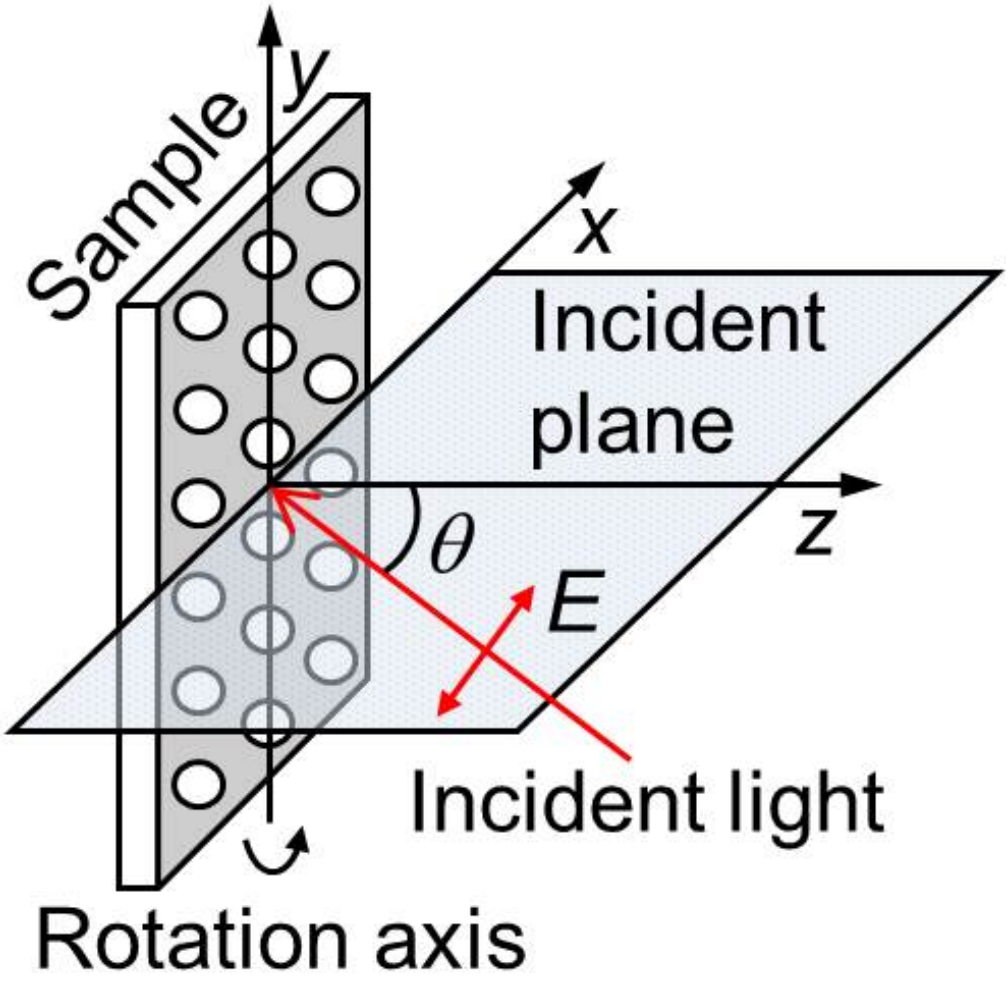

Figure 7.9: From [114]. Original caption: Schematic of the configuration for angle-resolved EOT measurements in the infrared regime under TM-polarized illumination. Incident light is in the x-z plane, *i.e.,* the incident plane. The electric field $\vec{E}$ also lies in the incident plane. Variation of the incident angle θ is obtained by rotating the sample around the y-axis. Reprinted with permission. Copyright 2012, American Chemical Society.

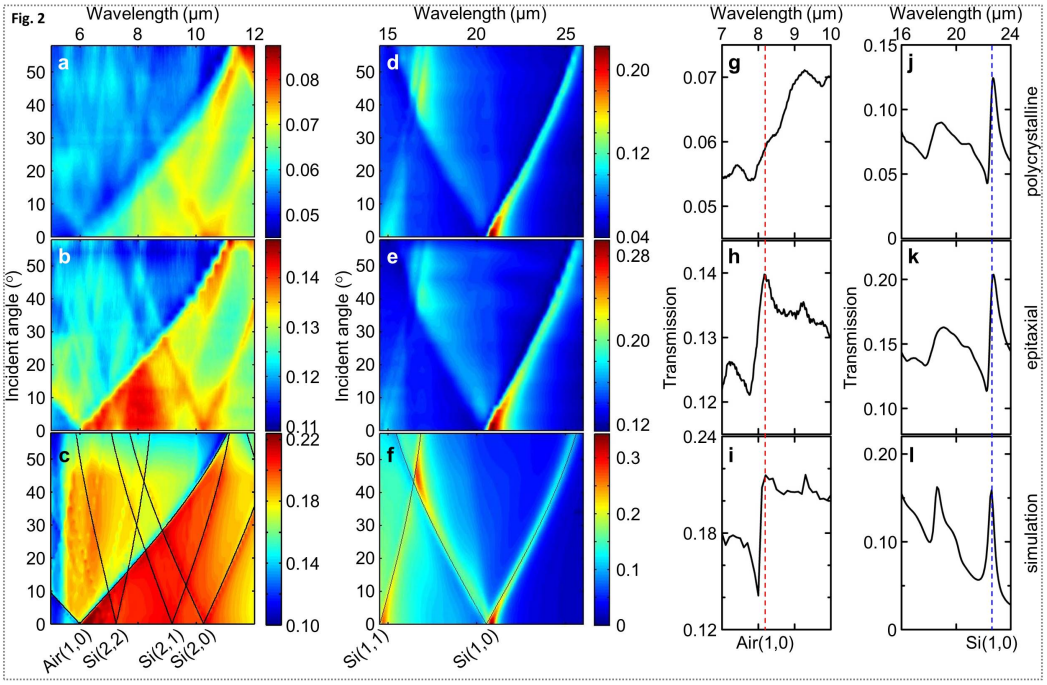

Figure 7.10: From [114]. Original caption: Experimental and simulated angle-resolved EOT transmission spectra in the infrared regime. (top and middle rows) Experimental angle-resolved infrared transmission spectra under TM-polarized illumination for perforated polycrystalline (top row) and epitaxial (middle row) Ag films. (bottom row) Simulation results from the commercial software package COMSOL, using the real geometric and material parameters except for the substitution of a PEC film for the Ag film. Both perforated Ag films (top and middle rows) and the PEC films (bottom row) have a thickness of 80 nm, a lattice period of 6 μm, and a hole diameter of 3 μm. (a–f) Contour plot with intensities indicated by false color. Theoretcial SPP bands (black solid) are superposed on (c,f), with different SPP modes indexed by Si(m,n) or air(m,n). (g–l) Individual transmission spectra acquired at 20°. The dashed lines are to guide the eye for the air(1,0) (red) and Si(1,0) (blue) modes, respectively. Reprinted with permission. Copyright 2012, American Chemical Society.

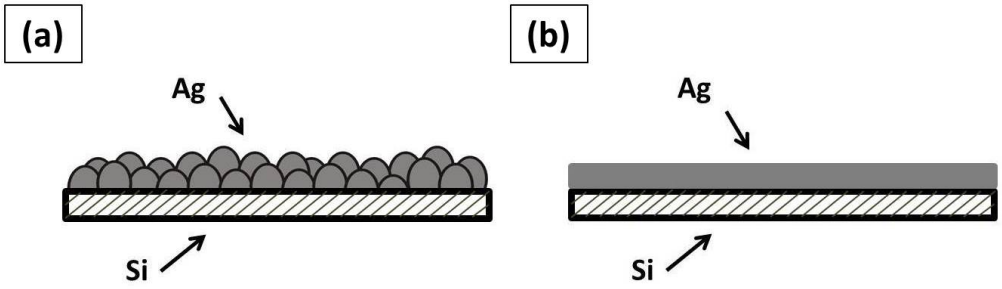

Figure 7.11: Schematic of film morphology for thermally evaporated polycrystalline film, left, and smooth epitaxial film, right. The film-substrate interface is relatively smooth in both cases, but the morphology at the air interface is much different.

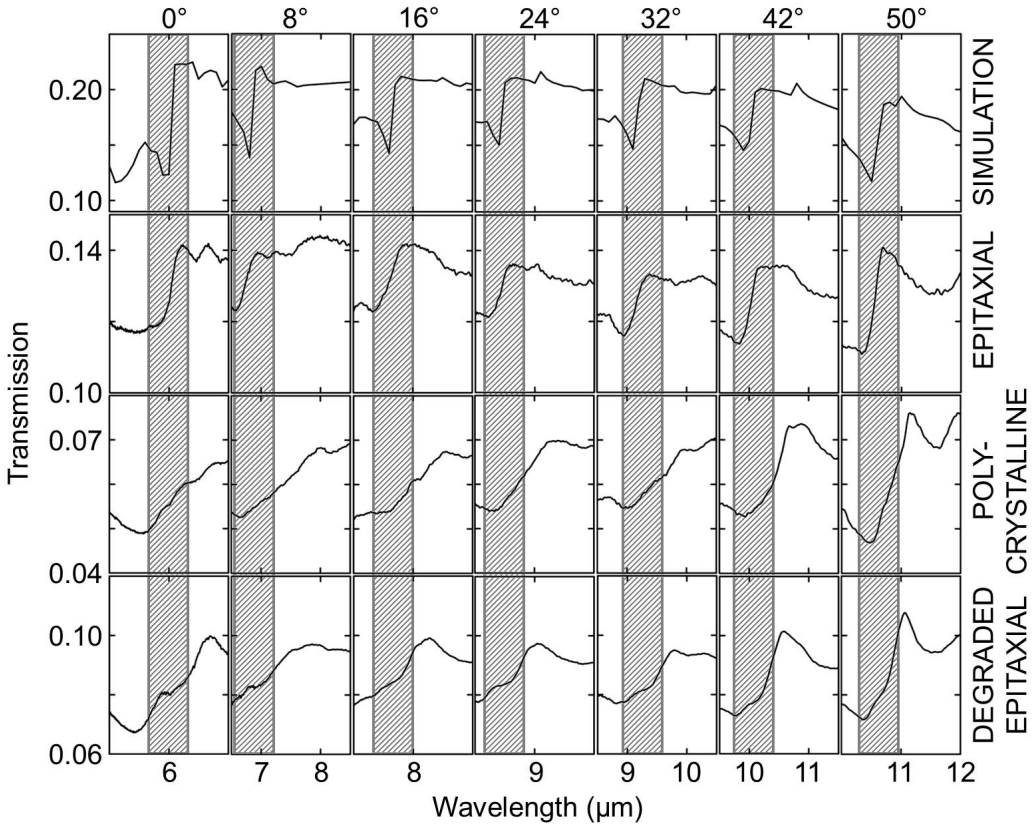

Figure 7.12: From [114]. Transmission spectra showing degradation of air-side resonance features after two years exposure to ambient conditions. Original caption: Experimental and simulated transmission spectra for the air(1,0) mode (shadow area). (1st row) Simulated transmission spectra. (2nd row) Experimental transmission spectra from perforated epitaxial Ag film. (3rd row) Experimental transmission spectra from perforated polycrystalline Ag films. (4th row) Experimental transmission spectra from the perforated epitaxial Ag film after degradation. Reprinted with permission. Copyright 2012, American Chemical Society.

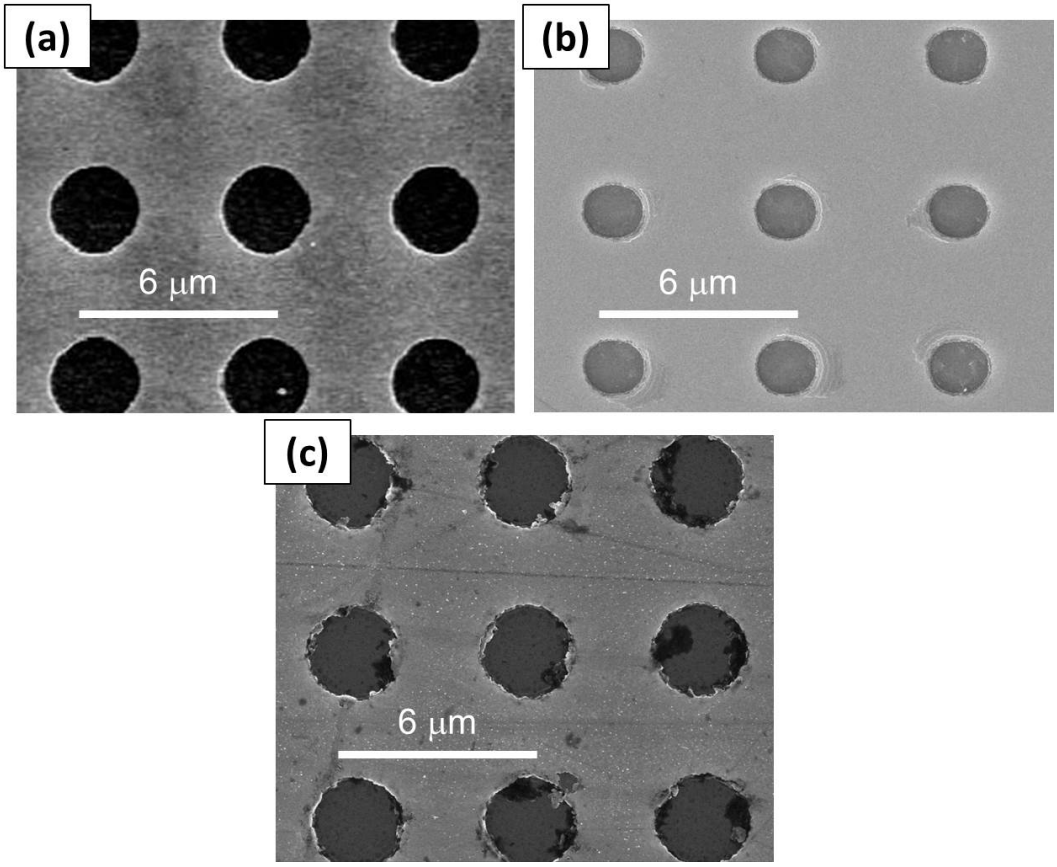

Figure 7.13: From [114]. Original caption: SEM images of perforated Ag films.... (a) SEM image of the polycrystalline Ag film. (b) SEM image of another epitaxial Ag film, one not used in EOT measurements. (c) SEM image of the epitaxial Ag film used for EOT measurements, after exposure to air for nearly two years. Reprinted with permission. Copyright 2012, American Chemical Society.

Bibliography

[1] Hung-ying Chen, Hon-way Lin, Chang-Hong Shen, and Shangjr Gwo. Structure and photoluminescence properties of epitaxially oriented GaN nanorods grown on Si(111) by plasma-assisted molecular-beam epitaxy. *Applied Physics Letters*, 89(24):243105, 2006.

[2] Hong Liu, Y. F. Zhang, D. Y. Wang, M. H. Pan, J. F. Jia, and Q. K. Xue. Two-dimensional growth of Al films on Si(111)-77 at low-temperature. *Surface Science*, 571(1–3):5–11, 2004.

[3] S. H. Xin, P. D. Wang, Aie Yin, C. Kim, M. Dobrowolska, J. L. Merz, and J. K. Furdyna. Formation of self-assembling CdSe quantum dots on ZnSe by molecular beam epitaxy. *Applied Physics Letters*, 69(25):3884–3886, 1996.

[4] A. Kurtenbach, K. Eberl, and T. Shitara. Nanoscale InP islands embedded in InGaP. *Applied Physics Letters*, 66(3):361–363, 1995.

[5] F. Hatami, N. N. Ledentsov, M. Grundmann, J. Bohrer, F. Heinrischsdorff, M. Beer, D. Bimberg, S. S. Ruvimov, P. Werner, U. Gosele, J. Heydenreich, U. Richter, S. V. Ivanov, and B. Ya. Radiative recombination in type-II GaSb/GaAs quantum dots. *Applied Physics Letters*, 67(5):656–658, 1995.

[6] D. J. Eaglesham and M. Cerullo. Dislocation-free Stranski-Krastanow growth of Ge on Si(100). *Physical Review Letters*, 64(16):1943–1946, 1990.

[7] N. Carlsson, W. Seifert, A. Petersson, P. Castrillo, M. E. Pistol, and L. Samuelson. Study of the two-dimensional-three-dimensional growth mode transition in metalorganic vapor phase epitaxy of GaInP/InP quantum-sized structures. *Applied Physics Letters*, 65(24):3093–3095, 1994.

[8] O. Baklenov, D. L. Huffaker, A. Anselm, D. G. Deppe, and B. G. Streetman. Influence of Al content on formation of InAlGaAs quantum dots grown by molecular beam epitaxy. *Journal of Applied Physics*, 82(12):6362–6364, 1997.

[9] E. Alphandery, R. J. Nicholas, N. J. Mason, B. Zhang, P. Mock, and G. R. Booker. Self-assembled InSb quantum dots grown on GaSb: A photoluminescence, magnetoluminescence, and atomic force microscopy study. *Applied Physics Letters*, 74(14):2041–2043, 1999.

[10] G. Abstreiter, P. Schittenhelm, C. Engel, E. Silveira, A. Zrenner, and D. Meertens. Growth and characterization of self-assembled Ge-rich islands on Si. *Semiconductor Science and Technology*.

[11] A. Schreyer, J. F. Anker, Th. Zeidler, H. Zabel, M. Schafer, J. A. Wolf, P. Grunberg, and C. F. Majkrzak. Noncollinear and collinear mag-

netic structures in exchange coupled Fe/Cr(001) superlattices. *Physical Review B*, 52:16066–16085, 1995.

[12] B. Monemar and G. Pozina. Group III-nitride based hetero and quantum structures. *Progress in Quantum Electronics*, 24:239–290, 2000.

[13] H. Ohno. Making Nonmagnetic Semiconductors Ferromagnetic. *Science*, 281:951–956, 1998.

[14] John R. Arthur. Molecular beam epitaxy. *Surface Science*, 500(1-3):189–217, 2002.

[15] A. Many, Y. Goldstein, and N. B. Grover. *Semiconductor Surfaces*. John Wiley and Sons, Inc., 1965.

[16] C. B. Duke. *Atoms and electrons at surfaces: A modern scientific revolution*. American Institute of Physics, on behalf of the American Vacuum Society, 1984.

[17] J. H. Singleton. *The development of valves, connectors, and traps for vacuum systems during the 20th century*. American Institute of Physics, on behalf of the American Vacuum Society, 1984.

[18] L. A. Harris. Miscellaneous topics in Auger electron spectroscopy. *Journal of Vacuum Science and Technology*, 11(1):23, 1974.

[19] Robert L. Park. Inner-shell spectroscopy. *Physics Today*, 28(4):52, 1975.

[20] A. Chambolle and E. Bonnetier. Computing the Equilibrium Configuration of Epitaxially Strained Crystalline Films. *SIAM Journal on Applied Mathematics*, 62(4):1093–1121, 2002.

[21] Antonin Chambolle and Margherita Solci. Interaction of a Bulk and a Surface Energy with a Geometrical Constraint. 39(1):77–102, 2007.

[22] Zhenyu Zhang. Quantum stability of ultrathin metal overlayers on semiconductor substrates. *Surface Science*, 571(1–3):1–4, 2004.

[23] Marian A. Herman, Wolfgang Richter, and Helmut Sitter. *Epitaxy: Physical Principles and Technical Implementation*. Springer-Verlag, 2004.

[24] Arthur R. Smith, Kuo-Jen Chao, Qian Niu, and Chih-Kang Shih. Formation of Atomically Flat Silver Films on GaAs with a "Silver Mean" Quasi Periodicity. *Science*, 273(5272):226–228, 1996.

[25] Richard L. Schwoebel and Edward J. Shipsey. Step Motion on Crystal Surfaces. *Journal of Applied Physics*, 37(10):3682, 1966.

[26] Gert Ehrlich and F. G. Hudda. Atomic View of Surface Self-Diffusion: Tungsten on Tungsten. *The Journal of Chemical Physics*, 44(3):1039, 1966.

[27] E. Bauer. Epitaxy of metals on metals. *Applied Surface Science*, 11/12:479–494, 1982.

[28] Tsun-Mei Chang and Emily A. Carter. Mean-field theory of heteroepitaxial thin metal film morphologies. *Surface Science*, 318(1–2):187–203, 1994.

[29] M. Jalochowski and E. Bauer. Resistance oscillations and crossover in ultrathin gold films. *Physical Review B*, 37(15):8622–8626, 1988.

[30] G. Neuhold, L. Bartels, J.J. Paggel, and K. Horn. Thickness-dependent morphologies of thin Ag films on GaAs(110) as revealed by LEED and STM. *Surface Science*, 376(1–3):1–12, 1997.

[31] Ph. Ebert, K.-J. Chao, Q. Niu, and C. Shih. Dislocations, Phason Defects, and Domain Walls in a One-Dimensional Quasiperiodic Superstructure of a Metallic Thin Film. *Physical Review Letters*, 83(16):3222–3225, 1999.

[32] C.-S Jiang, Hongbin Yu, C.-K Shih, and Ph. Ebert. Effect of the Si substrate structure on the growth of two-dimensional thin Ag films. *Surface Science*, 518(1–2):63–71, 2002.

[33] S. Heun, J. Bange, R. Schad, and M. Henzler. Conductance of Ag on Si (111): a two-dimensional percolation problem. *Journal of Physics: Condensed Matter*, 5:2913–2918, 1993.

[34] R. Schad, S. Heun, T. Heidenblut, and M. Henzler. Magnetoconductivity of Thin Epitaxial Silver Films. *Applied Physics A*, 234:231–234, 1992.

[35] S. B. Arnason and A. F. Hebard. Ultra-thin silver films obtained by sequential quench-anneal processing. *Thin Solid Films*, 518(1):61–65, 2009.

[36] M. Jalochowski and E. Bauer. Quantum size and surface effects in the electrical resistivity and high-energy electron reflectivity of ultrathin lead films. *Physical Review B*, 38(8):5272–5280, 1988.

[37] L. Aballe, C. Rogero, S. Gokhale, S. Kulkarni, and K. Horn. Quantum-well states in ultrathin aluminium films on Si(111). *Surface Science*, 482-485:488–494, 2001.

[38] K.-J. Chao, Zhenyu Zhang, Ph. Ebert, and C.-K. Shih. Substrate effects on the formation of flat Ag films on (110) surfaces of III-V compound semiconductors. *Physical Review B*, 60(7):4988–4991, 1999.

[39] Zhenyu Zhang, Qian Niu, and Chih-Kang Shih. "Electronic Growth" of Metallic Overlayers on Semiconductor Substrates. *Physical Review Letters*, 80(24):5381–5384, 1998.

[40] F. K. Schulte. A theory of thin metal films: electron density, potentials and work function.

[41] Peter J. Feibelman and D. R. Hamann. Quantum-size effects in work functions of free-standing and adsorbed thin metal films. *Physical Review B*, 29(12):6463–6467, 1984.

[42] Peter J. Feibelman. Static quantum-size effects in thin crystalline, simple-metal films. *Physical Review B*, 27(4):1991–1996, 1983.

[43] Y. Jia, M. M. Ozer, H. H. Weitering, and Z. Zhang. *Quantum Size Effects in the Growth and Properties of Ultrathin Metal Films, Alloys, and Related Low-Dimensional Structures*, volume 47 of *Springer Series in Surface Sciences*. Springer, 2011.

[44] Iwao Matsuda, Han Yeom, Takehiro Tanikawa, Kensuke Tono, Tadaaki Nagao, Shuji Hasegawa, and Toshiaki Ohta. Growth and electron quantization of metastable silver films on Si(001). *Physical Review B*, 63(12):1–9, 2001.

[45] Hongbin Yu, C. Jiang, Ph. Ebert, X. Wang, J. White, Qian Niu, Zhenyu Zhang, and C. Shih. Quantitative Determination of the Metastability of Flat Ag Overlayers on GaAs(110). *Physical Review Letters*, 88(1):016102, 2001.

[46] M. M. R. Evans, B. Y. Han, and J. H. Weaver. Ag films on GaAs(110): dewetting and void growth. *Surface Science*, 465(1–2):90–96, 2000.

[47] Georg Neuhold and Karsten Horn. Depopulation of the Ag(111) Surface State Assigned to Strain in Epitaxial Films. *Physical Review Letters*, 78(7):1327–1330, 1997.

[48] M. Horn-von Hoegen, T. Schmidt, M. Henzler, G. Meyer, D. Winau, and K. H. Rieder. Epitaxial layer growth of Ag(111)-films on Si(100).

Surface Science, 331–333:575–579, 1995.

[49] M. Horn-von Hoegen, T. Schmidt, G. Meyer, D. Winau, and K. H. Rieder. Lattice accommodation of low-index planes: Ag(111) on Si(001). *Physical Review B*, 52(15):10764–10767, 1995.

[50] Mingmin Shen, J.-M. Wen, C. J. Jenks, P. A. Thiel, Da-Jiang Liu, and J. W. Evans. Ripening of monolayer vacancy pits on metal surfaces: Pathways, energetics, and size-scaling for Ag(111) versus Ag(100). *Physical Review B*, 75(24):245409, 2007.

[51] K. Morgenstern, G. Rosenfeld, and G. Comsa. Decay of two-dimensional Ag islands on Ag(111). *Physical Review Letters*, 76(12):2113–2116, 1996.

[52] M. Esser, K. Morgenstern, G. Rosenfeld, and G. Comsa. Dynamics of vacancy island coalescence on Ag(111). *Surface Science*, 402–404:341–345, 1998.

[53] N. I. Papanicolaou, G. A. Evangelakis, and G. C. Kallinteris. Molecular dynamics description of silver adatom diffusion on Ag(100) and Ag(111) surfaces. *Computational Materials Science*, 10:105–110, 1998.

[54] Karina Morgenstern, Georg Rosenfeld, Bene Poelsema, and George Comsa. Brownian Motion of Vacancy Islands on Ag(111). *Physical Review Letters*, 74(11):2058–2061, 1995.

[55] J. B. Pendry. Negative refraction makes a perfect lens. *Physical Review Letters*, 85(18):3966–3969, 2000.

[56] Nicholas Fang and Xiang Zhang. Imaging properties of a metamaterial superlens. *Applied Physics Letters*, 82(2):161, 2003.

[57] Nicholas Fang, Hyesog Lee, Cheng Sun, and Xiang Zhang. Sub-diffraction-limited optical imaging with a silver superlens. *Science*, 308(5721):534–537, 2005.

[58] David O. S. Melville and Richard J. Blaikie. Super-resolution imaging through a planar silver layer. *Optics express*, 13(6):2127–34, 2005.

[59] Rizia Bardhan, Surbhi Lal, Amit Joshi, and Naomi J Halas. Theranostic Nanoshells: From Probe Design to Imaging and Treatment of Cancer. *Accounts of Chemical Research*, 44(10):936–946, 2011.

[60] Shuwen Zeng, Ken-Tye Yong, Indrajit Roy, Xuan-Quyen Dinh, Xia Yu, and Feng Luan. A Review on Functionalized Gold Nanoparticles for Biosensing Applications. *Plasmonics*, 6(3):491–506, 2011.

[61] Kyuwan Lee, Vladimir P. Drachev, and Joseph Irudayaraj. DNA-gold nanoparticle reversible networks grown on cell surface marker sites: application in diagnostics. *ACS Nano*, 5(3):2109–17, 2011.

[62] Jiri Homola, editor. *Surface Plasmon Resonance Based Sensors*, volume 4 of *Springer Series on Chemical Sensors and Biosensors*. Springer-Verlag, 2006.

[63] Wenshan Cai, Uday K. Chettiar, Alexander V. Kildishev, and Vladimir M. Shalaev. Optical cloaking with metamaterials. *Nature Photonics*, 1(4):224–227, 2007.

[64] Andrea Alù and Nader Engheta. Multifrequency Optical Invisibility Cloak with Layered Plasmonic Shells. *Physical Review Letters*, 100(11):113901, 2008.

[65] Ulf Leonhardt. Optical conformal mapping. *Science*, 312(5781):1777–1780, 2006.

[66] J. B. Pendry, D. Schurig, and D. R. Smith. Controlling electromagnetic fields. *Science*, 312(5781):1780–2, 2006.

[67] D. Schurig, J. J. Mock, B. J. Justice, S. A. Cummer, J. B. Pendry, A. F. Starr, and D. R. Smith. Metamaterial electromagnetic cloak at microwave frequencies. *Science*, 314(5801):977–980, 2006.

[68] P. R. West, S. Ishii, G. V. Naik, N. K. Emani, V. M. Shalaev, and A. Boltasseva. Searching for better plasmonic materials. *Laser & Photonics Reviews*, 4(6):795–808, 2010.

[69] Thomas W. Ebbesen, Cyriaque Genet, and Sergey I. Bozhevolnyi. Surface-plasmon circuitry. *Physics Today*, 61(5):44, 2008.

[70] Junichi Takahara, Suguru Yamagishi, Hiroaki Taki, Akihiro Morimoto, and Tetsuro Kobayashi. Guiding of a one-dimensional optical beam with nanometer diameter. *Optics letters*, 22(7):475–7, 1997.

[71] Jun Q. Lu and A. A. Maradudin. Channel plasmons. *Physical Review B*, 42(17):11159–11165, 1990.

[72] M. González, J.-C. Weeber, A.-L. Baudrion, A. Dereux, A. Stepanov, J. Krenn, E. Devaux, and T. Ebbesen. Design, near-field characterization, and modeling of 45° surface-plasmon Bragg mirrors. *Physical Review B*, 73(15):155416, 2006.

[73] Valentyn S. Volkov, Sergey I. Bozhevolnyi, Eloïse Devaux, Jean-Yves Laluet, and Thomas W. Ebbesen. Wavelength selective nanophotonic components utilizing channel plasmon polaritons. *Nano Letters*, 7(4):880–884, 2007.

[74] Thomas Nikolajsen, Kristjan Leosson, and Sergey I. Bozhevolnyi. Surface plasmon polariton based modulators and switches operating at telecom wavelengths. *Applied Physics Letters*, 85(24):5833, 2004.

[75] Domenico Pacifici, Henri J. Lezec, and Harry A. Atwater. All-optical modulation by plasmonic excitation of CdSe quantum dots. *Nature Photonics*, 1(7):402–406, 2007.

[76] J. A. Porto, L. Martín-Moreno, and F. J. García-Vidal. Optical bistability in subwavelength slit apertures containing nonlinear media. *Physical Review B*, 70(8):081402, 2004.

[77] G. A. Wurtz, R. Pollard, and A. V. Zayats. Optical Bistability in Nonlinear Surface-Plasmon Polaritonic Crystals. *Physical Review Letters*,

97(5):057402, 2006.

[78] Jose Dintinger, Istvan Robel, Prashant V. Kamat, Cyriaque Genet, and Thomas W. Ebbesen. Terahertz All-Optical Molecule-Plasmon Modulation. *Advanced Materials*, 18(13):1645–1648, 2006.

[79] Darrick E. Chang, Anders S. Sorensen, Eugene A. Demler, and Mikhail D. Lukin. A single-photon transistor using nanoscale surface plasmons. *Nature Physics*, 3(11):807–812, 2007.

[80] S. R. Friberg, Y. Silberberg, M. K. Oliver, M. J. Andrejco, M. A. Saifi, and P. W. Smith. Ultrafast all-optical switching in a dual-core fiber nonlinear coupler. *Applied Physics Letters*, 51(15):1135–1137, 1987.

[81] J. L. Jewell, Y. H. Lee, M. Warren, H. M. Gibbs, N. Peyghambarian, A. C. Gossard, and W. Wiegmann. 3-pJ, 82-MHz optical logic gates in a room-temperature GaAs-AlGaAs multiple-quantum-well etalon. *Applied Physics Letters*, 46(10):918–920, 1985.

[82] Stephen M. Jensen. The Nonlinear Coherent Coupler. *IEEE Journal of Quantum Electronics*, QE-18(10):1580–1583, 1982.

[83] A. Sommerfeld. *Ann. Phys. Chem.*, 67:233, 1899.

[84] J. Zenneck. *Ann. Phys.*, 23:846, 1907.

[85] G. Ruthemann. *Ann. Phys.*, 2:113, 1948.

[86] W. Lang. *Optik*, 3:233, 1948.

[87] David Bohm and David Pines. A Collective Description of Electron Interactions. I. Magnetic Interactions. *Physical Review*, 82(5):625–634, 1951.

[88] David Pines and David Bohm. Collective Description of Electron Interactions: II. Collective vs. Individual Particle Aspects of the Interactions. *Physical Review*, 85(2):338, 1952.

[89] David Bohm and David Pines. A Collective Description of Electron Interactions: III. Coulomb Interactions in a Degenerate Electron Gas. *Physical Review*, 92(3):609–625, 1953.

[90] David Pines. A Collective Description of Electron Interactions: IV. Electron Interaction in Metals. *Physical Review*, 92(3):626–636, 1953.

[91] C. J. Powell and J. B. Swan. Origin of the Characteristic Electron Energy Losses in Magnesium. *Physical Review*, 116(1):81–83, 1959.

[92] C. J. Powell and J. B. Swan. Origin of the Characteristic Electron Energy Losses in Aluminum. *Physical Review*, 115(4):869–875, 1959.

[93] T. W. Ebbesen, H. J. Lezec, H. F. Ghaemi, T. Thio, and P. A. Wolff. Theory of extraordinary optical transmission through subwavelength hole arrays. *Nature*, 391:667–669, 1998.

[94] William L. Barnes, Alain Dereux, and Thomas W. Ebbesen. Surface plasmon subwavelength optics. *Nature*, 424:824–830, 2003.

[95] Stefan A. Maier. *Plasmonics: Fundamentals and Applications*. Springer, 2007.

[96] John David Jackson. *Classical Electrodynamics*. John Wiley and Sons, Inc., third edition, 1999.

[97] J. Dionne, L. Sweatlock, H. Atwater, and A. Polman. Planar metal plasmon waveguides: frequency-dependent dispersion, propagation, localization, and loss beyond the free electron model. *Physical Review B*, 72(7):075405, 2005.

[98] Edward D. Palik, editor. *Handbook of Optical Constants of Solids*. Academic Press, 1985.

[99] Edward D. Palik and G. Ghosh, editors. *Handbook of Optical Constants of Solids II*. Academic Press, 1991.

[100] P. B. Johnson and R. W. Christy. Optical Constants of the Noble Metals. *Physical Review B*, 6(12):4370–4379, 1972.

[101] J. M. Elson and R. H. Ritchie. Photon Interactions at a Rough Metal Surface. *Physical Review B*, 4(12):4129–4138, 1971.

[102] Martin T. Hill. Status and prospects for metallic and plasmonic nanolasers (Invited). *Journal of the Optical Society of America B*, 27(11):B36, 2010.

[103] H. Ehrenreich and H. R. Philipp. Optical Properties of Ag and Cu. *Physical Review*, 128(4):1622–1629, 1962.

[104] B. R. Cooper, H. Ehrenreich, and H. R. Philipp. Optical Properties of Noble Metals. *Physical Review*, 138(2A):A494–A507, 1965.

[105] D. A. Bobb, G. Zhu, M. Mayy, A. V. Gavrilenko, P. Mead, V. I. Gavrilenko, and M. A. Noginov. Engineering of low-loss metal for nanoplasmonic and metamaterials applications. *Applied Physics Letters*, 95(15):151102, 2009.

[106] M. G. Blaber, M. D. Arnold, and M. J. Ford. Optical properties of intermetallic compounds from first principles calculations: a search for the ideal plasmonic material. *Journal of Physics: Condensed Matter*, 21(14):144211, 2009.

[107] Anthony J. Hoffman, Leonid Alekseyev, Scott S. Howard, Kale J. Franz, Dan Wasserman, Viktor A. Podolskiy, Evgenii E. Narimanov, Deborah L. Sivco, and Claire Gmachl. Negative refraction in semiconductor metamaterials. *Nature Materials*, 6(12):946–950, 2007.

[108] Crissy Rhodes, Stefan Franzen, Jon-Paul Maria, Mark Losego, Donovan N. Leonard, Brian Laughlin, Gerd Duscher, and Stephen Weibel. Surface plasmon resonance in conducting metal oxides. *Journal of Applied Physics*, 100(5):054905, 2006.

[109] Stefan Franzen. Surface Plasmon Polaritons and Screened Plasma Absorption in Indium Tin Oxide Compared to Silver and Gold. *Journal of Physical Chemistry C*, 112(15):6027–6032, 2008.

[110] Scott H. Brewer and Stefan Franzen. Calculation of the electronic and optical properties of indium tin oxide by density functional theory. *Chemical Physics*, 300(1–3):285–293, 2004.

[111] F. Michelotti, L. Dominici, E. Descrovi, N. Danz, and F. Menchini. Thickness dependence of surface plasmon polariton dispersion in transparent conducting oxide films at 1.55 um. *Optics letters*, 34(6):839–841, 2009.

[112] Ashkan Vakil and Nader Engheta. Transformation optics using graphene. *Science*, 332(6035):1291–1294, 2011.

[113] Bing Wang, Xiang Zhang, Francisco J. García-Vidal, Xiaocong Yuan, and Jinghua Teng. Strong Coupling of Surface Plasmon Polaritons in Monolayer Graphene Sheet Arrays. *Physical Review Letters*, 109(7):073901, 2012.

[114] Bo-Hong Li, Charlotte E. Sanders, James McIlhargey, Fei Cheng, Changzhi Gu, Guanhua Zhang, Kehui Wu, Jisun Kim, S. Hossein Mousavi, Alexander B. Khanikaev, Yu-Jung Lu, Shangjr Gwo, Gennady Shvets, Chih-Kang Shih, and Xianggang Qiu. Contrast between Surface Plasmon

Polariton-Mediated Extraordinary Optical Transmission Behavior in Epitaxial and Polycrystalline Ag Films in the Mid- and Far-Infrared Regimes. *Nano Letters*, 12(12):6187–6191, 2012.

[115] C. Julian Chen. *Introduction to Scanning Tunneling Microscopy*. Oxford University Press, 1993.

[116] J. Bardeen. Tunneling from a Many-particle Point of View. *Physical Review Letters*, 6(2):57–59, 1961.

[117] Roland Wiesendanger. *Scanning Probe Microscopy and Spectroscopy: Methods and Applications*. Cambridge University Press, 1994.

[118] I. Horcas. *Review of Scientific Instruments*, 78:013705, 2007.

[119] G. Binnig, C. F. Quate, and Ch. Gerber. Atomic Force Microscope. *Physical Review Letters*, 56(9):930–933, 1986.

[120] Ricardo Garcia and Alvaro San Paulo. Attractive and repulsive tip-sample interaction regimes in tapping-mode atomic force microscopy. *Physical Review B*, 60:4961–4967, 1999.

[121] Alex de Lozanne. Sensors for Proximal Probe Microscopy, 2006.

[122] The Nobel Foundation. `http://www.nobelprize.org`, 2013.

[123] J. B. Pendry. *Low Energy Electron Diffraction*. Academic Press, 1974.

[124] Hans Luth. *Solid Surfaces, Interfaces, and Thin Films*. Springer-Verlag, 2010.

[125] Ayahiko Ichimiya and Philip I. Cohen. *Reflection High Energy Electron Diffraction*. Cambridge University Press, 2004.

[126] K. Mae, V. V. Moshchalkov, and Y. Bruynseraede. Intensity profiles along the RHEED streaks for various thin film surface morphologies. *Thin Solid Films*, 340:145–152, 1999.

[127] C. Richard Brundle, Charles A. Evans, and Shaun Wilson. *Encyclopedia of Materials Characterization*. Gulf Professional Publishing, 1992.

[128] Shuji Hasegawa. *Reflection High-Energy Electron Diffraction*. John Wiley and Sons, Inc., 2012.

[129] E. Bauer. *Low Energy Electron Reflection Microscopy*, volume 1. Academic Press, Inc., 1962.

[130] Richard Haight, Frances M. Ross, and James B. Hannon. *Handbook of Instrumentation and Techniques for Semiconductor Nanostructure Characterization*. World Scientific.

[131] J. T. Sadowski, Y. Fujikawa, and T. Sakurai. Nucleation and Growth of Thin Pentacene Films Studied by LEEM and STM. In Yasunori Fujikawa, Kazuo Nakajima, and Toshio Sakurai, editors, *Frontiers in Materials Research*. Springer, 2008.

[132] R. M. Tromp. Low-energy electron microscopy. *IBM Journal of Research and Development*, 44(4):503–516, 2000.

[133] M. S. Altman, W. F. Chung, Z. Q. He, H. C. Poon, and S. Y. Tong. Quantum size effect in low energy electron diffraction of thin films. *Applied Surface Science*, 170:82–87, 2001.

[134] Y.-J. Lu, J. Kim, H.-Y. Chen, C. Wu, N. Dabidian, C. E. Sanders, C.-Y. Wang, M.-Y. Lu, B.-H. Li, X. Qiu, W.-H. Chang, L.-J. Chen, G. Shvets, C.-K. Shih, and S. Gwo. Plasmonic Nanolaser Using Epitaxially Grown Silver Film. *Science*, 337(6093):450–453, 2012.

[135] L. Vitos, A. V. Ruban, H. L. Skriver, and J. Kolla. The surface energy of metals. *Surface Science*, 411:186–202, 1998.

[136] David Bergman and Mark Stockman. Surface Plasmon Amplification by Stimulated Emission of Radiation: Quantum Generation of Coherent Surface Plasmons in Nanosystems. *Physical Review Letters*, 90(2):027402, 2003.

[137] Paul Horowitz and Winfield Hill. *The Art of Electronics*. Cambridge University Press, second edition, 2006.

[138] Nir Magen, Avinoam Kolodny, Uri Weiser, and Nachum Shamir. Interconnect-Power Dissipation in a Microprocessor. In *Proceedings of the 2004 international workshop on system level interconnect prediction*, number 74, pages 7–13, 2004.

[139] International Technology Roadmap for Semiconductors (ITRS). `http://www.itrs.net/Links/2011ITRS/Home2011.htm`, 2011.

[140] ITRS Interconnect Working Group. `http://www.itrs.net/Links/2011Winter/11_Interconnect.pdf`, 2011.

[141] R. F. Oulton, V. J. Sorger, D. A. Genov, D. F. P. Pile, and X. Zhang. A hybrid plasmonic waveguide for subwavelength confinement and long-range propagation. *Nature Photonics*, 2(8):496–500, 2008.

[142] Rupert F. Oulton, Volker J. Sorger, Thomas Zentgraf, Ren-Min Ma, Christopher Gladden, Lun Dai, Guy Bartal, and Xiang Zhang. Plasmon lasers at deep subwavelength scale. *Nature*, 461(7264):629–632, 2009.

[143] Hung-Ying Chen, Hon-Way Lin, Chang-Hong Shen, and Shangjr Gwo. Structure and photoluminescence properties of epitaxially oriented GaN nanorods grown on Si(111) by plasma-assisted molecular-beam epitaxy. *Applied Physics Letters*, 89(24):243105, 2006.

[144] Haoyan Wei and Hergen Eilers. From silver nanoparticles to thin films: Evolution of microstructure and electrical conduction on glass substrates. *Journal of Physics and Chemistry of Solids*, 70(2):459–465, 2009.

[145] H. Bethe. Theory of Diffraction by Small Holes. *Physical Review*, 66(7–8):163–182, 1944.

[146] A. D. Rakic, A. B. Djurisic, J. M. Elazar, and M. L. Majewski. Optical properties of metallic films for vertical-cavity optoelectronic devices. *Applied optics*, 37(22):5271–5283, 1998.

[147] C. Genet, M. P. van Exter, and J. P. Woerdman. Fano-type interpretation of red shifts and red tails in hole array transmission spectra. *Optics Communications*, 225(4–6):331–336, 2003.

[148] Michaël Sarrazin, Jean-Pol Vigneron, and Jean-Marie Vigoureux. Role of Wood anomalies in optical properties of thin metallic films with a bidimensional array of subwavelength holes. *Physical Review B*, 67(8):085415, 2003.

[149] Bo-Hong Li, Houfang Liu, Fei Cheng, Jing Han, Hong Xiao, Xiufeng Han, Changzhi Gu, and Xianggang Qiu. Local rotational symmetry effects on Fano resonances with constant non-resonant transmission channel. *Applied Physics Letters*, 101(3):031114, 2012.

[150] Prashant Nagpal, Nathan C. Lindquist, Sang-Hyun Oh, and David J. Norris. Ultrasmooth patterned metals for plasmonics and metamaterials. *Science*, 325(5940):594–597, 2009.

Vita

Charlotte Sanders was born on February 15, 1978 in Englewood, Colorado. She attended high school at Judge Memorial Catholic High School in Salt Lake City, Utah, and in 2003 earned her Bachelor of Arts in Comparative Literature from Barnard College in New York, having focused on the literature of the early Roman empire and eighteenth century imperial Russia. She then earned a Master of Arts degree in Physics from City University of New York's Hunter College in 2007 under the guidance of Professor Ying-Chih Chen; her master's thesis concerned phase locking in fiber laser arrays. She entered the doctoral program in Physics at the University of Texas at Austin in 2007.

Permanent address: 1003 Justin Lane, #2089
Austin, Texas 78757
U.S.A.

This dissertation was typeset with LaTeX[†] by the author.

[†]LaTeX is a document preparation system developed by Leslie Lamport as a special version of Donald Knuth's TeX Program.